UNIVERSIDAD DE CHILE
FACULTAD DE CIENCIAS FÍSICAS Y MATEMÁTICAS
DEPARTAMENTO DE INGENIERÍA ELÉCTRICA

A PROOF OF CONCEPT DOUBLE TONE READOUT FOR KINETIC INDUCTANCE DETECTOR BOLOMETERS

TESIS PARA OPTAR AL GRADO DE MAGÍSTER EN CIENCIAS DE LA INGENIERÍA, MENCIÓN ELÉCTRICA

SEBASTIÁN ANTONIO JORQUERA TAPIA

PROFESOR GUÍA:
RICARDO FINGER CAMUS

PROFESOR CO-GUÍA:
DAVID MONASTERIO LAGOS

MIEMBROS DE LA COMISIÓN:
NICOLÁS REYES GUZMÁN
WALTER MAX-MOERBECK ASTUDILLO

Este trabajo ha sido financiado parcialmente por los fondos
Basal FB210003, FONDECYT 1221662 y FONDEF ID21-10359

SANTIAGO DE CHILE
2024

RESUMEN DE LA TESIS PARA OPTAR
AL GRADO DE MAGÍSTER EN CIENCIAS
DE LA INGENIERÍA, MENCIÓN ELÉCTRICA
POR: SEBASTIÁN ANTONIO JORQUERA TAPIA
FECHA: 2024
PROF. GUÍA: RICARDO FINGER CAMUS

PRUEBA DE CONCEPTO DE LECTURA DE DOS TONOS PARA BOLÓMETROS DE DETECTORES DE INDUCTANCIA CINÉTICA

Los detectores de inductancia cinética (MKIDs por sus siglas en inglés) son una tecnología sumamente atractiva para detectores de baja energia, como los requeridos en astronomía.

La tecnología MKID permite colocar múltiples detectores en una línea de alimentación, permitiendo que un solo dispositivo de lectura monitoree cientos de detectores. El problema de lectura necesita soluciones dedicadas, por lo que el Max-Planck Institute desarrolló un sistema llamado U-board basado en FPGA y GPU.

El objetivo de este documento es el estudio de factibilidad de un algoritmo de lectura de dos tonos para la cámara APEX-MKID usando la U-board. La matemática de la lectura por fase es presentada y a partir de ella se desarrollan dos tipos de lecturas de dos tonos, una coloca los tonos a igual distancia de la frecuencia de resonancia y la segunda los coloca equidistantes al centro de la zona lineal del resonador.

Se realizaron pruebas de sensibilidad para calcular la temperatura equivalente de ruido (NET), obteniendo $2.77mK\sqrt{s}$ para la lectura de un tono y $3.62mK\sqrt{s}$, $3.44mK\sqrt{s}$ para los modos con dos tonos. Los resultados muestran que el ruido añadido por duplicar los tonos supera la ganancia de incrementar el tiempo de integración de tener dos tonos.

RESUMEN DE LA TESIS PARA OPTAR
AL GRADO DE MAGÍSTER EN CIENCIAS
DE LA INGENIERÍA, MENCIÓN ELÉCTRICA
POR: SEBASTIÁN ANTONIO JORQUERA TAPIA
FECHA: 2024
PROF. GUÍA: RICARDO FINGER CAMUS

A PROOF OF CONCEPT DOUBLE TONE READOUT FOR KINETIC INDUCTANCE DETECTOR BOLOMETERS

Microwave kinetic inductance detectors (MKIDs) are a detector technology based on the change of the resonant frequency due to the hit of a photon. This technology is attractive for low-energy detectors as used in astronomy. The MKID technology enables to place multiple detectors in the same feed line, needing a single readout to measure hundreds of detectors.The readout problem needs custom solutions, so the Max-Planck institute built a readout based on an FPGA and GPU called U-board.

This document has as objective the feasibility study of a double-tone readout algorithm for the APEX-MKID camera using this new readout. The phase-readout mathematics is presented, and based on it, a double-tone readout was developed. Two types of double-tone readout were implemented: one places the tones at the same distance of the resonant frequency, and the second places the tones equidistant to the center of the linear phase of the IQ circle.

Sensitivity tests were made to obtain the noise equivalent temperature (NET), obtaining 2.77mK*sqrt(s) for the single-tone and 3.62mK*sqrt(s) and 3.44mK*sqrt(s) for the double-tone modes. As a conclusion, the noise added by doubling the tones overcomes the sensitivity gain of increasing the integration time when having a double-tone readout.

¡ Apartense vacas,
que la vida es corta!
GGM

Agradecimientos

Quiero agradecer a todas las personas con las que tuve la suerte de compartir en este tiempo, puedo decir que cada uno es un ser espectacular. Siempre me he considerado una persona sumamente afortunada por el hecho de haber encontrado (y seguir encontrando) gente increible a mi alrededor.

Doy gracias al laboratorio de ondas milimétricas y a sus integrantes, por la buena onda y por todas las enseñanzas que tuve en ese lugar todos los años que estuve. El laboratorio es un lugar genial, donde pude conocer valiosa gente y me pude desarrollar como profesional en el área que me encanta y de la que disfruto cada día.

Quiero agradecer a la gente del Max Planck que me recibió y permitió jugar con la camara A-MKID en Bonn. En especial agradezco enfaticamente a Nicolás Reyes, Bernd Klein y Gerrit Grutzeck que fueron esenciales para el desarrollo de este trabajo y por todas las gestiones que realizaron para que se pudiera llevar a cabo.

Gracias también a mi comisión por entregarme valioso feedback para poder terminar de escribir correctamente este documento, muchas gracias por su tiempo y los buenos consejos.

Finalmente, me gustaria terminar agradeciendo a mi familia, siempre presente en todo lo que hago y dando apoyo constantemente.

Table of Content

Tables index

Figures index

Chapter 1

Introduction

Observational astronomy is a field that is in constant search for promising new technologies that can expand the exploration of faint distant objects that cannot be observed with the current technology. In that sense, astronomical receivers are at the cutting edge of what is technologically feasible, and each new generation of receivers is a showcase of the advances in different disciplines like material science, physics, electronics, and data processing, among others. In this new generation of receivers, Microwave Kinetic Inductance Detectors (MKID) cameras have gained attention due to their high sensitivity and the capability to build large cameras with relative ease using the current technology available.

MKIDs cameras are direct detectors that use as a working principle the break of the Cooper pairs due to the capture of photons, being able to reach photon-noise-limited sensitivity. Each MKID detector consists of a superconductor resonator circuit coupled to a feed line and to one antenna that captures photons. As the detector is in the superconductor regime, the resistance of the circuit is very low, obtaining notch-type resonators with a large quality factor, enabling the placement of several detectors with different resonant frequencies in the same line. For example, the APEX-MKID (A-MKID) camera has approximately 800 detectors per line, and the complete camera has 24 lines, forming a receiver with nearly 19200 pixels. To read the response of these large pixel quantities, the standard procedure consists of placing a single tone near each resonant frequency to monitor the changes in amplitude and phase. These changes have to be measured simultaneously for each detector as fast as possible with the minor downtime between measures, forcing the design and construction of dedicated readouts for this type of receiver.

In this document, the development and characterization of a double tone readout are presented. For the development of this new readout method, a novel FPGA-GPU system designed by the Max-Planck-Institut für Radioastronomie (MPIfR) called U-Board was used. For the testing and characterization of the performance of the method, the A-MKID receiver was used.

1.1. Hypothesis

The hypothesis of this thesis is that when doubling the quantity of tones per MKID, the sensitivity of the overall system will increase since this method doubles the integration time.

1.2. General Objective

The main objective of this thesis is the development and characterization of a double tone readout for the APEX MKID camera.

1.3. Specific Objectives

1. Make a mathematical description of the phase readout for MKIDs to have a theoretical framework to work on.
2. Develop an algorithm that enables the double tone readout mode.
3. Characterize the sensitivity achieved by the double tone readout and compare it with the standard single tone readout.

1.4. Thesis outline

The sections of this document are structured with the following order:

- Chapter 2: In this chapter Bolometers and superconductor theory are presented in a brief way. There is a subchapter dedicated to describe resonator theory, which takes a fundamental role in the understand of the readout system.
- Chapter 3: In this chapter the Atacama Pathfinder EXperiment (APEX) telescope, the A-MKID camera and the new A-MKID readout system are presented.
- Chapter 4: In this chapter the double tone implementation and the test to determine its performance are described.
- Chapter 5: In this chapter the conclusions of the results obtained for the double tone readout are presented, and possible future work guidelines are described.

Chapter 2

Theoretical Framework

2.1. Astronomical receivers

For millimeter and sub-millimeter wavelengths, the observations are mainly made by two types of receivers: heterodyne receivers and bolometers. Each one of those receiver types has its own benefits and limitations for a given observation, so the astronomer must select the receiver that better matches the scientific requirements.

On one side, heterodyne receivers are coherent detectors that have as core device a mixer that down-converts the high frequency signals coming from the sky to a lower frequency that can be digitized. This downconvertion conserves the amplitude and phase information of the signal over time, enabling the study of spectral line emission/absorption, which is fundamental for the detection of certain molecules in astronomical sources.

As heterodyne receivers conserve the amplitude and phase information of the signal, they enable a plethora of applications, such as interferometry between multiple antennas or phased arrays. The main drawback of heterodyne receivers is that they usually have a narrow bandwidth, and the noise of these types of receivers is limited by the quantum noise. From a practical point of view, each element in a heterodyne receiver is hard to design and build, making it complicated to build multi-pixel cameras, and the ones that do exist do not surpass the tens of pixels magnitude order.

On the other side, bolometers can be thought as thermometers; they only measure changes in temperature due to the emission of celestial objects, i.e. the bolometers just detect the intensity of the observed object. Opposed to heterodyne receivers, bolometers have a larger bandwidth, but at the cost of just detecting total power and not being able to determine the frequency components of the incoming radiation with the precision of a heterodyne receiver.

As an advantage, bolometers are not limited by the quantum noise, making them more sensitive to weaker signals than the heterodyne counterpart. The building process of large cameras is simpler, enabling the creation of huge multipixel cameras with thousands of pixels.

For these features the bolometers are better suited for low intensity detections and to map large regions of the sky. With larger maps astronomers can find interesting regions that can be studied afterwards with a heterodyne instrument.

In this section we are going to focus in the working principles of the bolometers, since MKIDs belong to that receiver category. Even if the working principle of MKIDs is different from the standard bolometers, most of the concepts can be transferred and the metrics to characterize them are the same.

2.1.1. Bolometers

The standard thermal detector is composed by an absorbing element with a heat capacity C that converts the radiation into heat and a heat sink with temperature T_s connected to the absorbing element via thermal conductance G as shown in figure 2.1

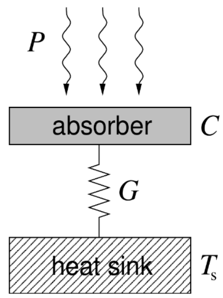

Figure 2.1: Basic schematic of a thermal detector. Image extracted from [1].

When the sky signal with a power P hits the detector, the temperature of the absorbing element increases at a rate $\frac{dT_B}{dt} = \frac{P}{C}$ approaching the limiting value $T_B = T_S + P/G$ with a time constant of $\tau = C/G$. In the same way, when the radiation stops hitting the detector the temperature will lower to T_S with the same time constant τ.

Then, the requirements for the absorbing material are a large absorptivity over the interested frequency range and a low heat capacity. In contrast, the supporting substrate should have a low heat capacity and large thermal conductivity to keep it isothermal during the bolometer operation.

The basic bolometer uses an electrical resistive thermometer to measure the temperature change of the absorbing element. This thermometer must satisfy a low heat capacity, low electrical noise and a proper temperature dependence of the resistance. The thermometer is attached to the absorber element to generate a readout of the temperature change. When using a semiconductor thermometer, a bias current must be applied to generate a negative thermal feedback to keep it in a stable operation [1]. In those cases, a current is constantly passing through the thermistor adding a readout power that gets into the read temperature as equation 2.1 shows, where $P_{bias} = V_{bias}I$

$$T = T_0 + (P_{signal} + P_{bias})/G \tag{2.1}$$

2.1.2. Noise Equivalent Power (NEP)

The most important parameters that characterize a bolometer behavior are the time constant τ and the *Noise Equivalent Power* (NEP) which is the power absorbed that produces a signal-to-noise ratio of unity at the output [2]. In other words, is the smallest power difference that produces a signal equals to the noise level of the detector itself.

As simple rule of thumb, a smaller NEP indicates a more sensitive detector as the detector can sense smaller changes of power with a higher SNR. Even though NEP is used as a parameter for comparison between bolometers is not an absolute measure of sensitivity, since it depends on the specific measurement conditions, for example the background noise present when doing the measurement.

Usually the NEP can be split in two components as equation 2.2 shows.

$$NEP^2 = NEP^2_{detector} + NEP^2_{background} \tag{2.2}$$

In an ideal case a bolometer is limited by the background noise, which means that if the detector noise is small enough to be negligible the NEP is mostly dominated by the thermal noise of the optics and the sky.

As the bolometer acts as a direct detector the noise can only be calculated after post detection averaging, this leads to the convenient usage of the units $W/Hz^{1/2}$ to represent a normalized NEP.

Two large contributors of the detector noise are the Johnson noise and phonon noise. The Johnson noise is generated due the random motions of the electrons in the thermometer and can be written as equation 2.3 shows, where k_B is the Boltzmann constant, R is the detector resistance and S is the responsivity of the detector and it is the parameter that represents the conversion between input power and the output voltage, it has units of V/W.

$$NEP^2_{Johnson} = \frac{4k_BTR}{S^2} \tag{2.3}$$

The phonon noise is a representation of the quantization of the lattice vibration made by quasi-particles called phonons that acts as transport system of the thermal energy between the absorber and the heat sink. The phonon noise can be written as equation 2.4, where G is the thermal conductance show in figure 2.1.

$$NEP^2_{phonon} = 4k_BT^2G \tag{2.4}$$

The background noise coming from the sky and optics emission is called photon noise, and is generated due the random fluctuations in the rate of absorption of photons. If the signals satisfy the Rayleigh-Jeans approximation $h\nu < k_BT$ and assuming a limited bandwidth $\Delta\nu$ with a central frequency ν_0, then we could write the photon noise as the expression in equation 2.5, where η is the overall transmission of the system, ϵ is the average emissivity and T is the background temperature.

$$NEP^2_{photon} = 2(h\nu_0 + \eta\epsilon k_BT)P_{signal} \tag{2.5}$$

If we join those theoretical expressions of the NEP components, we obtain the expression in equation 2.6. This equation shows that for an optimal behavior of the receiver we need to minimize T, G and R and it becomes evident that the temperature plays an outstanding role in the overall system noise. Lowering the operating temperature reduces dramatically the detector noise and for that reason bolometers are operated at cryogenic temperatures.[1]

$$NEP^2 = \frac{4k_BTR}{S^2} + 4k_BT^2G + 2(h\nu_0 + \eta\epsilon K_BT)P_{signal} \tag{2.6}$$

For completeness, there is an alternative way to present the sensitivity of a bolometer instrument using the temperature instead of the power called Noise Equivalent Temperature (NET). NET would be preferred for certain measurement setups where the temperature of the test loads are known.

[1] In the specific case of MKIDs the low temperature is also a requirement to produce the superconductor state.

The most trivial approach to relate the NEP and NET comes from the computation of the power sensed by an antenna from a blackbody of a given temperature. In the most general case the blackbody spectral energy density is given by equation 2.7, that is the energy per volume per unit frequency, and the total power sensed by an antenna is expressed in equation 2.8, where A_{eff} is the effective area and $F(\theta,\phi)$ is the normalized antenna beam pattern.

$$I_{blackbody} = 2\frac{h\nu^3}{c^2}\frac{1}{exp\left(\frac{h\nu}{k_BT}\right)-1}[\frac{\text{Watts}}{m^2Hz\cdot sr} \tag{2.7}$$

$$P_{sensed} = \frac{A_{eff}}{2}\int_{\nu}^{\nu+\delta\nu}\int\int_{4\pi} I_{blackbody}F(\theta,\phi)d\Omega d\nu \tag{2.8}$$

As trivial example where we can obtain a closed form of this power-temperature relation, we can restrict our study to the case of low frequencies where $\frac{hf}{k_BT} < 1$, called the Rayleigh-Jeans regime. In this regime the spectral energy density can be approximated by equation 2.9.

$$I_{blackbody} \approx \frac{2\nu^2k_BT}{c^2} = \frac{2k_BT}{\lambda^2} \tag{2.9}$$

If we replace the Rayleigh-Jeans approximation and assume that the beam pattern approximately constant in $\Delta\nu$ then power sensed by the antenna is given by equation 2.10 but the beam pattern in a solid angle $\Omega_A = A_{eff}/\lambda^2$ leading to the final result show in equation 2.11, where B represents the total bandwidth that is being observed. Since the power-relation obtained in the Rayleigh-Jeans regime is linear the relation between NET and NEP is direct.

It must be said that since some bolometers have a high operational frequency, the Rayleigh-Jeans approximation is not valid and one should solve the equation 2.8 to obtain the power-temperature relation.

$$P_{sensed} = \frac{A_{eff}}{2}\frac{2k_BT}{\lambda^2}\Delta\nu\int F(\theta,\phi)d\Omega = \frac{A_{eff}}{2}\frac{2k_BT}{\lambda^2}\Delta\nu \tag{2.10}$$

$$P = k_BT\Delta\nu = K_BTB \tag{2.11}$$

As a summary, in this subsection the basic noise sources that limit the performance of a bolometer were presented. In particular, the NEP/NET quantities were introduced as a way to measure the sensitivity of a bolometer.

As briefly mentioned at the beginning of this subsection, the concepts presented here are the standard equations used in a bolometer that uses the thermal conductance as detection method. In the MKID based bolometers the absorbing element is an antenna and the thermometer are no longer a simple resistance but a superconductor resonant circuit. Using a superconducting device has as side effect that the resistance of the thermometer approaches to zero, improving the noise of the whole system.

The next subsections are a short introduction to superconductivity concepts that makes the MKID detector technology possible.

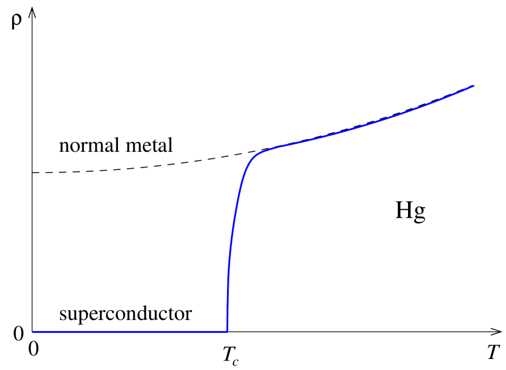

Figure 2.2: In a superconductor there is an abrupt decay in the resistance when the material reaches its critical temperature T_C. Image extracted from [3].

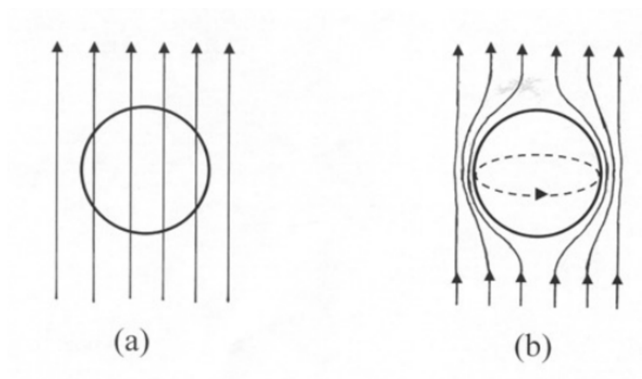

Figure 2.3: Meissner effect: a) In the normal state the conductor let pass the external magnetic field. b) Below the critical temperature the material expels the interior magnetic field and also rejects the external one. Image extracted from [4]

2.2. Superconductor theory

Superconductors were discovered by H. Kamerlingh-Onnes in 1911 in his laboratory for low-temperature physics while he was measuring material parameters using liquid helium to cool them down. Kamerlingh-Onnes discovered that some materials drop their DC resistance to zero when the temperature is lower than a critical temperature T_C as figure 2.2 shows. In a normal metal the resistance decreases with temperature but reaches a finite value when $T \to 0$.

The second main characteristic of these superconductor materials was found in 1933 by Meissner and Oschsenfeld. They discovered that in the superconductor state the material not only rejects the entrance of a magnetic field into the material (as perfect conductivity predicts) but also expels the field that the original non-superconductor material has inside when reaching the superconductor state. This effect is called the Meissener effect, and it implies that superconductivity can be destroyed due to the effect of a critical magnetic field H_C. This was a turning point in the study of superconductors because the existence of this effect suggested that superconductivity is a thermodynamic equilibrium state that can be reached independently of the path that leads to it.

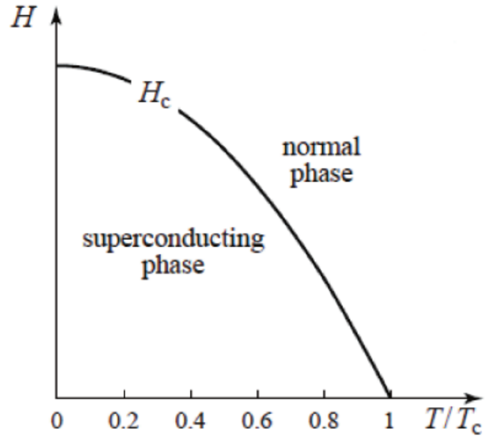

Figure 2.4: Temperature dependence of the critical magnetic field. Image extracted from [4].

It took 50 years of study for the physicist to arrive to a theory that could explain the superconductor effects in a satisfactory way: the Bardeen-Cooper-Schrieffer (BCS) theory which uses second quantization techniques to explain the formation of a macroscopic quantum state that is responsible for the superconductivity. Understanding the BCS theory requires knowledge of quantum field theory, and since we only want to understand the concept behind the superconductor effect, we are going to start with the semi-classical explanations that can predict and explain some effects observed in the superconductor regime without introducing quantum mechanical formalism.

2.2.1. London equations

The London equations are built using the Drude model as their base. The standard Drude model treats the electrons in a material as ballistic particles that can move across a lattice that forms the material and uses a classical expression to model their behavior.

The basic Drude equation is shown in 2.12, where e is the electron charge, m is the electron charge, E is an electric field, τ is the relaxation time of the material, and v is the speed of the moving electron. In the Drude model the electron is accelerated by an electric field E and de-accelerated due to the collision with the immobile ions of the material lattice. The relaxation time τ in this equation represents the time it would take to stop the movement of one electron due to the lattice scattering process.

$$m\frac{dv}{dt} = eE - m\frac{v}{\tau} \tag{2.12}$$

In a steady state for a metal we would have $v = eE\tau/m$, if there are n electrons in a volume unit, then we obtain the Ohm's law $J = nev = (ne^2\tau/m)E = \sigma E$. For the superconductor case, the scattering term is neglected since the relaxation time $\tau \to \infty$ and we obtain an acceleration on the current given by equation 2.13 where the term n_s represents the number of superconductor electrons.

$$\frac{dJ_s}{dt} = \frac{n_s e}{m}E = \frac{E}{\Lambda} \tag{2.13}$$

These ideas led London to postulate equation 2.14 refer as the first London equation, where

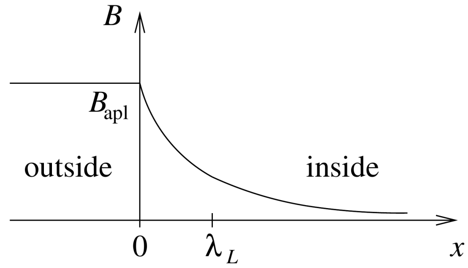

Figure 2.5: Meissner effect predicted by London equations. Image extracted from [3].

the Λ term is a phenomenological parameter that depends on the material. Also, looking carefully, the Λ term depends on the number of superconductor electrons (n_s) present in the material. It is expected that n_s also depends on the material temperature.

The first London equation describes perfect conductivity: in the London picture, the electric field accelerates the superconductor electrons, opposed to a normal material that follows Ohm's law $J = \sigma E$ where the velocity of the electron is linear with the electric field.

$$E = \frac{\partial}{\partial t}(\Lambda J_s) \tag{2.14}$$

$$H = -c\boldsymbol{\nabla} \times (\Delta J_s) \tag{2.15}$$

$$\Lambda = \frac{4\pi\lambda}{c^2} = \frac{m}{n_s e^2} \tag{2.16}$$

The second London equation is shown in expression 2.15 and describes the Meissner effect. The relation is clear when combining it with the Maxwell equation $\boldsymbol{\nabla} \times H = \frac{4\pi J}{c}$, leading to equation 2.17 that tells us that the magnetic field is expelled from the interior of the material in an exponential way with a penetration depth of λ. The dependence on temperature of the penetration depth was found empirically as equation 2.18. In the limit $T << T_C$ the typical values for the penetration depth are $\lambda = 40 - 80nm$ [4], and in the limit $T \rightarrow T_C$ we have $\lambda \rightarrow \infty$

$$\nabla^2 H = \frac{H}{\lambda^2} \tag{2.17}$$

$$\lambda(T) \approx \lambda(0)\Big[1 - \frac{T}{T_C}^{4}\Big] \tag{2.18}$$

2.2.2. Two fluid model

Even though for static currents, superconductors can be treated as lossless diamagnetic objects, for most practical uses, the current will be alternating, and in that case superconductor materials show a finite dissipation.

Following the London equation on 2.14, the electromagnetic field E will accelerate and de-accelerate the superconductor electrons, and this electric field will also act on the normal (non-superconductor) electrons, producing a scattering process with the material lattice following Ohm's law.

To account for this effect, the two fluid model treats the overall system as a superposition of the responses of the superconducting electrons and normal electrons and then uses the Drude model as the starting point to derive the resulting effect. So, the total electron density n can be divided into two parts: a superconducting part n_s with a relaxation time $\tau_s \to \infty$ and a normal part n_n with a finite relaxation time τ_n.

Inserting these assumptions in the Drude model and making the corresponding algebra, we will obtain the first London equation 2.14 for the superconductor part. Meanwhile, for the normal part, we will get the equivalent of Ohm's law shown in the equation 2.19.

$$J_n = \frac{n_n e^2 \tau_n}{m} E \tag{2.19}$$

Now we are going to analyze the effect of a harmonic field $E = E_0 e^{i\omega t}$ obtaining a complex conductivity, as the equation 2.20 shows, where the frequency is below the gap frequency of the material.

This equation shows a non-zero dissipation for non-DC signals and explains the finite Q factors in superconductor resonators.

$$\sigma(\omega) = \Big[(\pi n_s e^2/2m)\delta(\omega) + n_n e^2 \tau_n/m\Big] + i\Big[\frac{n_s e^2}{m\omega}\Big] \tag{2.20}$$

2.2.3. Bardeen Cooper Schrieffer (BCS) theory

The most basic introduction to BCS theory consists of looking at the interaction between two electrons via an attractive potential in a material.

The starting point is the time-independent Schrödinger equation $\hat{H}\left|\Psi\right\rangle = E\left|\Psi\right\rangle$, where $\hat{H}$ is the Hamiltonian of the system, Ψ is the wave function, and E are the eigenenergies of the system.

The equation 2.21 is the time independent Schrödinger equation for two electrons of mass m, with a Hamiltonian $\hat{H} = \hat{p}_1 + \hat{p}_2 + V(\vec{r_1} - \vec{r_2})$ where $\hat{p}_i = -i\hbar\nabla_i$ is the momentum operator in the position basis, and $V(\vec{r}_1 - \vec{r}_2)$ is an attractive potential that only depends on the distance between the particles.

$$\left[-\frac{\hbar\nabla^2_{r_1}}{2m} - \frac{\hbar\nabla^2_{r_2}}{2m} + V(\vec{r_1} - \vec{r_2})\right] \Psi(\vec{r_1}, \vec{r_2}) = E\Psi(\vec{r_1}, \vec{r_2}) \tag{2.21}$$

Making the standard transformations of the two-body problem $\vec{r} = \vec{r_1} - \vec{r_2}$, $\vec{R} = (\vec{r_1} + \vec{r_2})/2$, $M = 2m$, $\mu = m/2$ the Schrödinger equation becomes equation 2.22

$$\Big[-\frac{\hbar\nabla^2_R}{2M} - \frac{\hbar\nabla^2_r}{2\mu} + V(\vec{r})\Big]\Psi(\vec{r}, \vec{R}) = E\Psi(\vec{r}, \vec{R}) \tag{2.22}$$

Here we note that the potential does not depend on the mass center, thus we could define an effective energy as $\overline{E} = E - \hbar^2 K^2/(2M)$ and take the Fourier transform over the Schrödinger equation to obtain the expression in 2.24, where we define $\epsilon_k = \hbar^2 k^2/(2m)$, that is the free electron energy. The importance of this expression is that the energy of the bounded pair is less than the energy of two independent electrons. Finally, we rewrite equation 2.24 as the expression 2.25 defining the quantity $\Delta(k)$.

$$\frac{\hbar^2 k^2}{2\mu}\Psi(k) + \int d^3 r V(r)\Psi(r)e^{-ikr} = \overline{E}\Psi(k) \tag{2.23}$$

$$\int \frac{d^3 k'}{(2\pi)^3} V(k-k')\Psi(k') = (E - 2\epsilon_k)\Psi(k) \tag{2.24}$$

$$\Delta(k) = (E - 2\epsilon_k)\Psi(k) \tag{2.25}$$

Before continuing with the algebra, it is necessary to introduce the Fermi level concept, which is the highest energy level that an electron can occupy at a given temperature. It can be thought as the outermost electron level in the energy surface sphere.

For a material that follows the Fermi-Dirac statistics, the electrons near the Fermi level are the ones that produce the electrical conduction, so it makes sense to restrict the analysis of the potential in the neighborhood of that level.

The other concept that needs to be quickly introduced is the Debye model, which is a simple model that treats a material as a collection of phonons. Since the distance between the atoms in a material limits the wavelength of the vibration, there is an upper limit to the possible vibration frequencies; this is known as the Debye frequency ω_D. Therefore, all modes of the phonons are under the Debye frequency, and since the energy of a phonon is given by $E = h\omega$, consequently the possible energies are also bounded.[5]

With these ideas in mind, we take as potential $V(k-k') = -V_0$ and consider that it only affects the electron with energies in the range $(\epsilon_F, \epsilon_F + \omega_D)$ to obtain the expression in 2.27.

$$\Delta = V_0 \rho(\epsilon_k)\Delta \int_{\epsilon_F}^{\epsilon_F+\omega_D} \frac{d\epsilon}{2\epsilon - E} \tag{2.26}$$

$$\frac{2}{V_0\rho(\epsilon_F)} = ln\left(\frac{2\epsilon_F - E + 2\omega_D}{2\epsilon_F - E}\right) \tag{2.27}$$

The final approximation consists of taking the limit $V_0\rho(\epsilon_F) << 1$, where we can consider $2\epsilon_F - E + 2\omega_D \sim 2\omega_D$ to finally get the expression of the binding energy of two electrons in equation 2.28. The importance of this expression is that it tells us that a bound state between two electrons will be formed regardless of how small the attraction potential that exists between them is. This bound state formed by two electrons is called a Cooper pair.

$$2\epsilon_F - E = E_b = 2\omega_D e^{-\frac{2}{V_0\rho(\epsilon_F)}} \tag{2.28}$$

This basic introduction that shows the instability in the Fermi sea causes the formation of bounding pairs under an arbitrary small attractive potential was the main inspiration for the Bardeen, Cooper, and Schrieffer (BCS) theory. The BCS theory takes this idea one step further and treats the many-body electronic problem to show that the complete system is unstable to the formation of a unique ground state where most of the particles condensate, becoming a macroscopic quantum state where the main carriers are the Cooper pairs. Like the theory involves second quantization methods and mean field approximations, we are going to describe it only qualitatively here.

The main idea is that the interaction between electrons of opposite spins can be mediated by a phonon exchange; these electrons form the Cooper pair. A more intuitive explanation

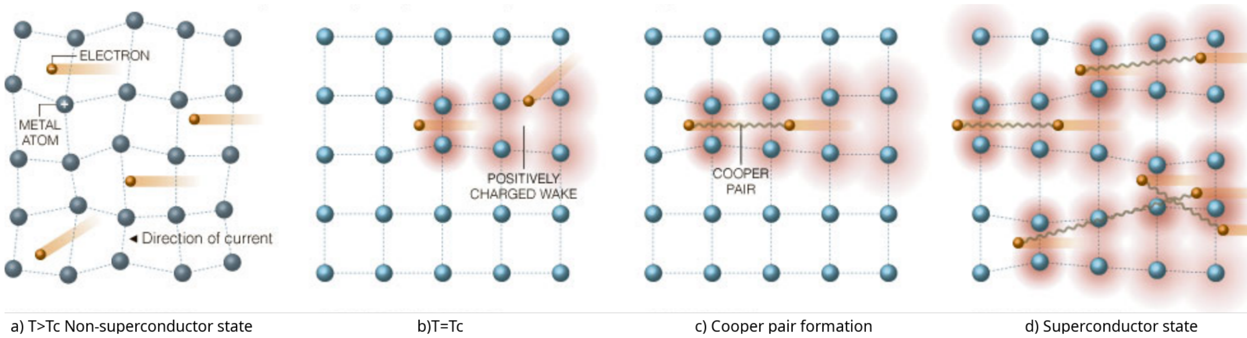

Figure 2.6: Sketch of the formation of Cooper pairs due the interaction of the electrons with the surrounding lattice. a) Is the normal state of the material when $T > T_c$, b) shows the effect of a charged particle over the lattice, c) shows the Cooper pair formation enabled by the lattice and d) shows the superconductor state where several electrons have been paired creating a macroscopic effect. Image extracted from [6].

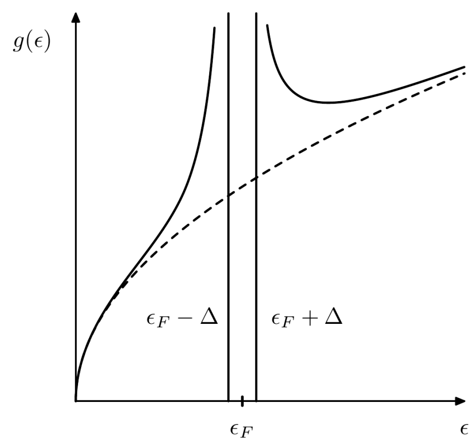

Figure 2.7: Density of states (DOS) of electrons in superconducting regime. In dashed line is showed the normal DOS of given by a Fermi distribution. This image shows that there are no states within the energy gap in the superconductor regime. Image extracted from [7].

consists on the picture where the first electron passes through the medium and polarizes the ion cores of the lattice, generating a zone with an excess of positive charges that attracts the second electron, as figure 2.6 shows.

The important points of this theory for the present document are:

- The superconductivity is produced by the binding of two electrons mediated by the interaction with the surrounding phonons.
- The bind of the Cooper pairs reduces its total energy by 2Δ, generating a gap in the density of states, as figure 2.7 shows. So, in order to break the pairing you need to inject at least $2\Delta \approx 3.5 k_B T_C$.

2.2.4. Kinetic inductance

As mentioned in the previous subsections, one can model the overall impedance of one superconductor using the two fluid model, obtaining an imaginary component that only depends on the superconductor carriers, as equation 2.20 shows.

The kinetic inductance is the circuital representation of the energy stored in the inertial motion of the Cooper pairs. For example, for a superconductor wire of cross-sectional area A and length l, we can obtain the kinetic inductance by equating the kinetic energy of the Cooper pairs with the inductive energy generated by an inductor. This equation will lead to the expression 2.29, where we can see that the kinetic inductance increases when the Cooper pair density decreases, since to maintain the same amount of current, the carriers should have a greater velocity.

$$L_k = \frac{m}{2n_s e^2}\frac{l}{A} \tag{2.29}$$

Another important aspect of kinetic inductance is that it behaves in a non-linear way when interacting with large currents. This is typically expressed as a Taylor expansion, as equation 2.30 shows. The non-linear behavior of the kinetic inductance makes the superconductor materials good candidates to be used in mixing and amplification processes, as for example SIS mixers and parametric amplifiers. For the case of MKID resonators, the Taylor expression in equation 2.30 adds non-desired terms that should be carefully treated managing the readout power that is injected to each resonator to avoid a non-linear response.

$$L_k = L_0\left[1 + \left(\frac{I}{I_{*1}}\right)^2 + \left(\frac{I}{I_{*2}}\right)^3 + \ldots\right] \tag{2.30}$$

2.3. Microwave kinetic inductance detectors

Microwave kinetic inductance detectors (MKIDs) are a type of superconductor photon detector. The working principle of the MKIDs is to indirectly measure the change in the Cooper pairs number in the superconductor material due to the effect of the incident photons.

As mentioned in the previous sections, the Cooper pairs can be broken when injecting an amount of energy higher than 2Δ. The MKID detectors idea relies on forming superconductor resonators where the circuit is coupled to an antenna that receives radiation. The photons with energy $\hbar\nu > 2\Delta$ will be able to break a Cooper pair, affecting the kinetic inductance value thus leading to a change in the resonant frequency.

In summary, MKIDs receivers monitor the resonant frequency of the superconductor resonant circuit, which varies due to the change in kinetic inductance due to the Cooper pair breaking. A feed-line is connected to the readout system to inject test signals to characterize the state of the resonator circuit. An equivalent circuit of a single MKID is shown in figure 2.8.

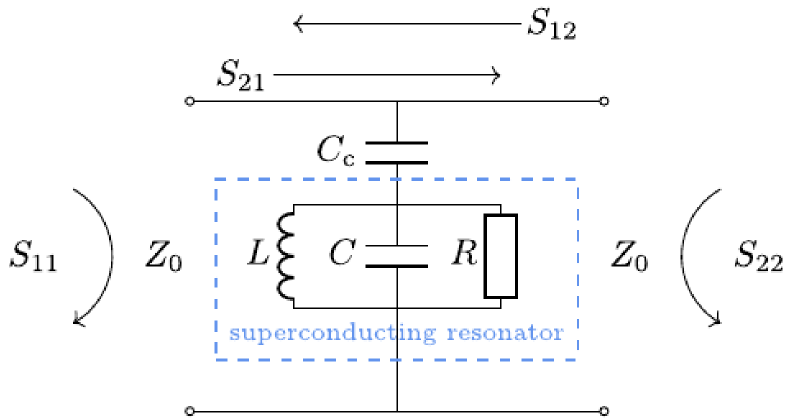

Figure 2.8: Single MKID circuital diagram. Image extracted from [8].

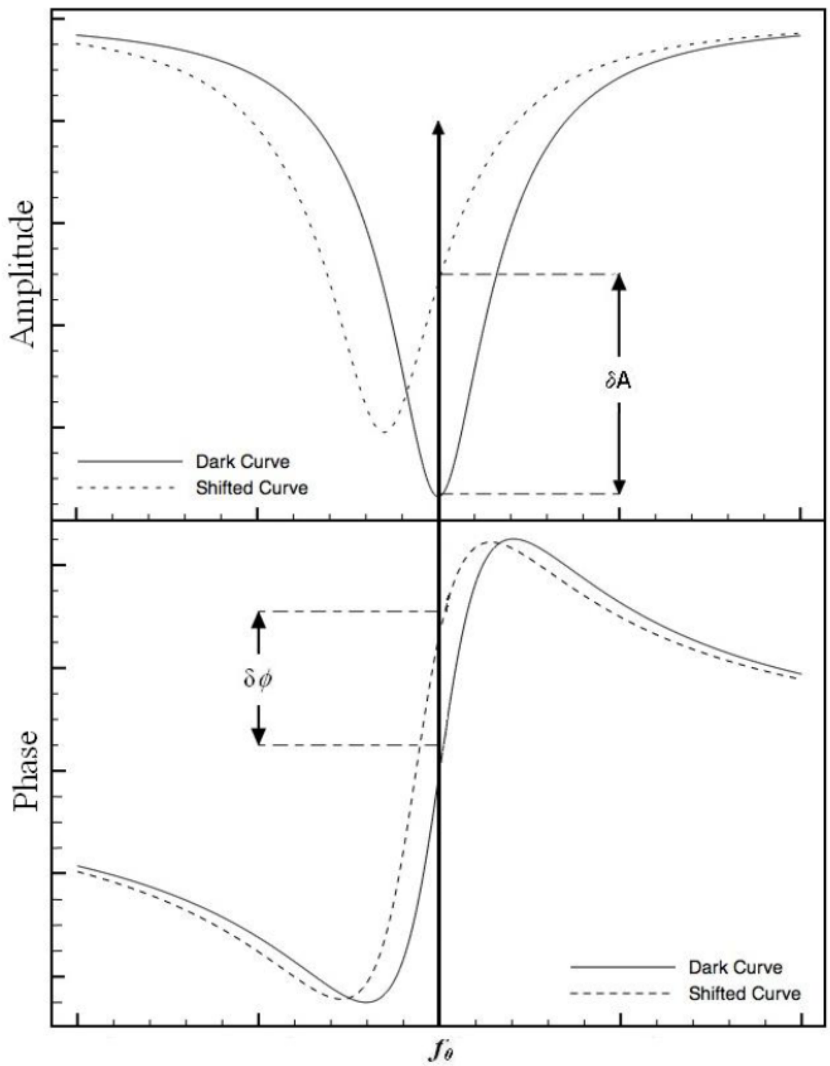

Figure 2.9: Effect produced in the amplitude and phase of the S_{21} in a MKID by a change on the kinetic inductance due a Cooper pair breaking by a photon. Image extracted from [9].

The formation of a single MKID detector only requires the addition of a capacitor to the superconductor material, and given the superconductor's low resistance, the resultant resonator has a huge quality factor, meaning that the resonance is very well localized in the frequency domain. This well defined localization is used to multiplex the readout of the MKIDs.

Since the natural resonant frequency is mainly determined by the values of the inductance and the capacitor, it is possible to tune each MKID to a different resonant frequency. This allows the placement of several detectors at different resonant frequencies, leaving the monitoring problem of each detector to the readout system.

This ability to frequency multiplex the detectors allows the reading of hundreds of detectors at the same time using a single feed-line with a single low-noise amplifier connected to it. This is the main advantage of MKIDs compared to other detectors such as transition edge sensors (TESs) or superconducting tunnel junctions (SJTs).

The equivalent circuit of a line with several MKIDs is shown in figure 2.10. The basic idea to monitor the change in the resonant frequency consists of injecting a tone that sweeps over the whole bandwidth to measure the detector's response. This is equivalent to using a vector network analyzer to measure the S_{21} parameter.

This sweeping method is not optimal because it wastes time sweeping each frequency point with a single tone, and it would also measure frequency points that are not relevant to determine the resonance shift. These flaws at the end mean that the effective integration time of one MKID is just a fraction of the whole process.

These problems led to the development of custom readout systems that are dedicated to monitor each MKID in a more optimal way. The standard method consists of a preliminary characterization of each MKID detector following a theoretical resonator model. With the model parameters acquired for each detector, a single tone can be placed in each MKID to monitor its variation. Having this tone constantly measuring the state of the MKID gives an optimal result since all the time is used to integrate the status of the detector.

To have a deeper understanding of the readout procedure, it is necessary to introduce some concepts of resonator theory.

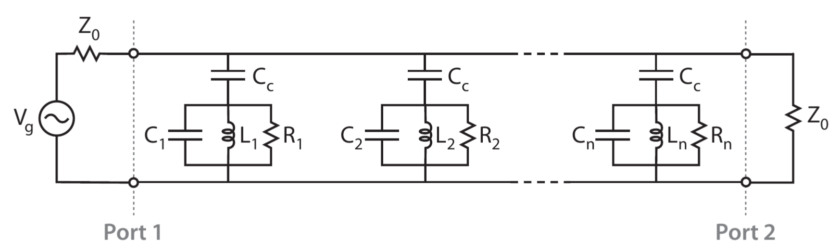

Figure 2.10: Multiple MKIDs circuits in the same line and the corresponding S21. As can be seen there is one resonance per MKID. Image extracted from [10].

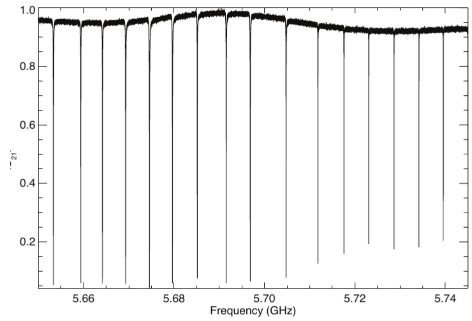

Figure 2.11: Response of a MKID line composed by several detectors tuned to a different resonant frequency. Image extracted from [11].

2.4. Resonator theory

A resonator circuit is characterized mainly by its resonance frequency f_r and the quality factor Q. The quality factor can be defined as the ratio of the stored energy by the circuit and the energy lost in one radian of the oscillation cycle [12]. One can distinguish different sources of energy loss that contribute to the quality factor; among them, the most important are the internal losses and the coupling losses, which are described by the internal quality factor Q_i and the coupling or external quality factor Q_c. The total quality factor of the complete circuit is given by the addition of the two reciprocal values, $Q^{-1} = Q_i^{-1} + \mathrm{Re}\{Q_c^{-1}\}$.

As a model to describe the S_{21} scattering coefficient of a notch type resonator, the equation 2.31 [13] is used, where f describes the test frequency, f_r the resonant frequency, Q_l the loaded quality factor, $|Q_c|$ the absolute value of the coupling quality factor, and ϕ quantifies the impedance mismatch between the coupling line and the resonator itself.

The terms grouped as *environment* are external contributions that come from outside the resonator (cable losses, phase delays, etcetera). To handle these external contributions, the standard practice is to calibrate the measurement setup to discount from the overall response before the measurement of the device under test.

$$S_{21} = \underbrace{a e^{i\alpha} e^{-2\pi i f \tau}}_{\text{environment}} \underbrace{\left[1 - \frac{(Q_l/|Q_c|)e^{i\phi}}{1 + 2iQ_l(f/f_r - 1)}\right]}_{\text{ideal resonator}} \tag{2.31}$$

The most common way to measure a resonator consists of utilizing a vector network analyzer that generates a frequency sweep on port 1 and measures the transmission on port 2. As mentioned previously, for a bolometer composed of MKIDs this method is inefficient since we have to wait for a complete sweep to have an update on the information about the resonator state. And since the quality factors of the superconductor resonators are large, we are interested in a small region of the complete bandwidth. Then a frequency sweep on the complete band will spend most of the time characterizing frequency zones that do not contain valuable information.

The aim of this subsection is to explain the resonator model in equation 2.31 and how different visualizations of this equation could lead to a better representation that enables a continuous monitor of the resonators state.

2.4.1. Resonators are Circles

We are going to take a closer look at the second term inside brackets of equation 2.31. This expression is called $\hat{S}_{21}$ in the expression 2.32. We focus on that expression because the rest of the terms in equation 2.31 are just transformations over the generated curve. To simplify the development, we introduce the variable $t = f/f_r - 1$ and add a convenient zero to generate the equation 2.36 that satisfies a circle equation $x^2 + y^2 = r^2$ with radius 1/2 centered at $(x, y) = (1/2, 0)$.

$$\hat{S}_{21} = \frac{1}{1 + 2iQ_l(f/f_r - 1)} = \frac{1}{1 + 2iQ_l t} = \tag{2.32}$$

$$\frac{1}{1 + 4Q_l^2 t^2} - \frac{2iQ_l t}{1 + 4Q_l^2 t^2} = \tag{2.33}$$

$$\frac{1}{1 + 4Q_l^2 t^2} + \left(\frac{1}{2} - \frac{1}{2}\right) - \frac{2iQ_l t}{1 + 4Q_l^2 t^2} = \tag{2.34}$$

$$\frac{1/2 - 2Q_l^2 t^2}{1 + 4Q_l^2 t^2} + \frac{1}{2} - \frac{2iQ_l t}{1 + 4Q_l^2 t^2} \tag{2.35}$$

$$x(t) = \mathrm{Re}\left\{\hat{S}_{21}\right\} = \frac{1}{2}\left(\frac{1 - 4Q_l^2 t^2}{1 + 4Q_l^2 t^2}\right) + \frac{1}{2} \qquad y(t) = \mathrm{Im}\left\{\hat{S}_{21}\right\} = -\frac{1}{2}\left(\frac{4iQ_l t}{1 + 4Q_l^2 t^2}\right) \tag{2.36}$$

To better understand the selected substitutions in 2.32, it is necessary to briefly introduce the Weierstrass substitution and the stereographic projection of a circle.

The Weierstrass substitution, or half-angle substitution, is based on the relation $t = \tan(\theta/2)$; this allows us to express sines and cosines as the expression in 2.37 shows. Using the Weierstrass substitution, the circle curve can be parametrized using equations in 2.38 and 2.39, which have the same structure as $\hat{S}_{21}$ in expression 2.36.

$$\sin(\theta) = \frac{2t}{1 + t^2} \qquad \cos(\theta) = \frac{1 - t^2}{1 + t^2} \tag{2.37}$$

$$x = x_0 + r\cos(\theta) = x_0 + r\frac{1 - t^2}{1 + t^2} \tag{2.38}$$

$$y = y_0 + r\sin(\theta) = y_0 + r\frac{2t}{1 + t^2} \tag{2.39}$$

Explaining such parametrization in a deeper way requires the introduction of the concept of stereographic projection of the circle into the real line shown in figure 2.12. The stereographic projection is one of several ways to map the points that are part of a circle to a 1D line.

This mapping is made by placing a unit circle and from the point $(x, y) = (-1, 0)$ start to draw lines with a given angle θ. Then the height t where the lines cut the y axis maps the angle θ as figure 2.12 shows.

The final trick consists of mapping θ to the arc subtended between the point $(-1, 0)$ and the point where the traced line cuts the circle (the green points in the figure 2.12). We denote this arc as ϕ. Using simple geometry, we can determine that $\phi = \theta/2$ and as the circle is unitary ϕ is also the angle of the standard polar coordinate system.

It can be shown that this transformation completely maps the angles of a circle into the real line, but it is important to note that the angles are not evenly spaced in this new parametrization. It is clear in figure 2.12 that the red points have different separations; for example, the angles in $(0, -\pi/2)$ are mapped to the interval $(0, 1)$ and the interval $(\pi, -\pi)$ is mapped to $(1, +\infty)$.

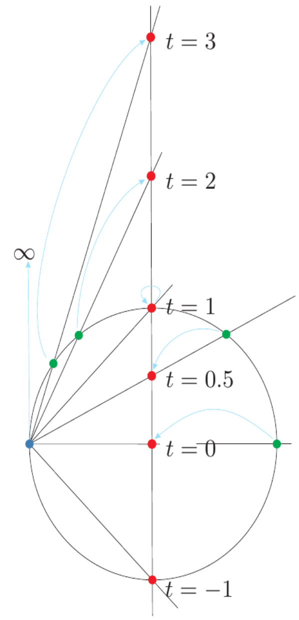

Figure 2.12: Stereographic projection of a circle into the real line. Image extracted from [14].

Figure 2.13 shows a different visualization of a resonator and how the complex plane maps the uniformly spaced points in the real plane to non-uniform points in the circle. The marked red and blue points span $60kHz$ but in the complex plane, the red marks are mapped to nearly half of the circle, and the blue marks have less than one quarter. This non-uniform spacing is also shown in the histogram of 2.13.a, where most of the points are in the extremes. Another important piece of information is that the peak of this resonance in the complex plane is always located at the point $(x, y) = (1, 0)$.

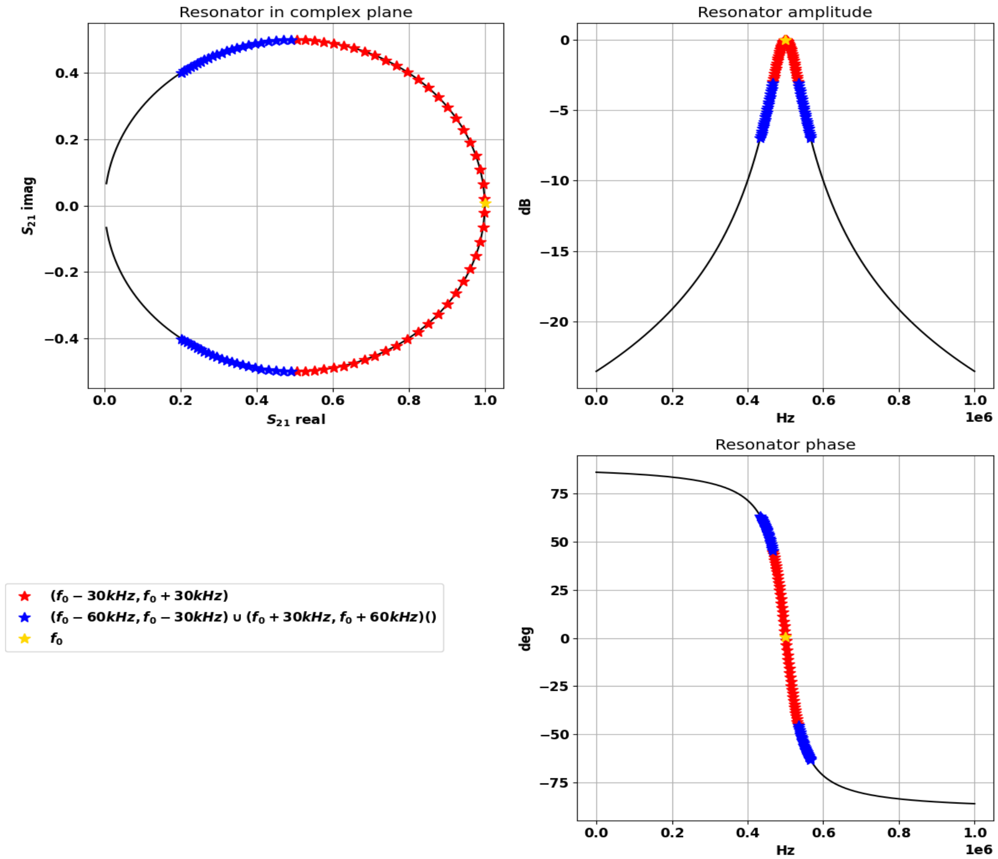

(a) Points distribution in different visualization for S_{21}. The marked points are linearly spaced in frequency, where the red and blue marks span $\approx 60kHz$ each. As can be seen in the complex plane figure, the $60kHz$ are not equally distributed in that representation.

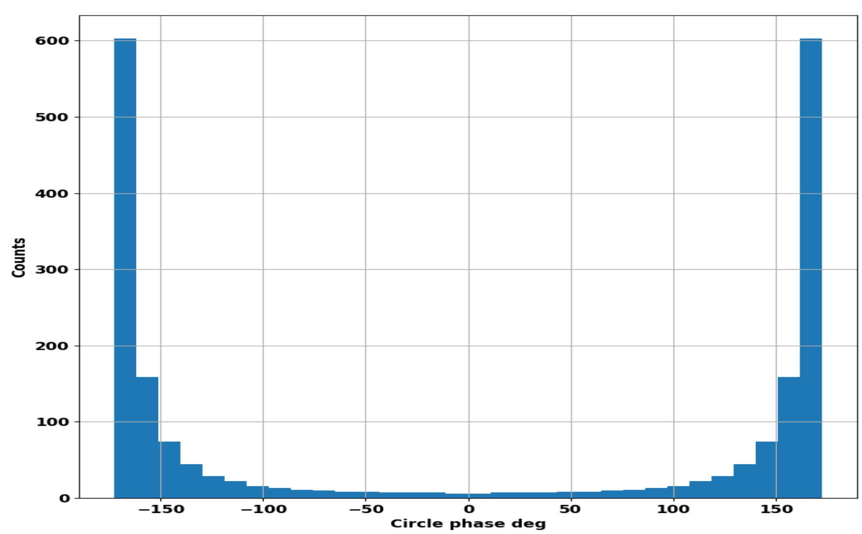

(b) Histogram of the phase on the complex circle in figure 2.13.a. This shows that a uniform sampling is not mapped to a uniform spacing in the circle domain.

Figure 2.13: Distribution of points on a resonator.

This circle visualization allows us to simply represent the change in the resonant frequency as a rotation of the circle in the complex plane.

Figure 2.14 shows two resonator curves that have the same Q but the resonance frequency differs. As the marker at 0.5 MHz shows, the overall effect of changing the resonance frequency is a rotation on the complex plane. This agrees with the previous statement that both curves should have the resonance point at $(0, 1)$, forcing the rotation.

This rotation in the circle of the complex plane will be the parameter that we want to monitor to determine the state of the MKID. As the measure of this rotation only requires the measurement of a single frequency point, it allows the measurement of several points at the same time with minimal effort.

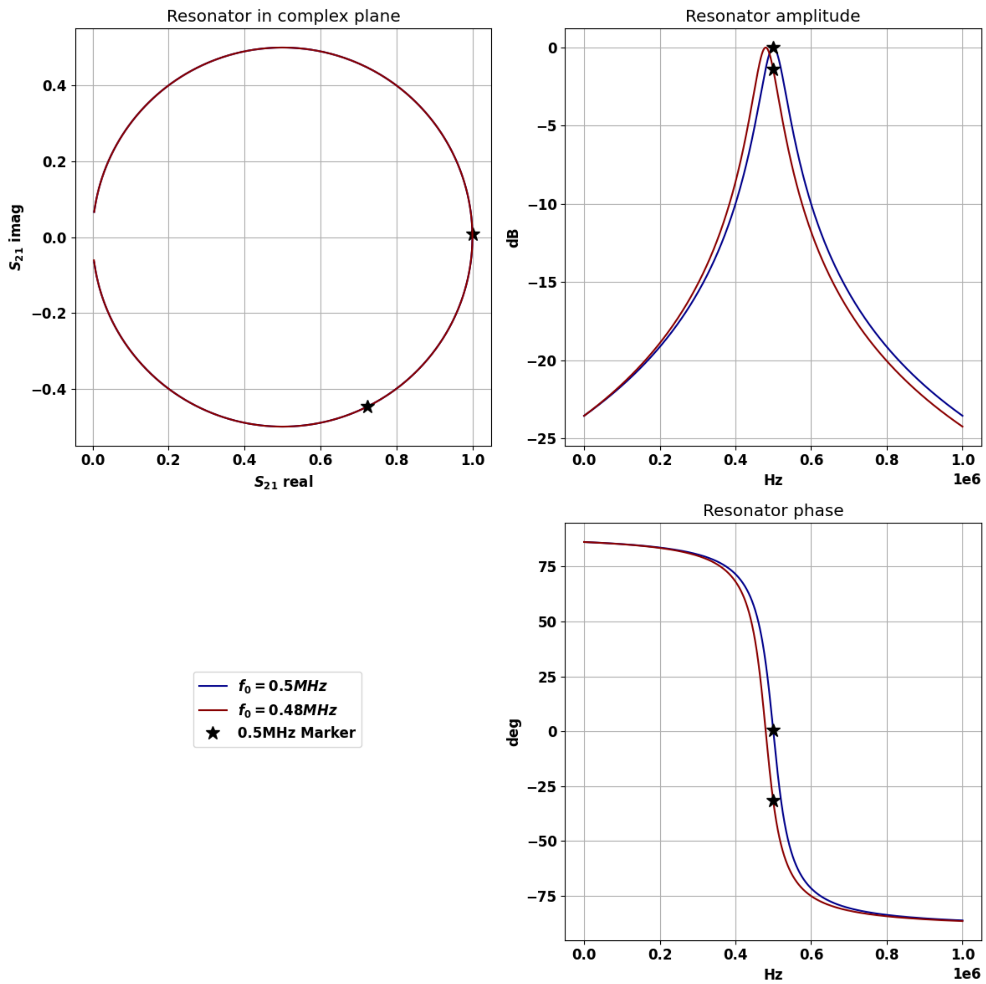

Figure 2.14: Response of a change in the resonant frequency of a resonator in different views. This image shows that in the circle domain the change in the resonant frequency translate into a rotation.

2.4.2. Modifications over the circle

$$S_{21} = ae^{i\alpha}e^{-2\pi i f\tau}\left[1 - \frac{(Q_l/|Q_c|)e^{i\phi}}{1+2iQ_l(f/f_r-1)}\right] = \tag{2.40}$$

$$ae^{i\alpha}e^{-2\pi i f\tau}\left[1 - (Q_l/|Q_c|)e^{i\phi}\hat{S}_{21}\right] \tag{2.41}$$

Until now, we had only focused on the study of a single term of equation 2.31 that is copied in 2.41 for the convenience of the reader. Now we are going to see the transformation produced by the rest of the terms on the generated curve.

To isolate the effect of each term, we are going to add them progressively to the ideal resonator expression and see their effect over the complex curves.

First, we are going to start adding the complex term ϕ that comes from the impedance mismatch of the coupling circuit and the resonator itself. In the complex plane, this phase term produces a rotation of ϕ, taking the origin as a pivot point. So, every point on the circle gets operated by a rotation matrix, as equation 2.43 and figure 2.15 show.

$$S_{21} = \frac{e^{i\phi}}{1+2iQ_l(f/f_r-1)} \tag{2.42}$$

$$\begin{pmatrix} x' \\ y' \end{pmatrix} = \begin{pmatrix} \cos(\phi) & -\sin(\phi) \\ \sin(\phi) & \cos(\phi) \end{pmatrix} \begin{pmatrix} x \\ y \end{pmatrix} \tag{2.43}$$

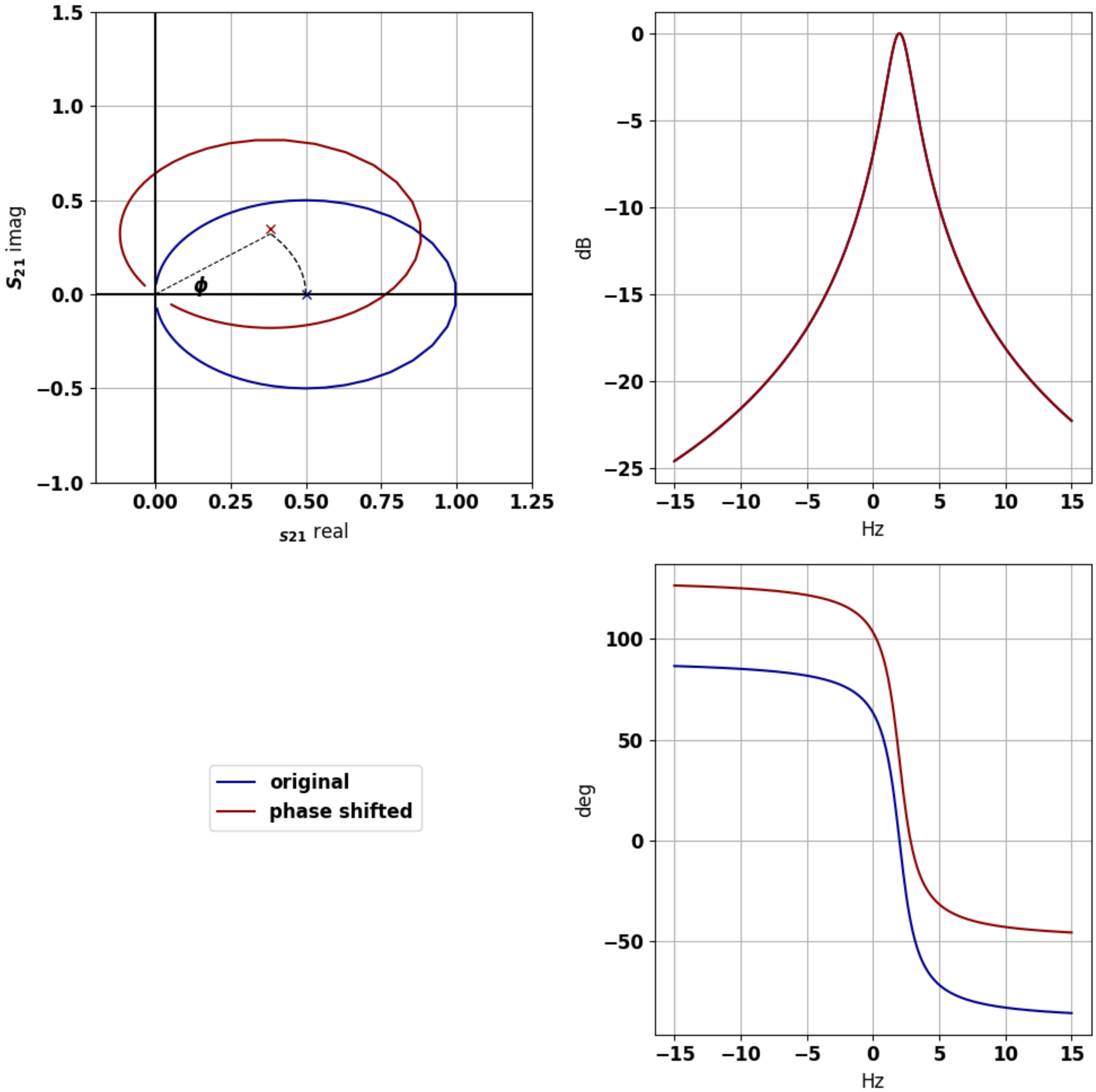

Figure 2.15: Effect of the phase term ϕ over the different representations of the resonator in equation 2.42.

$$S_{21} = 1 - \frac{Q_l/Q_c e^{i\phi}}{1 + 2iQ_l(f/f_r - 1)} \tag{2.44}$$

The next modification is to take $Q_l \neq Q_c$, generating a change in the radius of the circle and also modifying the position of the center accordingly.

To obtain the notch resonator type, we transform the S_{21} expression into the form of equation 2.44. The minus sign can be written as $e^{i\pi}$ giving again another rotation of the circle with the origin as pivot point. The addition of 1 is a shift of the reference coordinate system in the complex plane, but as the movement is only in the real axis, it generates substantial changes on the power and phase curves.

Figure 2.16 shows the effect of the different terms over a notch resonator given by equation 2.44. In the complex plane, the curves are still modeled as a circle that varies its center and radius. For the notch resonator, the points at frequencies $-\infty$ and $+\infty$ are located now at the point $(1, 0)$ in the complex plane, and the resonance occurs at the point of the circle where the distance to the origin is minimum.

In the complex plane, the blue curve just shows the effect of the rotation in 180°, which would let the previous circle of figure 2.15 centered at $(-1/2, 0)$ but then is moved by $(1, 0)$ to its final center position at $(1/2, 0)$.

The red curve shows the effect of adding the phase term ϕ; the final effect of this term is a rotation using as a pivot point $(1, 0)$.

The magenta curve is obtained by keeping the same phase term as the red curve but having different values of Q_l and Q_c, causing variations in the circle radius but keeping the point $(1, 0)$ as an extreme value. So, the overall effect of this radius modification is accompanied by a movement of the circle center. In the magnitude visualization the effect of the phase term ϕ causes an asymmetry in the curve, where for the selected value of ϕ, the left side of the dip has a zone with higher power than the right side. This asymmetry also causes a little deviation on the actual resonant frequency value.

The effect of the difference on the quality factors translate into a decrease on the deepness of the resonance.

The phase graphics show that for the blue curve, there is an abrupt change in the phase values near the resonance frequency. The effect of the phase term ϕ causes a smooth transition on the phase change near the resonance, and the effect of having different quality factors enhances that smoothing effect.

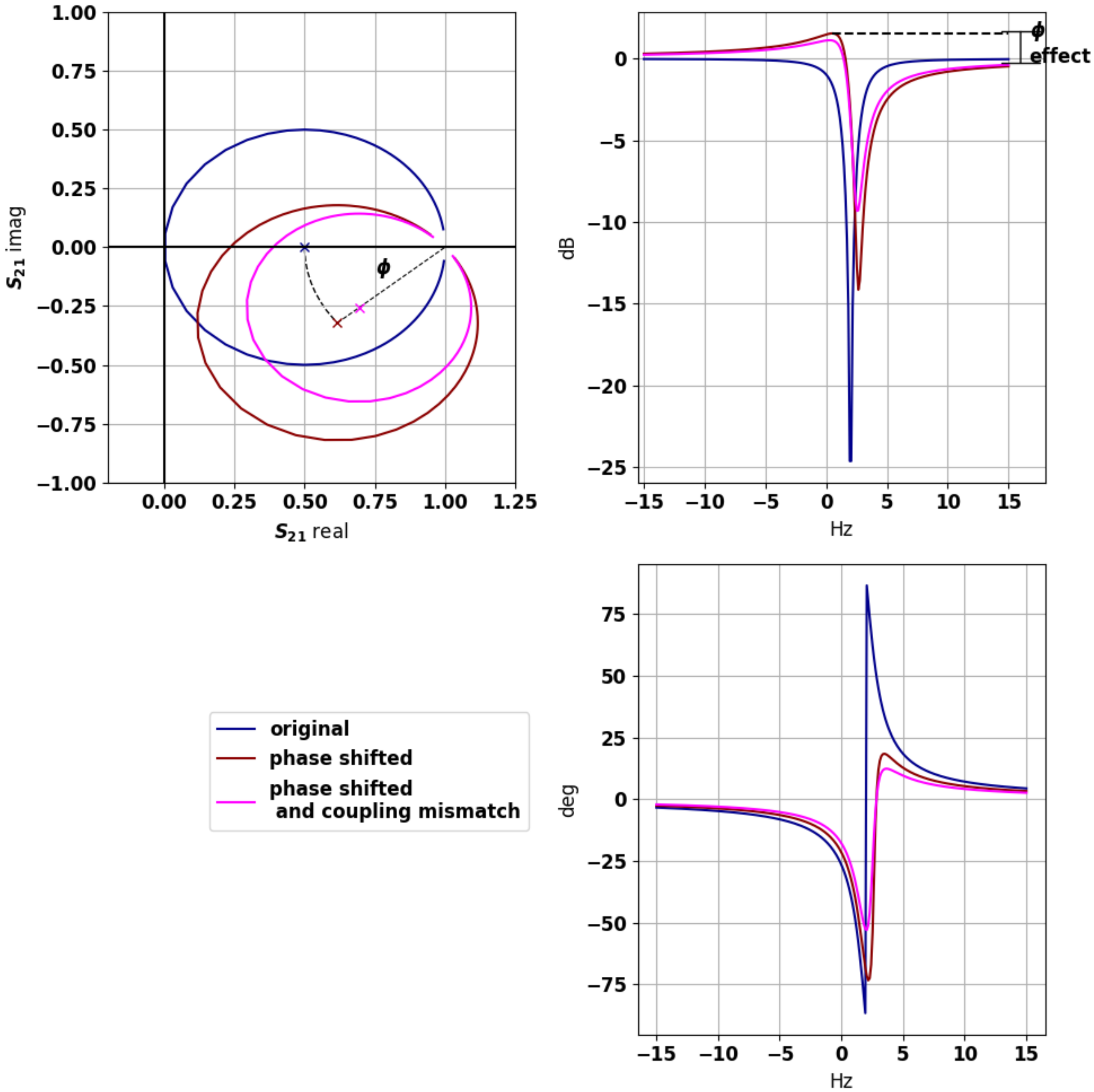

Figure 2.16: Responses of different terms for a notch resonator given by equation 2.44. The blue curve has $\phi = 0$, $Q_l = Q_c$, the red curve has $\phi = 30°$, $Q_l = Q_c$ and the magenta curve has $\phi = 30°$, $Q_l \neq Q_c$.

$$S_{21} = ae^{i\alpha}e^{-2\pi i f\tau}\left[1 - \frac{(Q_l/|Q_c|)e^{i\phi}}{1 + 2iQ_l(f/f_r - 1)}\right] \tag{2.45}$$

Equation 2.45 adds the external terms. The term a cause a change in the radius of the circle, but opposed to the effect of the ratio Q_l/Q_c the effect of a does not keep the point $(1,0)$ as an extreme value of the circumference, the extreme point now is $(a,0)$. In the magnitude visualization, this is translated as a vertical offset in the curve, and this term does not affect the phase curve.

The effect of the term $e^{i\alpha}$ causes another rotation that uses as a pivot the point $(0,0)$, so it generates a translation of the complete curve in the complex plane. This term does not cause changes in the magnitude graph but generates a vertical offset of the phase curve.

Finally, the expression $e^{-2\pi i\tau}$ models the cable delay response for different frequencies. This cable delay in the complex plane causes distortions in the circle shapes. This term does not affect the magnitude curve, and in the phase space, it is equivalent to adding a linear function with a slope proportional to the τ parameter.

2.4.3. KIDs readout power dependence

The other important parameter that affects the detector reading and is capable of modifying the resonator response is the readout tone power. This is not directly related to the standard resonator theory but is a specific feature of the superconductor resonator.

The injected power also affects the MKID response, mostly due to a non-linear effect of the kinetic inductance shown in equation 2.30. This power dependence causes a shift in the resonant frequency $\delta f_0(P)$ that depends on the power. Regarding the readout power, the MKID could be in three states: underdriven, overdriven, and with an optimal readout power level. When the MKID is in an underdriven state, increasing the readout power will shift the resonant frequency to higher values. When the readout power on the MKID is too high, it enters into an overdriven state. When the detector is in an overdriven state, the increase in the readout tone power causes a shift in the MKID resonant frequency to lower values. At the same time, when the MKID is in an overdriven state, the resonator stops being a Lorentzian curve and starts to show non-linear effects of the kinetic inductance, resembling a Duffing resonator response.

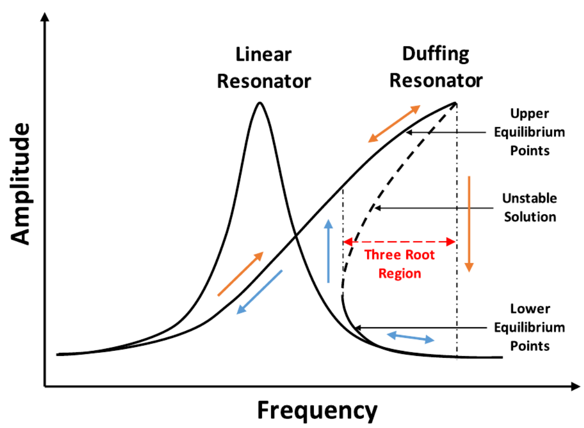

Figure 2.17: Standard Duffing resonator response. This response is due a x^3 non-linearity introduced in the standard resonating equation, causing the distortion in the resonant frequency. Image extracted from [15].

In an overdriven state, the nonlinearities of the kinetic inductance start to play a major role in the response of the MKID when a photon arrives, which finally means that the assumption that the resonance shift is linear with temperature is not valid anymore. On the other hand, the problem of being in the underdriven state is that Two-Level System (TLS) noise can be expressed as the relation in equation 2.46[16] where β is a value between $(1.5 - 2)$. So, in order to reduce the TLS noise, the power of the readout tone should be as high as possible, but without entering the overdriven state.

$$S_{TLS} = T^{-\beta} P_g^{-1/2} \tag{2.46}$$

2.4.4. Summary

In this subsection, the analytical model of a resonator was explored, leading to different visualizations of the resonator curves in different domains that make evident certain features of the resonator itself. In particular, for the MKID readout, we are interested in the mapping on the complex plane, where the resonator takes the form of a circle.

It was shown that for a given resonator with the same Q but a different resonant frequency, the circle remains the same, but it has a rotation around its center. As a single tone in the resonator curve is mapped to one point in the circle, if the resonant frequency changes, the point will rotate accordingly.

To make this type of measurement possible, the circle of the resonator has to be characterized to account for all the circle transformations in the complex plane that were described in this subsection.

Figure 2.18 shows the basic idea of the readout concept, where we only have a single point in the resonator, but since we have prior knowledge of the circle parameters, we are able to determine the overall rotation and therefore the resonance shift.

Figure 2.19 shows the diagram of the reading system, where IQ DACs generate the reading tones for each detector, and after the signal passes through the cryostat with the MKIDs, it is sampled by IQ ADCs. After the capture of the transmitted waveform, the data needs to be processed to extract the actual circle rotation.

It is important to note that this procedure has to be made for every detector, where each one has its own circle parameters and its own resonant frequency, and that the complete measurement has to be done simultaneously. So, the processing pipeline is not trivial.

In the next chapter, the AMKID camera and its new readout are presented, also the readout steps to determine the circle parameters are described.

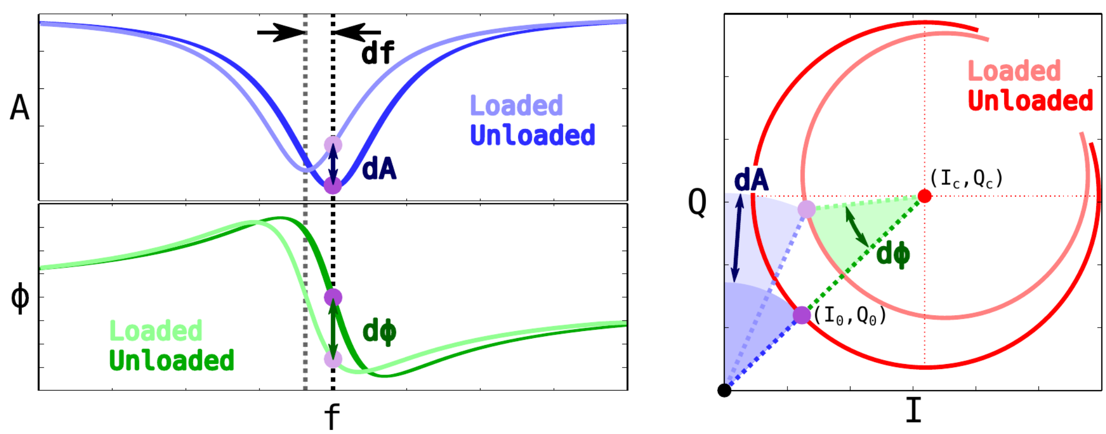

Figure 2.18: Example of the readout idea. With prior knowledge of the circle parameters (radius, rotation and center position), measuring a single point on the complex plane allows for the determination of the resonator status. Image extracted from [17].

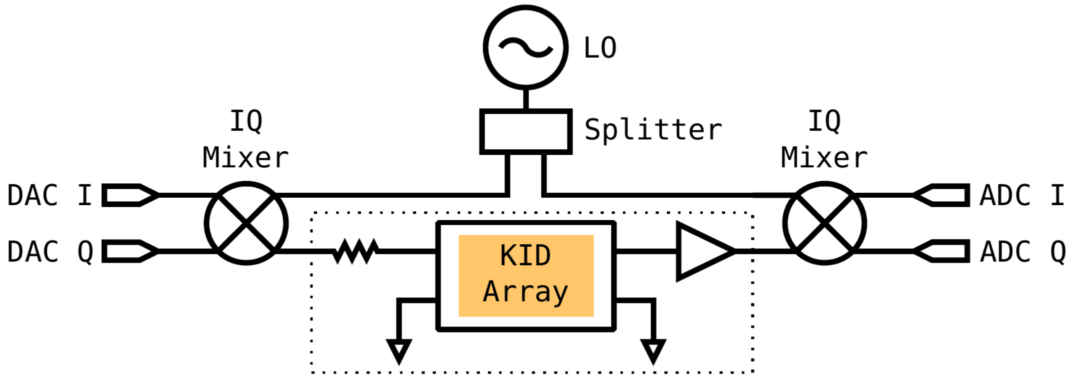

Figure 2.19: Readout Diagram. The IQ DACs generate a complex signal that contains the reading tones for each detector. After passing through the MKIDs line, the transmission is captured by a pair of IQ ADCs. Then the response of the line has to be processed to discount the complex plane transformations to extract the circle rotation. Image extracted from [17].

Chapter 3

Atacama Pathfinder Experiment (APEX) MKID camera

3.1. Telescope overview

Figure 3.1: APEX telescope at sunset. Image extracted from [18].

The Atacama Pathfinder Experiment (APEX) is a radio telescope located at an altitude of 5107 m on the Llano de Chajnantor in Chile. This location is considered one of the best places for submillimeter astronomy observations. The most significant limitation for submillimeter ground-based astronomy is the atmospheric absorption bands, which make the observation possible in certain frequency windows. The transmission of the atmosphere at the APEX high site can be seen in figure 3.2 [18].

As the name of the telescope implies, APEX was conceived to be a pathfinder for other submillimeter ground-based missions, and due to its nature as an experimental telescope, it is a test space for innovative instruments and techniques focused on radioastronomy.

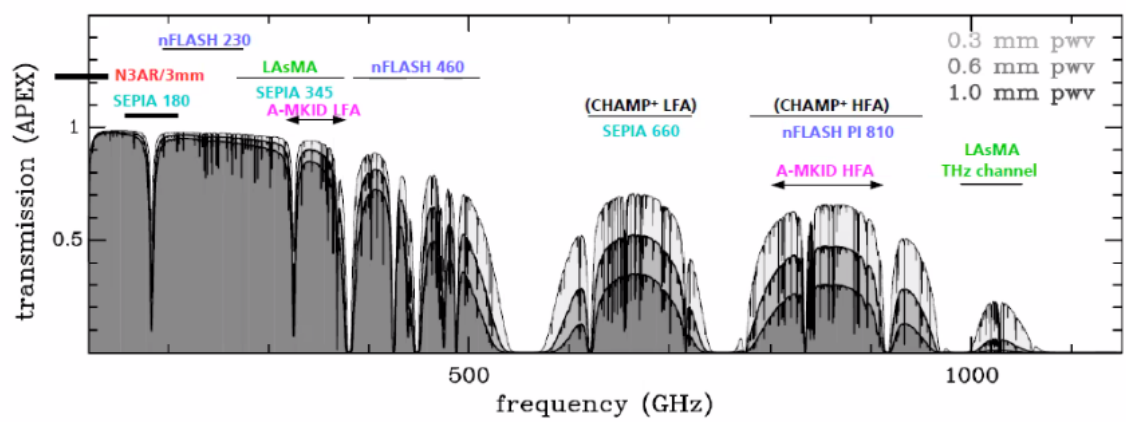

Figure 3.2: Transmission of the frequency bands at llano de Chajnantor and the bandwidths of the instruments placed at APEX in 2023. Image extracted from [19].

APEX was born as a collaboration between the Max-Planck-Institut für Radioastronomie (MPIfR), the Onsala Space Observatory (OSO) and the European Southern Observatory (ESO). APEX was installed and commissioned in 2005 and has been operational since then.

The telescope is a modified ALMA prototype designed and constructed by VERTEX Antennentechnik. It is a 12-meter single-dish Cassegrain antenna customized to have two Nasmyth cabins. The main reflector is composed of 264 aluminum panels that can be adjusted to correct surface errors to achieve a surface accuracy better than $20\mu m$ RMS. The Cassegrain cabin, just under the secondary reflector, was designed to allow wide field of view bolometer arrays, while the Nasmyths cabins are well suited to contain heterodyne receivers. To select the usage of the cabins, the telescope has a programmable arm with a mirror that can be placed in the optical path to deviate the signal to the Nasmyth cabins, as the diagram in figure 3.3 shows [20], where M1 and M2 are the Cassegrain antenna mirrors and M3 and M6 form a Gaussian telescope using the flat mirrors F4 and F5.

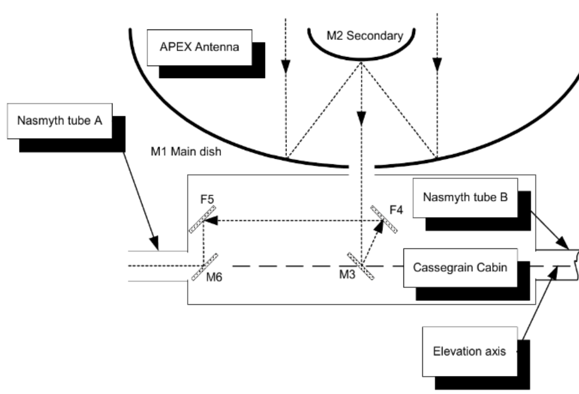

Figure 3.3: APEX optics diagram. Image extracted from [20]

3.2. APEX MKID receiver

3.2.1. A-MKID detectors

The APEX MKID receiver consists of a 24-line bolometer, where each line contains ≈ 800 MKID detectors. These detectors are grouped into two arrays that can observe one source at the same time: a low-frequency array (LFA) that has a bandwidth of $(330 - 360)GHz$ with 2800 pixels and a high-frequency array (HFA) working in the range $(800 - 900)GHz$ with 13800 pixels. The HFA and LFA have a hexagonal layout with a spacing of $1.1\lambda F$ and $1.2\lambda F$ respectively, generating a fully sampled image of the sky. To diplex the arrays, a polarizer grid is placed before the detectors, so the transmitted mode goes to the HFA and the reflected mode goes to the LFA.

The MKID detectors are produced by SRON/NOVA [21] using an antenna-coupled hybrid NbTiN-Al as the building block of the detector array. The hybrid MKID consists of a coplanar waveguide resonator, where the resonant frequency of each MKID is calculated using the equation $f_r = \frac{c}{4L\sqrt{\epsilon_{eff}}}$ where c is the speed of light, ϵ_{eff} is the effective dielectric constant of the CPW, and L is the resonator length. To enable a frequency multiplexing readout, each MKID has a different length, resulting in resonant frequencies in the $(4-8)GHz$ range. The narrow section of the MKID detector is connected to the feed of a twin-slot antenna, and efficient radiation coupling to the antenna is achieved by using Si lens arrays aligned in such a way that every MKID antenna is located at the focus of the lens. In operation, a set of filters is placed over the lens arrays to limit the bandwidth of the signals to a certain range.

In figure 3.4, photographs and diagrams of the MKID detectors can be seen, and in figure 3.5, there is a photograph of the filters used to limit the bandwidth of the array.

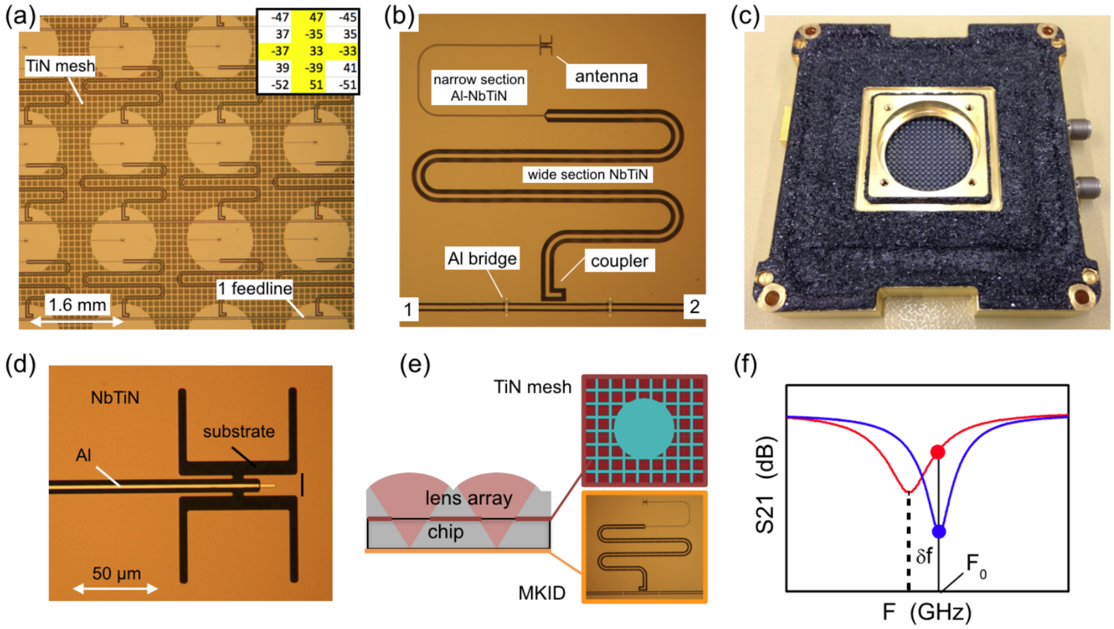

Figure 3.4: a) Photography of the backside of the chip detector. b) Zoom on a single detector. c) Photography of the lens array on the holder. d) Zoom on the antenna of one detector. e) Schematic of the cross section of the assembled detector. f) Response of one detector where blue curve is the equilibrium case and the red curve is the effect on the resonance due a photon absorption. Image extracted from [21].

Figure 3.5: Bandpass filters placed before the detectors.

3.2.2. A-MKID cryogenics

Due to sensitivity restrictions, the nominal temperature at the detector has to be $270mK$. This low temperature requirement is not due to the necessity of a superconductor state (the detectors have a higher critical temperature than this nominal temperature), but rather to keep the thermal noise of the cryostat environment that surrounds the detectors as low as possible.

To achieve a temperature of about $270mK$, the cryogenic system is composed of several temperature stages and layers. The external cooling is made by two $4K$ close-cycled pulse-tubes; one is used to cool down the optics at the interior of the cryostat and the cold amplifiers; the other pulse-tube is used to achieve a thermal bath temperature of $4K$ that surrounds a $He10$ cooler that is responsible for pushing the temperature under the $300mK$ at the detectors. The pulse tube coolers work with two temperature stages, the first one at $50K$ and the second one at $4K$.

The $He10$ cooler is a three-stage sorption cooler that utilizes different isotopes of helium as refrigerant; two stages use $He3$ and the other stage uses $He4$ (the name $He10$ comes from 3+3+4=10). The first $He4$ stage starts working when the bath temperature is at $4K$, and this layer cools the system until $1K$. This $1K$ serves as the thermal bath of the intermediate stage (I-stage) that uses $He3$ as refrigerant; in this layer, the temperature goes down to $300mK$. The final stage, called the ultra-cool stage, can achieve $260mK$ and is the place where the MKID detectors are mounted [22].

The initial cold-down procedure takes about of 60 hours; after this first cool-down, the subsequent cool-down process takes approximately two hours, with a holding time in laboratory conditions of near 19 hours. In total, there are 288 IF cables for the backend readout and electronics that came into the different cryostat layers, so avoiding thermal contact between the stages is a major problem that can only be detected after the 60 hours of cooling.

A diagram of the cryogenic system with the different stages can be seen in figure 3.6, and an actual photograph of the open cryostat is shown in figure 3.7.

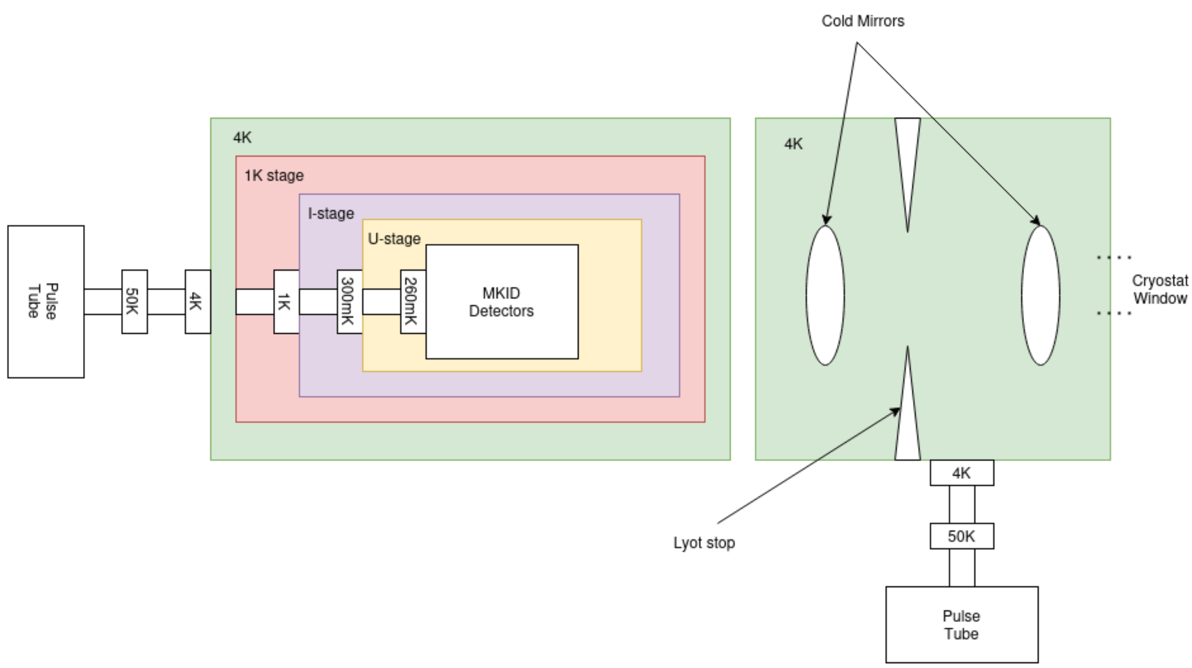

Figure 3.6: Diagram of the A-MKID cryogenic system.

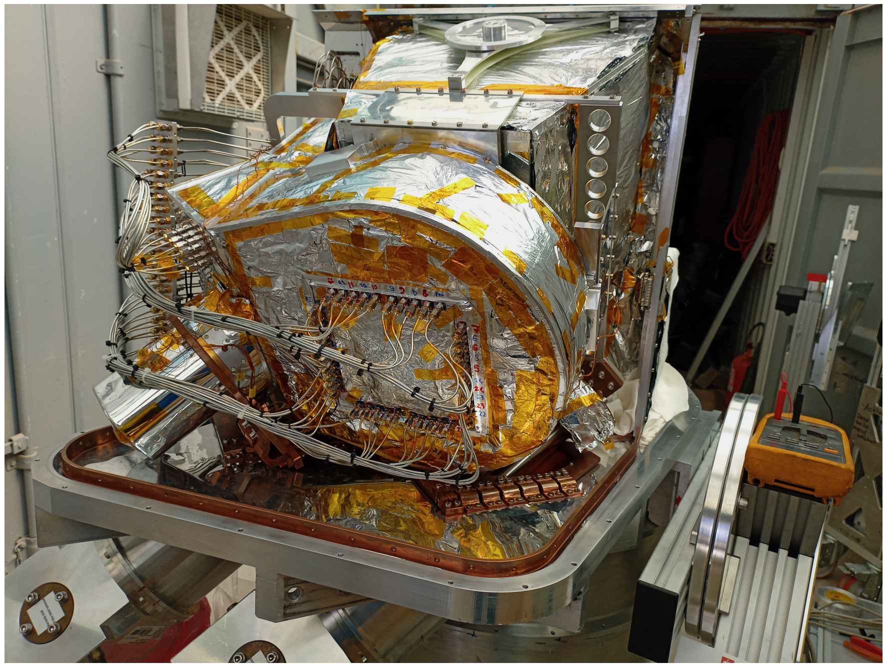

Figure 3.7: A-MKID cryostat opened.

3.2.3. A-MKID optics

The focal ratio of the secondary mirror of the Cassegrain antenna at APEX has an F-number of 8, and the resulting plate scale at the Cassegrain focus is approximately 2.15 arcsec. The goal of the optics is to have a diffraction-limited field of view of 16x16 arcmin^2 and that the complete optical system could fit in the APEX Cassegrain cabin. To have a diffraction-limited system means that the aberration induced by the optical system is low enough that the overall optic error is dominated by the Airy disk effect.

To satisfy these conditions, a pure reflective system was designed in the software Zeemax [23]. The system is composed of 4 mirrors with polynomial surfaces (M3, M4, M5, and M6) that are in charge of the magnifications of the focal plane image by a factor of approximately 3.6 to match the size of the detector chips. Also, two flat mirrors (F1 and F2) were introduced due to space limitations on the Cassegrain cabin. The use of the 4 mirrors allows to locate an intermediate focal plane at the cryostat window, but the optimization process of Zeemax causes aberrated beams at that intermediate plane that are corrected by the effect of M5 and M6 to arrive perpendicular to the detector plane.

A critical part of the optical system is the Lyot-stop, which is an aperture between M5 and M6 in the 4K stage that fits the beams that go to the detectors. The main task of the Lyot-stop is to terminate the light rays that do not come from the sky, preventing that non-astronomical warm temperature from going into the detectors and reducing the spillover effect.

An image of the optical system can be seen in figure 3.8, and figure 3.9 shows the simulated beams of HFA and LFA in the software GRASP.

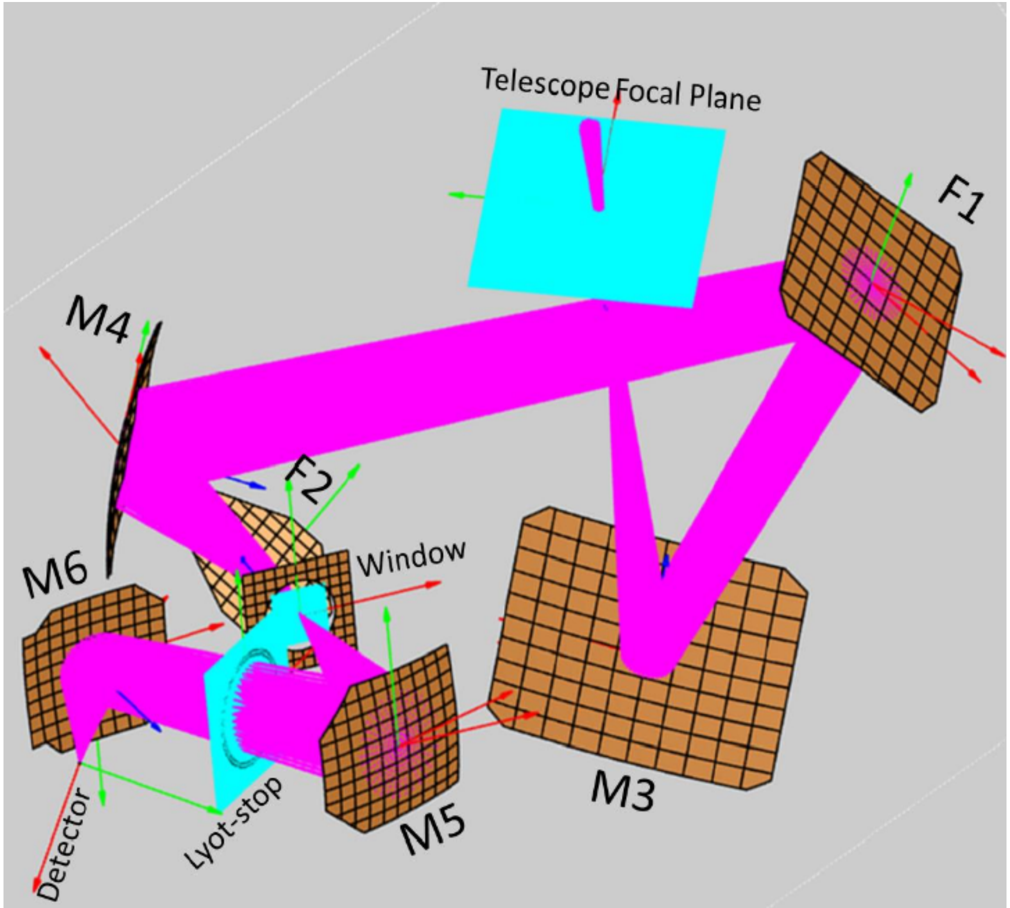

Figure 3.8: AMKID optical system layout. Image extracted from [23].

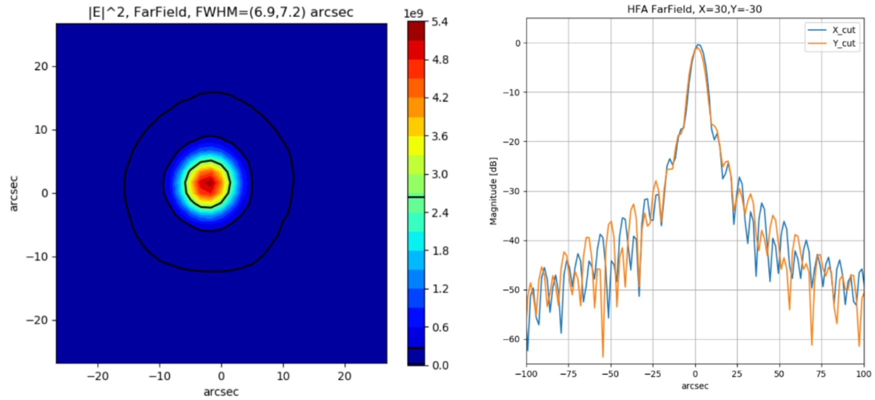

(a) HFA beam.

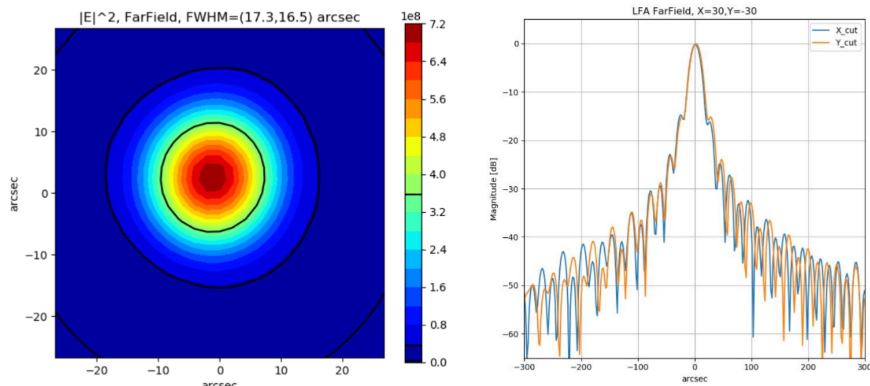

(b) LFA beam.

Figure 3.9: GRASP simulated on-sky beams. Image extracted from [24].

3.2.4. 2013 commissioning

A first commissioning of the A-MKID camera was made in December 2013, when the system was sent to Chile, mounted on the APEX high site, and tested. The results showed that the sensitivity of the detectors was worse than expected, making the bolometer uncompetitive compared with other instruments at that time (the LFA had three times worse sensitivity than expected and the HFA had six times worse). Also, there were problems with the optic alignment, and the beam quality of the high band was insufficient to make observations. Finally, the backend also presented problems since the individual power of the readout tones could not be set, so a lot of the read MKIDs were out of the linear zone.

These problems led the instrument back to the Max Planck Institute laboratories, where a campaign to fix them started in 2018.

First, a verification of the optics was made using the software GRASP and Zeemax, showing that the mirrors alignment is critical for good performance, needing a $0.2mm$ error in the mirrors position. For the new iteration, a metrology Faro arm is used to align the mirrors. This arm is connected to a computer that has a CAD model of the optical system and allows measuring the relative position of the mirrors and comparing it with the nominal values of the 3D position at the CAD model.

For the new A-MKID incarnation, new calibration methods were developed to measure the performance of the chip array in the laboratory, obtaining good sensitivity with values around $2mK\sqrt{s}$. The cryostat cabling was re-made, and systematic tests were made to achieve the

270mK temperature at the detectors in a consistent way. Tests were made to see the effect of magnetic fields over the cryostat, indicating that a magnetic shield is needed for proper operation. A new set of filters for the detectors was made to isolate the desired bandwidth, and advances in the software side were made, enabling a completely remote operation.

This thesis took place in the stage of verification of the second incarnation of the system in Bonn, Germany, and in the middle of the preparations for the commissioning at the telescope. Finally, the new A-MKID camera was sent to Chile in 2023, and the commissioning was in progress while this document was being written.

Figure 3.10: AMKID installation in 2023. Photo after lifting the cryostat with APEX crane for the installation at the Cassegrain cabin.

3.3. A-MKIDs readout

The 2013 A-MKID readout was composed by the XFFTS boards built and designed by the MPIfR [25]. For this project, the XFFTS are in charge of the integration of the signal in the time domain, then the data is passed into a computer that performs a standard FFT, makes the circle transformation for the phase reading, and finally sends the data to a merger computer.

For the new incarnation of the A-MKID camera, a new prototype backend was designed by the MPIfR.

This new backend is based on a heterogeneous design that mixes the huge parallelization capabilities of an FPGA with the flexibility of a GPU. Both technologies target as a main feature the parallelism of tasks in order to speed them up, but the selected method of each technology has its own advantages and disadvantages depending on the application that the programmer wants to develop.

3.3.1. Field Programmable Gate Array (FPGA)

Field Programmable Gate Array (FPGA) are programmable integrated circuits consisting of logic blocks that can be configured and interconnected to generate a specific digital circuit. Figure 3.11 shows a basic architecture of an FPGA, where different types of programmable blocks are spread inside the chip.

The typical blocks in an FPGA are the configurable logic blocks (CLB), which in a simplified way are a set of look-up tables (LUT) that can generate any boolean logic; block RAMs that are small and fast memories distributed around the chip; DSP blocks that perform mathematical operations in an efficient way; and routing channels that enable the connection between different blocks. Inside these routing components, there is a special kind that is used for the clock distribution. Besides these basic blocks, there are also specialized blocks to interface common signals, like for example, the serializer-deserializer (SerDes) transreceivers used for multi-gigabit high speed communications like PCIe, SATA, 10Gbe, Aurora, JESD204-B, etc.

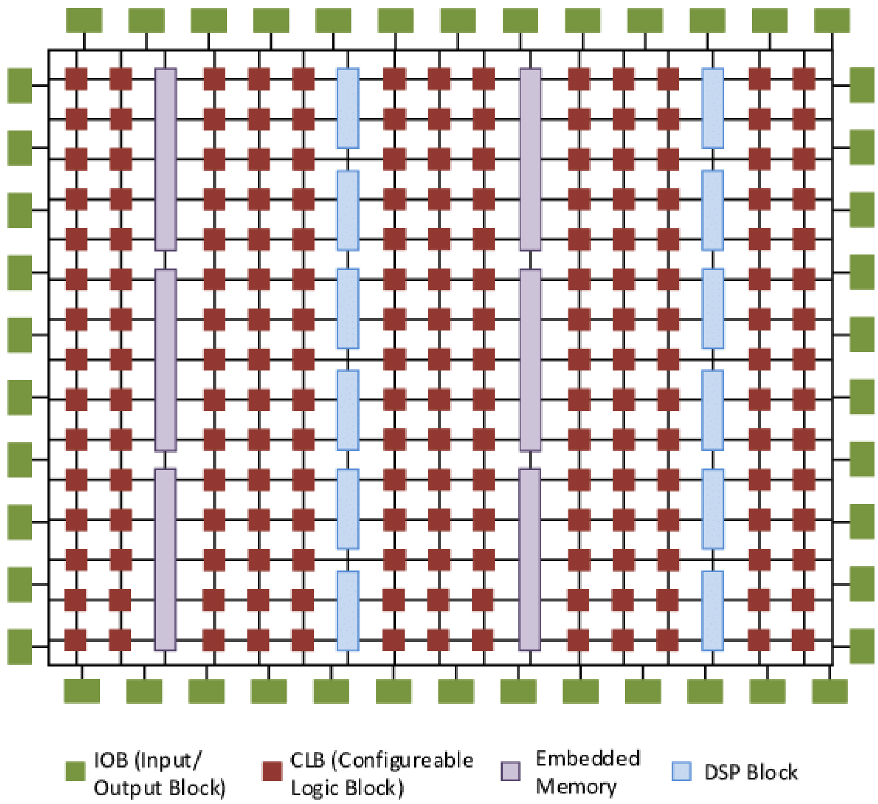

Figure 3.11: Basic representation of the logic inside an FPGA. Image extracted from [26].

The difference between FPGAs and other types of programmable devices is that the FPGA is inherently programmable hardware in the sense that there is no predefined instruction set, and the final outcome of the whole programming and compilation is a digital circuit that uses as building blocks the basic blocks inside the FPGA. This deviates from the tendency of the processors, that are based on a fast central unit, while the FPGAs are based on several small digital circuits that can be interconnected to obtain the desired result. This non-centralized approach enables the design of circuits that run in parallel, speeding up the computation even if the main system clock of the FPGAs is slower than the current processors. The distributed nature of the FPGAs allows that parallel circuits can run synchronously, and there are no missing information lapses or halt states when the system is running, meaning that the programmer has control over what happens in every clock cycle.

These features make FPGAs an attractive technology for real-time processing of huge amounts of data, like the ones produced in astronomy. It is common to find high-speed digitizers connected to an FPGA that process the real-time data and reduce its rate to allow offline storage. As an example, in a heterodyne receiver, the standard backend calculates an FFT followed by a power spectrum integration stage and finally sends the integrated spectrum to be stored for offline processing.

3.3.2. Graphics Processing Unit (GPU)

A graphics processing unit (GPU) is a hardware accelerator that was initially conceived to speed up computers and image processing. Given the high number of operations that a GPU can handle, their application scope has been expanded to other areas, such as for example, deep learning fields.

The GPU technology evolved by the hand of the video game community, which is constantly demanding more computational power for the rendering and rastering of an image in real time, so the gaming user has an immersive experience.

Since the GPU has to be able to update each pixel on the screen in real time, the GPU architecture has a parallelized approach where a small processor is in charge of a portion of the overall calculation. In this sense, the GPUs are multithread-oriented devices, and most of the leverage of the execution time is obtained if the algorithm that the programmer wants to implement can be separated into these threads.

Figure 3.12 shows the standard diagram of a GPU that is formed by an array of streaming processors (SPs) that share control logic and instruction cache. Each GPU also comes with a global memory DRAM that is used as the frame buffer by the GPU. The main task of the global memory is to transfer information from or to the device memory. Usually, the devices are equipped with Direct Memory Access (DMA) hardware, allowing efficient data transfer without the host CPU intervention.

GPU programming is based on the Single Instruction Multiple Data (SIMD) paradigm, which means that each SP will perform the same operation but over different portion of the data. So, the GPU architecture supposes that the overall operation can be decomposed into partial results that are calculated in the SPs, and that the final result is obtained by mixing those intermediate results. Then, the power of the GPUs does not rely on the computational power of each SP but on its quantity. For example, the NVIDIA GeForce RTX 3080 has 68 SMs with 128 SPs, so the total number of threads that can be run on this GPU at the same time is 14824.

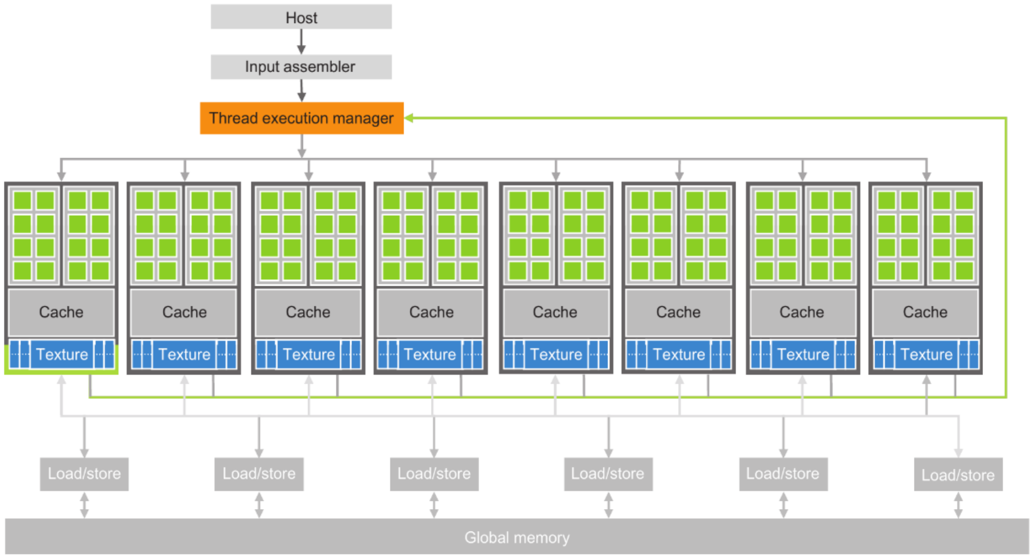

Figure 3.12: Diagram of a GPU architecture. Image extracted from [27].

An important topic in multithreading programming is the synchronization mechanism of the launched threads. Since the threads run independently, they can finish their computation at different times, and this could lead to a race condition and unpredictable results. One reason to group several SPs is to be able to share intermediate results between SPs, but it is the programmer's task to use a safe mechanism to synchronize the threads.

In 2007, NVIDIA released Compute Unified Device Architecture (CUDA), which is a parallel computing platform and application programming interface (API) built for NVIDIA GPU programming. CUDA acts as a software layer to access the GPU's virtual instruction set and enables the development of custom programs that can run using the GPU resources.

CUDA was designed to be used in conjunction with C, C++, and Fortran programs and follows the same nomenclature and conventions for GPU functions and primitives.

3.3.3. New A-MKID readout: U-board

As stated before, FPGAs have hard real-time capabilities since the digital circuit is actually generated in the chip via interconnection and programming of the primitive blocks. At the same time, this means that the programmer should work at a low abstraction level, making it difficult and time-consuming to implement complicated algorithms.

Another important point to notice is that FPGAs are designed to work using fixed-point arithmetic since floating-point usually uses dedicated hardware. The use of fixed-point arithmetic needs a careful bit growth scheme and simulations to verify the correctness of the model.

In the other extreme, GPUs use multithreading as a parallelization method, decomposing the problem and solving each small problem using a SP. Each SP has its own Arithmetic Logic Unit (ALU) and cache memory, and in most cases, they allow floating-point operations. The start of the GPU execution is given by the host device request, then it necessarily involves the intervention of the host operating system, which generates latency and jitter that cannot be allowed in a hard real-time system.

Since GPU programming is oriented toward multithreading, which is a common paradigm in computer science, it is more accessible for programmers than FPGAs. Also, CUDA is a

C++ dialect, which is a high-level language, enabling the abstraction of complicated algorithms in an elegant way.

The U-board was designed and built at the Max Planck Institute and is a heterogeneous device that uses an FPGA connected to a Jetson module via a PCIe bus. The first U-board prototype uses a VCU118 evaluation board from AMD and a Jetson Xavier AGX from NVIDIA.

The VCU118 board contains a Virtex Ultrascale+ FPGA and several peripherals connected to it. For this prototype, the most important components of the FPGA are the DDR4 memories populated across the board, the FMC+ connector and the PCIe connector.

The Jetson modules from NVIDIA are System-On-Modules (SOM) that contain CPU, GPU, DRAM, etc. The processor is an 8-core ARM with 32GB of LPDDR4, a GPU with 512 processing cores and 64 tensor cores. The SOM can be connected to an extension board that gives access to 16 lanes for PCIe4 and a RJ45 connector for communication.

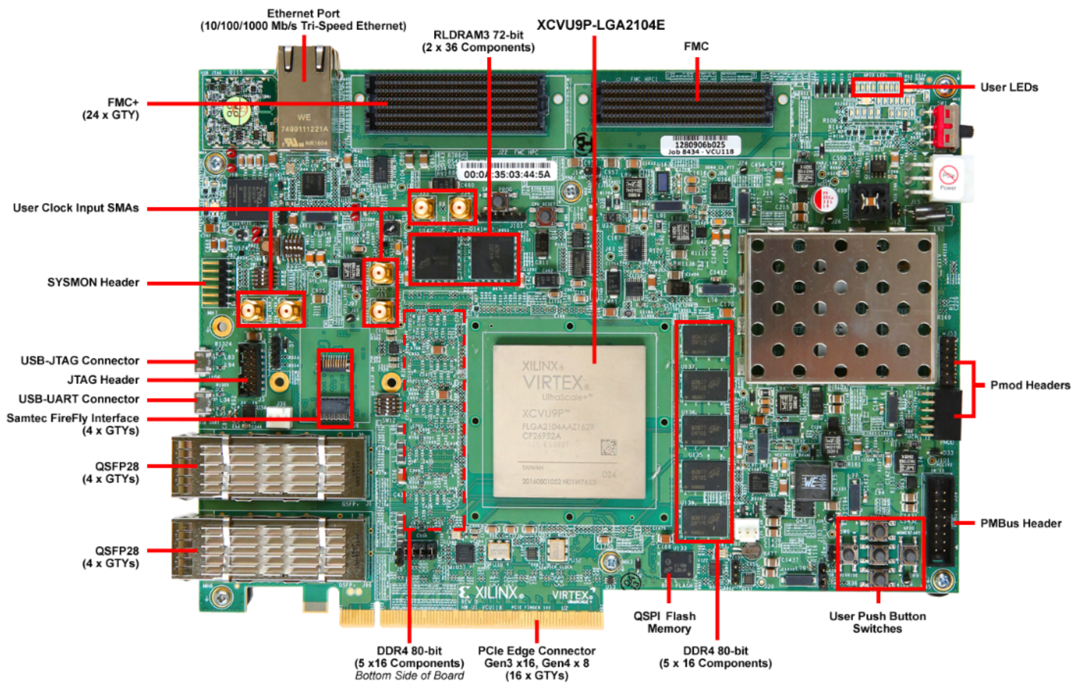

Figure 3.13: VCU118 diagram. Image extracted from [28].

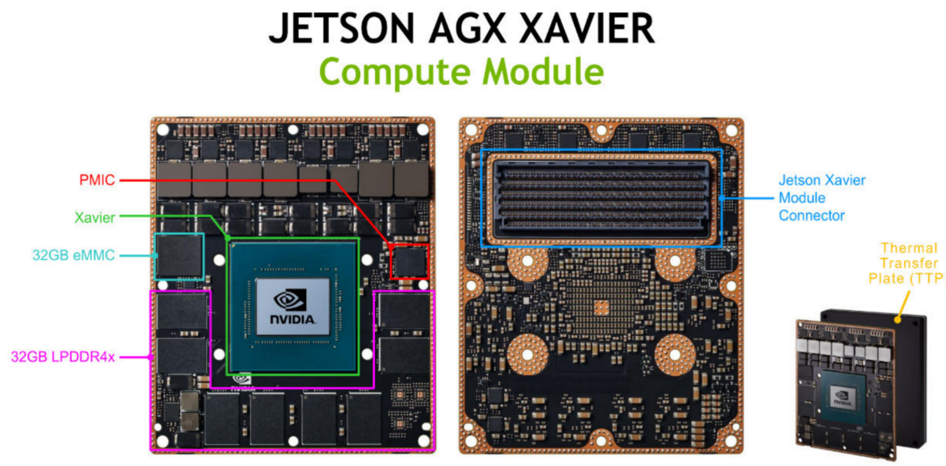

Figure 3.14: Jetson AGX Xavier diagram. Image extracted from [29].

FMC stands for FPGA Mezzanine Card, which is an ANSI/VITA standard used for high-speed peripherals connected to an FPGA. The FMC+ connector of the VCU118 is mapped to the GTY transreceiver, which supports a line rate of 32.75 Gb/s. The AMD transreceivers technology are ASICs inside the FPGA that are in charge of the physical layer of high-speed serial communications, message encoding/decoding (for example, 8b/10b), comma detection, clock recovery and deserialization/serialization of the data.

The U-board utilizes the FMC+ connector to form a link with the ADCs and DACs of the board. The custom board designed by the MPIfR consists of an ADC12DJ5200 that is a 12-bit ADC that can run up to 10.4 GSPS in single or dual channel mode, a slower ADC08DJ3200 that is a 12-bit with a maximum sampling rate of 6.4 GSPS in single-line mode, and a DAC AD9182 with 16-bits that supports up to 12.6 GSPS in single-line mode.

As the MKID readout system needs coherent phase reading, the DACs and ADCs use the same clock and the sample rates are set to 2 GHz. The DACs are used in dual-line mode and the ports represent the data in IQ format, so they can be upconverted via an IQ mixer and then go into the cryostat where the MKIDs are. After passing through the detector feedline, the signal goes to an IQ mixer downconverter and finally into the ADCs, which receive the downconverted complex IQ data.

A summary of the U-board digitizers capabilities and the configuration used for the A-MKID readout can be found in table 3.1.

Table 3.1: U-board digitizers summary.

	single line GSPS	dual line GSPS	A-MKID configuration	bits
ADC12DJ5200	10.4	5.2	2GSPS dual line	12
ADC08DJ3200	6.4	3.2	2GSPS dual line	16
AD9182	12.6	6.4	2GSPS dual line	16

The concept of the U-board for the A-MKID readout is to load the desired waveform with the MKIDs tones in the DRAM memory, stream the waveform to the DACs, and read the information back with the IQ ADCs. To determine the change in the resonant frequency, we are only interested in certain frequency components, so it is natural to calculate an FFT. The FFT is calculated in two stages: the first one on the FPGA and the second one on the GPU. The process is based on the Cooley-Tukey algorithm, where large FFTs can be computed by using smaller FFTs.

The decimation in frequency implementation of the FFT is shown in expressions 3.1, 3.2, 3.3 and 3.4, where it can be seen that an FFT of size N is being made by an DFT of size $N/2$. This method can be extended to obtain the typical butterfly structures that can be seen in figure 3.15 where it can be noted that the output of the FFT is unsorted.

$$X_k = \sum_{n=0}^{N-1} x_n e^{\frac{-2\pi i}{N}nk} \tag{3.1}$$

$$= \sum_{n=0}^{N/2-1} x_n e^{\frac{-2\pi i}{N}nk} + \sum_{n=0}^{N/2-1} x_{n+N/2} e^{\frac{-2\pi i}{N}(n+N/2)k} \tag{3.2}$$

$$= \sum_{n=0}^{N/2-1} x_n e^{\frac{-2\pi i}{N}nk} + e^{\frac{-2\pi i}{N}N/2k} \sum_{n=0}^{N/2-1} x_{n+N/2} e^{\frac{-2\pi i}{N}(n+N)k} \tag{3.3}$$

$$= \sum_{n=0}^{N/2-1} \Big(x_n + (e^{\frac{-2\pi i}{N}})^{N/2k} x_{n+N/2}\Big) e^{\frac{-2\pi i}{N}nk} \tag{3.4}$$

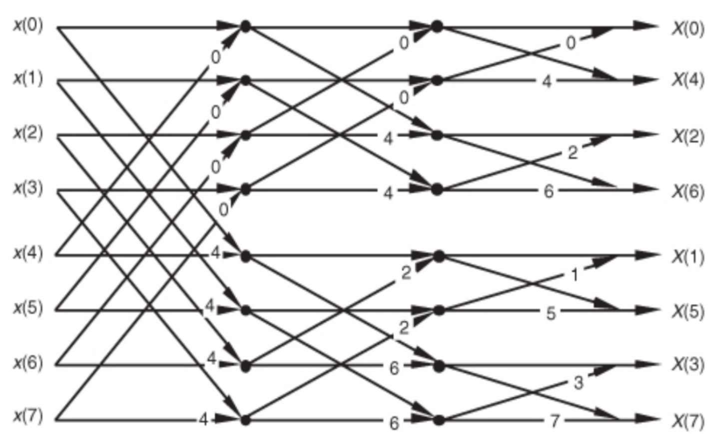

Figure 3.15: Typical butterfly diagram of a DFT. Image extracted from [30].

In the A-MKID U-board 16 pipelined complex FFT of $2^{16} = 65536$ samples are computed inside the FPGA and written into the Jetson memory via a DMA. In the Jetson, the GPU uses the computed FFTs to calculate a 2^{20} FFT via the Cooley-Tukey algorithm. The kernel of the Jetson is configured in such a way that the GPU has quick access to the addresses where the FPGA writes the FFT data, so the transaction is made with minimal OS intervention, keeping most of the data transfer work on the PCIe bus.

With this scheme, the readout has a frequency resolution of 3.9 kHz, but since in the A-MKID readout only certain frequency channels contain interesting information, when the system is up and running, the FPGA passes only the necessary channels to the GPU, saving computation time on the GPU side and avoiding bottlenecks.

After the computation of the FFT channels, the GPU transforms the data into the circle domain and is in charge of making the integration of the collected data. As mentioned previously, all this computation is done in floating point arithmetic, and for the integration, the user can set the weights of a determined type of filter instead of relying on the typical averaging filter.

Figure 3.16 shows the main idea of the U-board backend for the A-MKID readout, and the real implementation of the board is in figure 3.17.

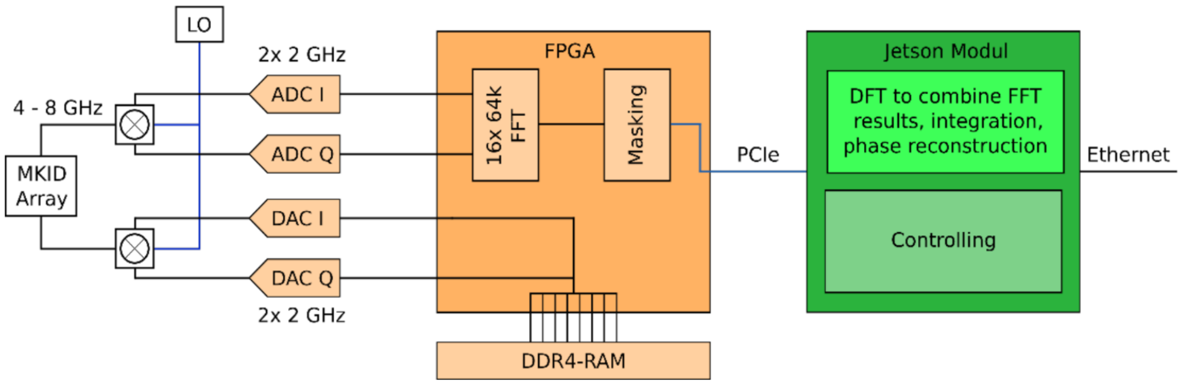

Figure 3.16: Simple diagram of the A-MKID U-board concept. Image extracted from [31].

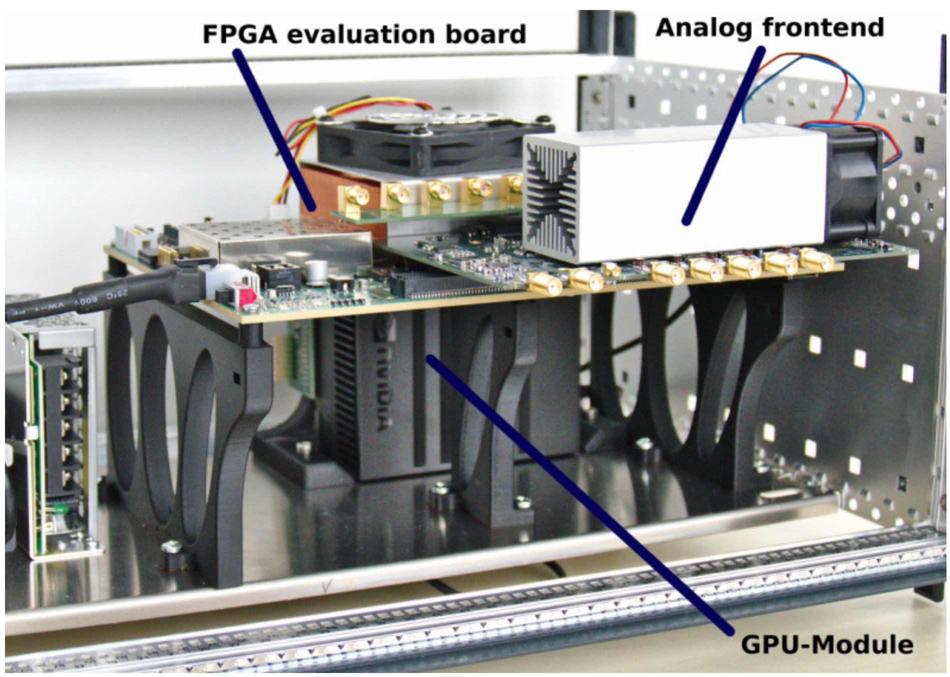

Figure 3.17: U-board prototype. Image extracted from [31].

3.4. A-MKID readout steps

Now that the U-board concept has been presented, the next subsections will present the steps involved in the actual A-MKID reading and the characterization stages that need to be done before the reading itself.

3.4.1. ADC-DAC calibration

The 2 DACs are running at 2 GSPS, and they are being used in IQ mode, giving a total bandwidth of 4 GHz. The data coming out from the DACs passes through a set of warm amplifiers and digitally controlled attenuators before going into an IQ mixer with a local oscillator near 6 GHz, obtaining a signal in the (4–8) GHz range[2].

The upconverted signal enters to the cryostat and passes through the line, reading the resonances. At the output of the cryostat, the signal is amplified by a set of cold amplifiers. Outside the cryostat, the signal gets into an IQ mixer, using the same LO as the upconverter in order to maintain phase coherency. After the downconversion, the signal is filtered and passes through another set of digitally controlled attenuators to finally reach the ADCs.

As the IQ mixers do not behave ideally, the first step is to measure their response for different values of phases and amplitudes that came out from the DACs. For that the slow ADC of the U-board receives the upconverted signal and decides the best set of amplitude and phase values for different frequency ranges.

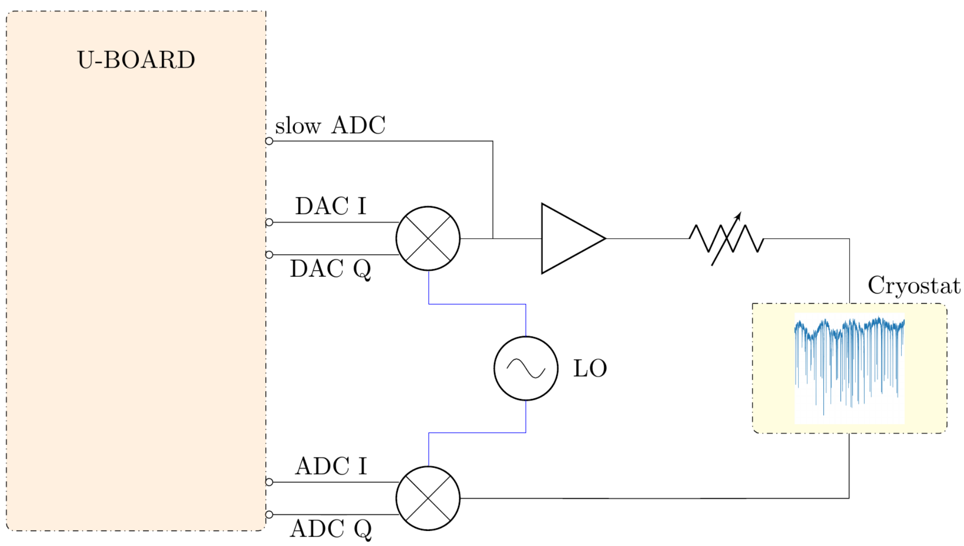

Figure 3.18: Readout connections diagram.

3.4.2. Bandpass search

In this bandpass search, the system makes a rough search of the MKIDs positions that is refined in the following stages. For the bandpass search, the bandwidth is divided into a certain number of zones, and in each iteration, the DACs inject an equally spaced number of tones in the given zone at once. Since MKIDs are sensitive to the total power on the line,

[2] The actual LO frequency will vary a little bit from line to line because of how the MKIDs are distributed after the manufacturing process.

the bandpass search method causes movements on the resonances, and some artifacts in the readout are generated. For example, the ADCs measure sectors that have positive gains, but as stated before, this gain is an artifact that does not involve the MKID positions.

To find the MKIDs positions, regions with convex curvature are searched. To avoid false detections given by the noise, a filter is applied to smooth the data, and the candidates are selected, finding the positions where the second derivative is positive and the dip of the signal is higher than a certain threshold.

On figure 3.19, it is shown a bandpass search output that has the MKIDs preliminary positions. The figure also shows the artifacts produced by the method, but it does not affect the MKIDs searching algorithm.

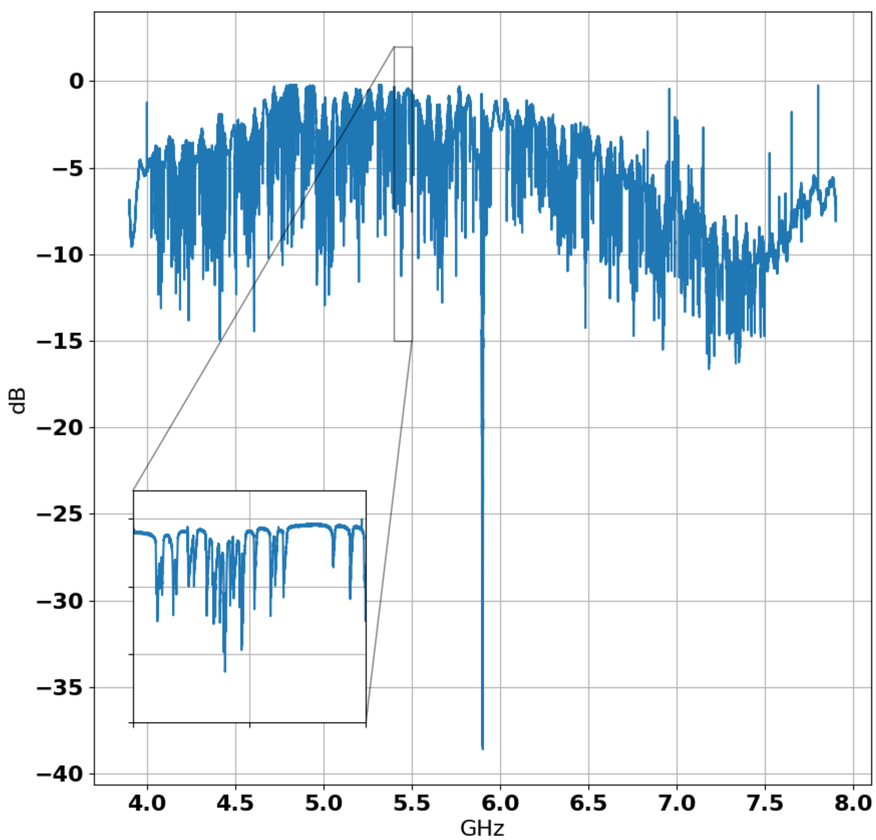

Figure 3.19: Bandpass search data.

After obtaining the preliminary MKIDs positions, a tone is placed in that frequency channel, preparing a posterior fine-tuning search. Beside the MKIDs tones, the readout also injects tones in zones that do not contain MKIDs in order to correct for the cables, amplifiers, etc. These additional tones are referred as blindtones and are used to correct the global variations that affect the overall system, like for example cryostat vibration. The readout injects around 40 blindtones, 20 per side band, and the positions are selected such that they sample the whole sideband while not being too close to the MKIDs.

3.4.3. Frequency-sweep and circle calibration

With the tones placed in their preliminary positions, a second search is made by setting a frequency sweep in the LO generator, typically around 2 MHz of its nominal frequency. Since the LO is shared between the upconverter and downconverter, the information is being recorded in the same FFT channel, but the RF information will be changing with the LO frequency, generating the fine search. The resulting data from the frequency sweep is shown in figure 3.20, where it can be seen that the power data is shaky, the phase data contains the phase delay from the cable, and the circle in the IQ plane does not look like a circle. To address these issues, the blindtones can be used to calibrate the data. First, the blindtones are grouped depending on their corresponding sideband. For each sideband, the average response of the blindtones is taken as a reference, and then the frequency sweep data from the MKIDs is divided by that reference. The data after the blindtone calibration can be seen in the figure 3.21.

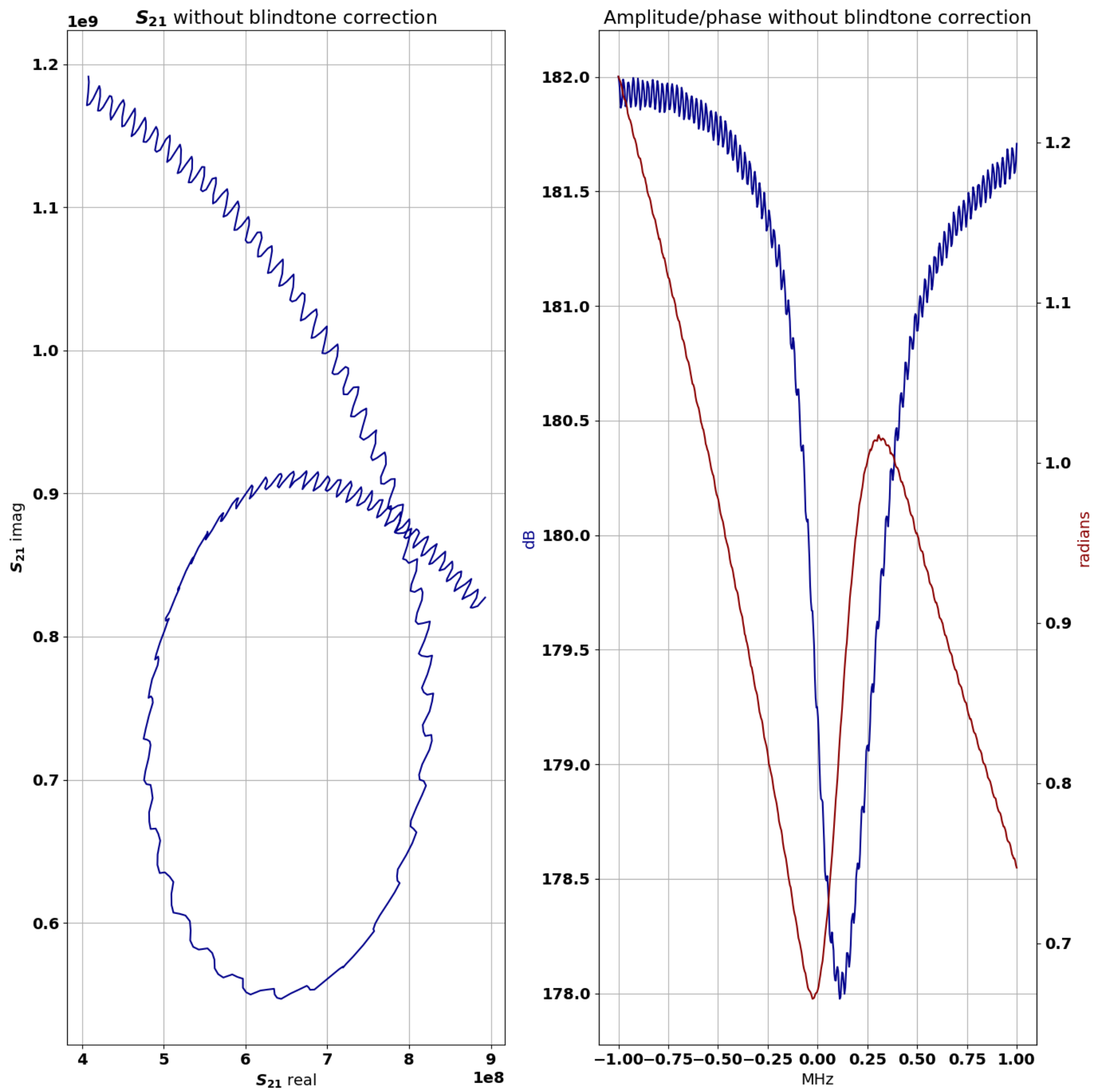

Figure 3.20: Frequency sweep without blindtone calibration.

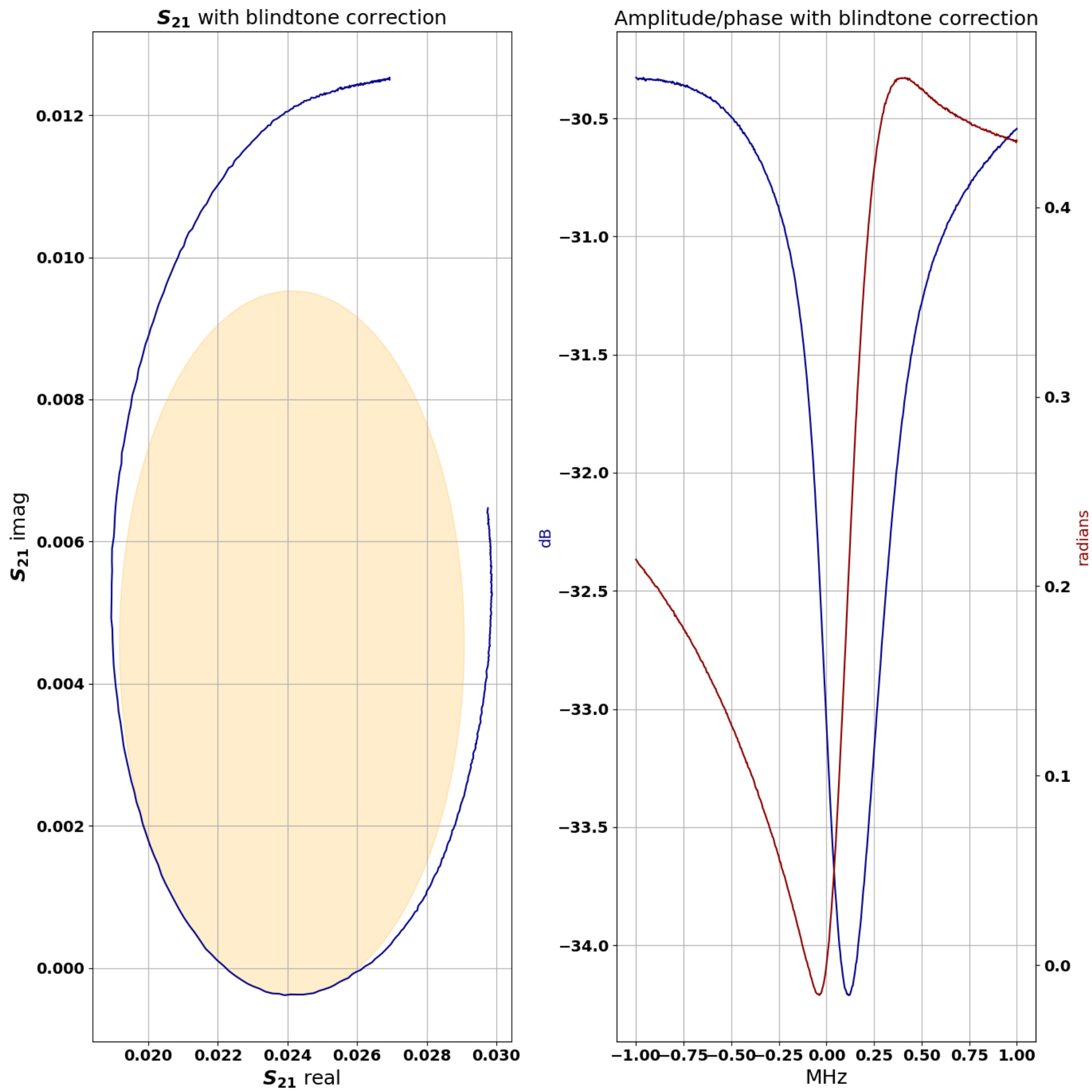

Figure 3.21: Frequency sweep with blindtone calibration.

With the calibrated IQ data, a fit can be done to find the most appropriate circle for each MKID. As mentioned in section 2.4.2 the circle could have moved its center, changed its radius, and rotated around the complex plane, the goal of this step is to find the inverse transformation. First, the circle center will be moved to the origin of the complex plane, the radius will be normalized and the circle will be rotated in order to have the current position at 0°.

These circle parameters are stored in the Jetson memory, to calibrate the samples that are being measured in real time. After this calibration stage, when the GPU obtains a sample, it first corrects it using the blindtones, then applies the circle transformation, calculates the corresponding phase rotation of the complex data and finally sends the data via a TCP port.

For debugging purposes, the raw IQ data, without blindtone corrections and circle calibrations, is also sent via another TCP port to have the raw data and to be able to process it offline.

3.4.4. Power-sweep

Each MKID has its own optimal readout power; if the tone power is less than optimal, there will be additional noise in the reading, and if the power is higher, it could lead the MKID to an overdriven state where the non-linear effects of the inductance start to dominate, and then the linear relation between resonance shift and temperature is no longer valid.

As stated before, ideally the power level at the readout tones should be as high as possible without entering the overdriven state. Luckily, there are certain signs that can be used to detect the transition to the overdriven state. In the underdriven state the MKIDs will shift up the resonant frequency when increasing the power of the signal, whereas in the overdriven state, the resonant frequency starts to go down. Another characteristic sign of the overdriven state is that the IQ circles start to have discontinuities and breaking points, as figure 3.22 shows for the brown curve.

For the U-board, the selected method to find the optimal power is to make several frequency sweeps at different power levels and search for where the movement of the resonant frequency changes direction. Figure 3.23 shows there is a turning point in the resonance evolution when the power gets increased.

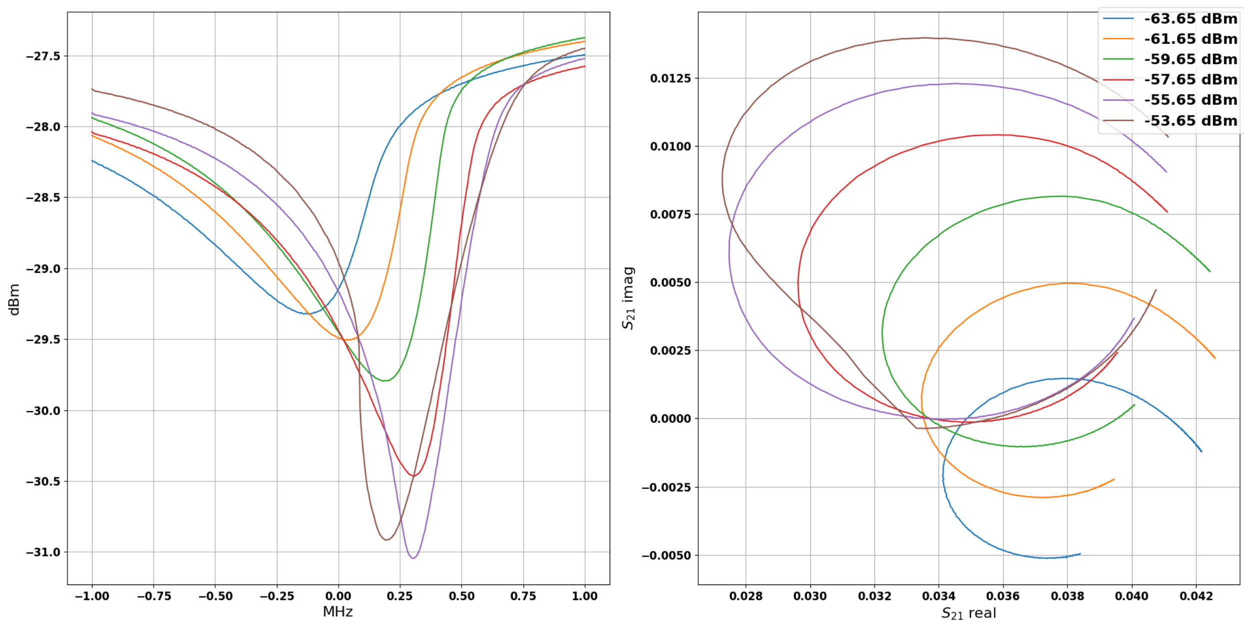

Figure 3.22: Power-sweep example. In this example the optimal curve of displayed set is the red curve with readout power of −57.65 dBm.

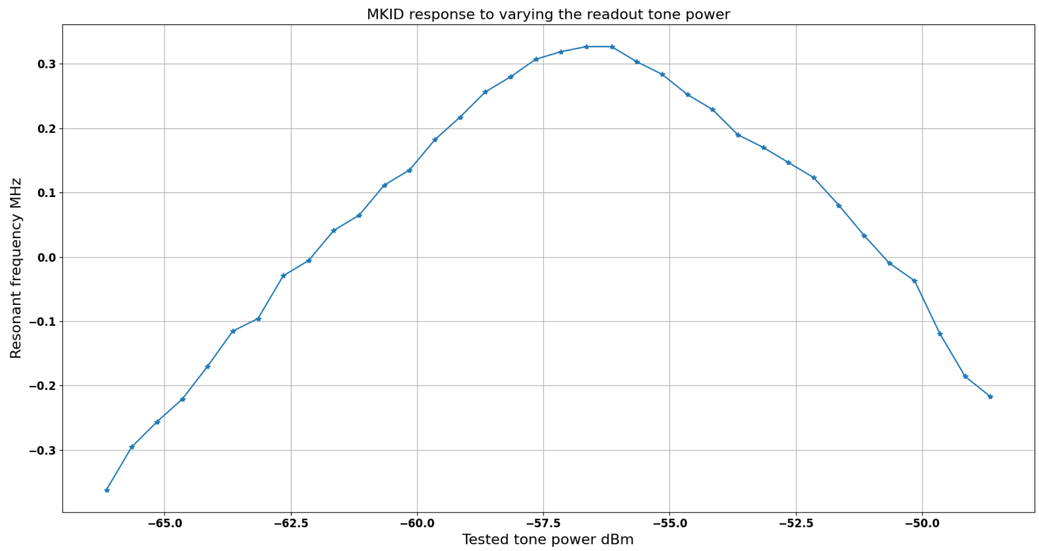

Figure 3.23: Evolution of a MKID resonance when varying the power of the readout tone.

When the optimal power for each MKID is found, all the MKIDs need to be re-characterized to obtain the circle parameters for the new setup.

3.4.5. MKIDs reading and control

When all the previous stages are done, the system has the resonant frequency, the optimal power level and the circle parameters that convert the IQ data to the unit circle for each MKID in the line.

As mentioned previously, the Jetson module has access to those parameters, so when reading the information, it first performs a blindtone correction followed by transformations to the circle domain, where the rotation of the circle is measured. After the circle phase rotation is computed, the Jetson accumulate a given integration time and after sends the integrated data to a control PC via a TCP port. Simultaneously, the IQ raw data is sent to the control PC, where the corrections can be made offline.

The user should only care about keeping the reading MKID in the linear zone of the circle domain, where the linear relationship with the temperature is valid. When most of the MKIDs are outside the linear range, a new frequency sweep needs to be done to characterize the circle parameters again and evaluate the tone position. The rule of thumb is that if a MKID moves over π in the circle domain, then it is outside of the linear zone and it needs to be recalibrated. Figure 3.24 shows an example of the available linear zone of a MKID colored yellow. If the detector goes outside that region, that is an indication that the detector needs to be re-calibrated.

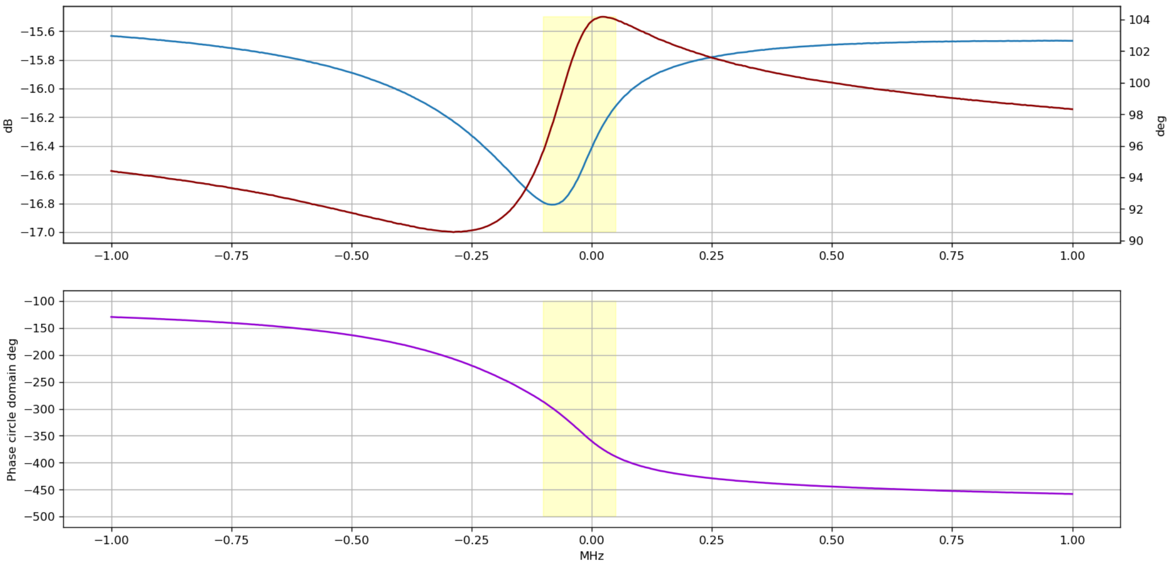

Figure 3.24: Example of the linear zone of a MKID colored in yellow. Outside that range the MKID information is not useful.

Chapter 4

Double tone MKID readout implementation and tests

With the new computational power and versatility that the U-board offers, the idea of this experiment was to investigate if the sensitivity of the A-MKID readout increases when the readout system uses two tones to read the phase information instead of the standard single-tone reading. The hypothesis is that when having two tones measuring the same resonance shift, the integration time will double, increasing the sensitivity of the system.

The next subsections explain how the double tone system was implemented in the U-board and how the sensibility test was made, using the NET of the different configurations as a comparison metric.

4.1. Double tone readout implementation

4.1.1. KIDs candidates selection process

As previously mentioned in Chapter 3, even if the U-board counts with a huge computation power, the number of detectors that can process is less than 2^{20} channels. After the preliminary band-pass search that finds the MKID resonances, a single tone is placed in each detector, then just certain channels are passed to the GPU to calculate the needed FFT channels. The GPU can support up to ≈ 1800 MKIDs being processed at the same time; over that number, the GPU have problems since is not able to allocate enough memory.

The memory limitation is not a problem for the single-tone readout since there are ≈ 800 MKIDs per line and the GPU has enough space for them. But since there was flexibility in the amount of MKIDs that the system could process, the resonance finding algorithm was too relaxed, causing non-MKIDs to be classified as actual MKIDs[3]. To put numbers, it was common that after the bandpass search, the U-board had to handle 1200 MKIDs, having at least 400 non-real MKIDs.

This miss-classification issue was tolerated since the U-board processing power can deal with it, and it is more important to not classify an actual MKID as a non-MKID. But when doubling the number of tones, the memory problem starts to arise, and the pipeline stops. So, the first step to implement a double-tone readout was to filter out the false MKID candidates.

The first method to filter out the non-MKID candidates is to look at the optimal power

[3] As these fake MKIDs do not respond to temperature variations, they will be discarded in the offline processing stage.

distribution of the single-tone readout. Figure 4.1 shows that several MKID candidates have the minimum tested power as the optimal. Several power-sweeps were made with different power levels, and the distribution always kept a similar distribution with a good portion of the candidates at the minimum power available.

As presented in Chapter 3, the power-sweep stage searches for the minimum power when the resonance starts to move to lower frequencies. A non-MKID that was misclassified is expected to not respond to the change of power, keeping the fake resonance in the same place. So, by construction the power-sweep algorithm will always assign the lower power levels to the non-MKIDs as the optimal power.

In consequence, the first new requirement is that the MKID candidates should not have as optimal power the lowest tested power available.

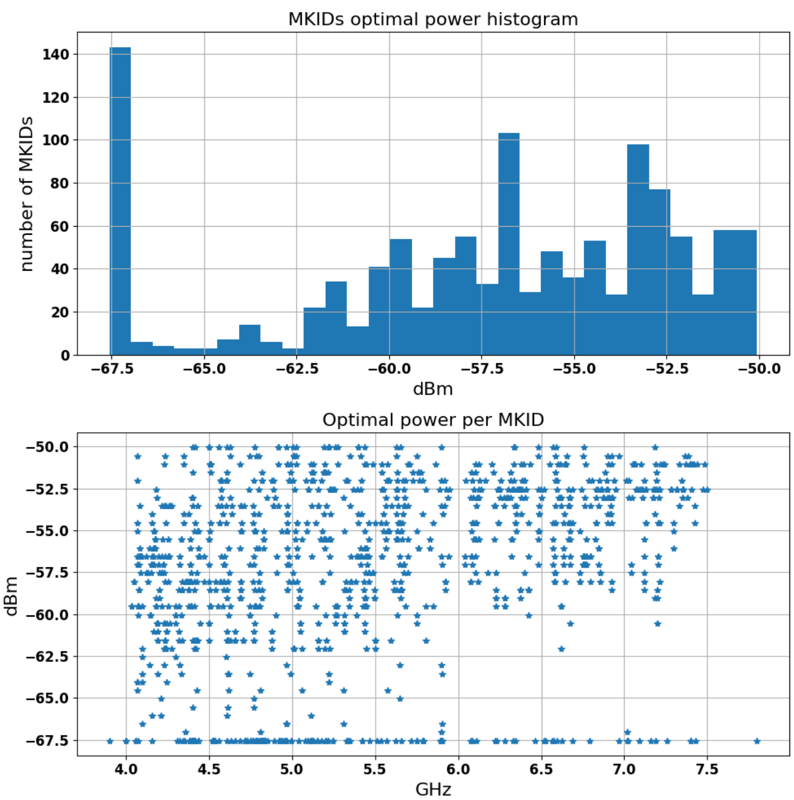

Figure 4.1: Optimal readout power using the powersweep method. The upper image is a histogram of the optimum powerlevel of all the MKIDs candidates. The lower image is the optimal power distribution of the MKIDs candidates across the bandwidth.

The second problem found in the MKID candidate set was that there are multiple candidates associated with one resonance. To avoid this behavior, the second imposition is that there cannot be another MKID candidate in a given frequency neighborhood. Therefore, for each MKID candidate, we draw a ball with a certain radius, and if two or more candidates have an overlap, then these two candidates belong to the same group associated with a single resonance. Finally, after having all the groups formed, we only kept one candidate per group. For this second imposition, we used a clustering algorithm called Density-Based Spatial Clustering of Applications with Noise (DBSCAN)[32].

DBSCAN creates fully connected maps between a dataset. The parameters that the user needs to set in this algorithm are the minimal amount of points to form a group *minPts* and the radius of the ball around each point ϵ.

A point p_0 is called *core point* when it has at least *minPts* at a distance ϵ. A point p_n is reachable if exists a sequence $p_{n-1}, p_{n-2} \dots p_1$ where point in the chain is at a distance ϵ from the previous point in the chain. This chain of reachable points forms a single cluster as figure 4.2. The points that are not reachable by any other point are called *outliers* or *noise points*. For the MKIDs application the *outliers* are the perfect candidates, where the MKIDs finding algorithm only detects one candidate per resonance. For the clusters formed we selected as representative the candidate that had the lowest optimal power in the set.

Figure 4.3 shows the cluster tags formed by a set of MKIDs, where the tag -1 are the noise points and the rest of the tags correspond to repeated tones that the power-sweep algorithm returns. For this example, the number of clusters created is 228 where the biggest cluster had 8 members.

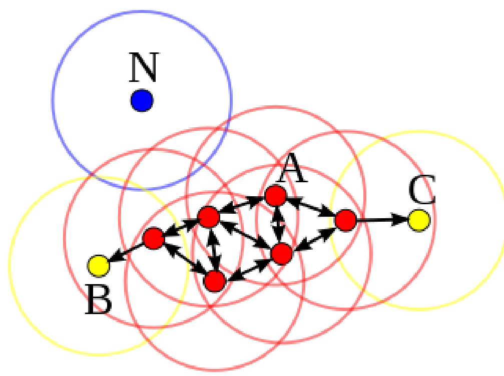

Figure 4.2: DBSCAN diagram. Image extracted from [32].

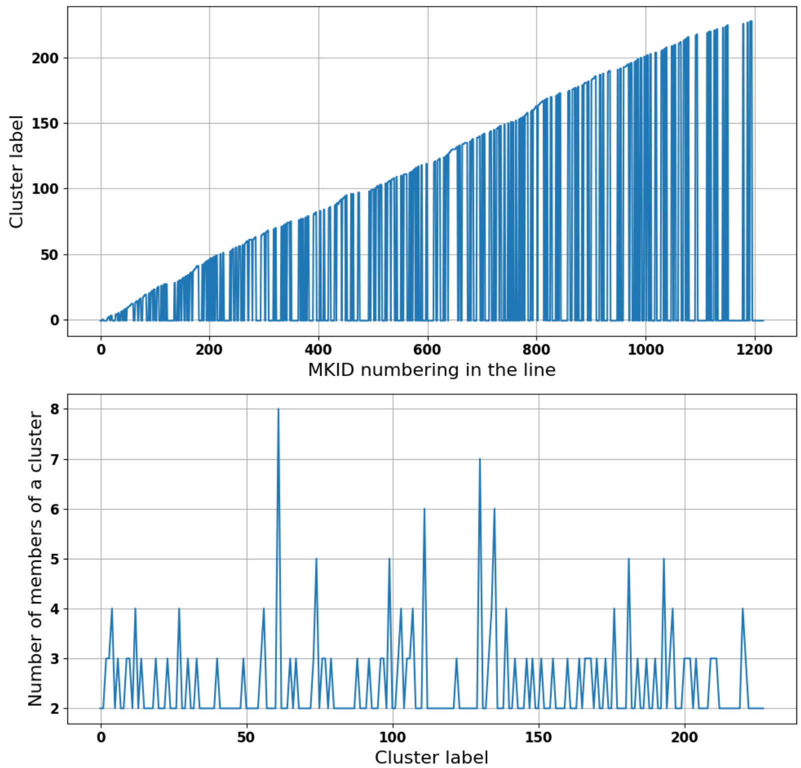

Figure 4.3: DBSCAN clustering over the single tone readout frequencies with a radius of $20kHz$. The upper figure shows the cluster belonging of each MKID candidate. Note that the clusters are labeled with growing numbers and the number -1 is reserved for the outlier group. The lower figure shows the amount of MKIDs candidates that are in a given cluster (excluding the outliers group).

The removal of the duplicated tones per resonance is an important step, not only due to memory restrictions but also for optimal readout power level determination. Since there were several tones at the same MKID, the outcome of the power-sweep routine is not valid since the additional tones affect the MKID response. For that reason, this clustering algorithm also becomes part of the frequency sweep step to keep the duplicated MKIDs as low as possible.

4.1.2. Double tone position

For the single-tone readout, the standard method is to place the tone near the MKID resonance because when the resonance shift occurs, the power difference will be more noticeable in that spot. But since we are using circle phase as the monitor parameter, we thought about the possibility of maximizing the available linear zone in the circle domain.

For an ideal MKID, the center of the linear zone in the circle domain and the resonance position are the same, but when measuring an actual MKID, there is a difference between them due to the asymmetry of the MKID itself. As an example, figure 4.4 shows a MKID that has a clear difference between the resonance frequency and the center of the linear zone, and in that specific case, when the detector receives the incoming radiation and the frequency shifts downward, it could end up being out of the linear zone.

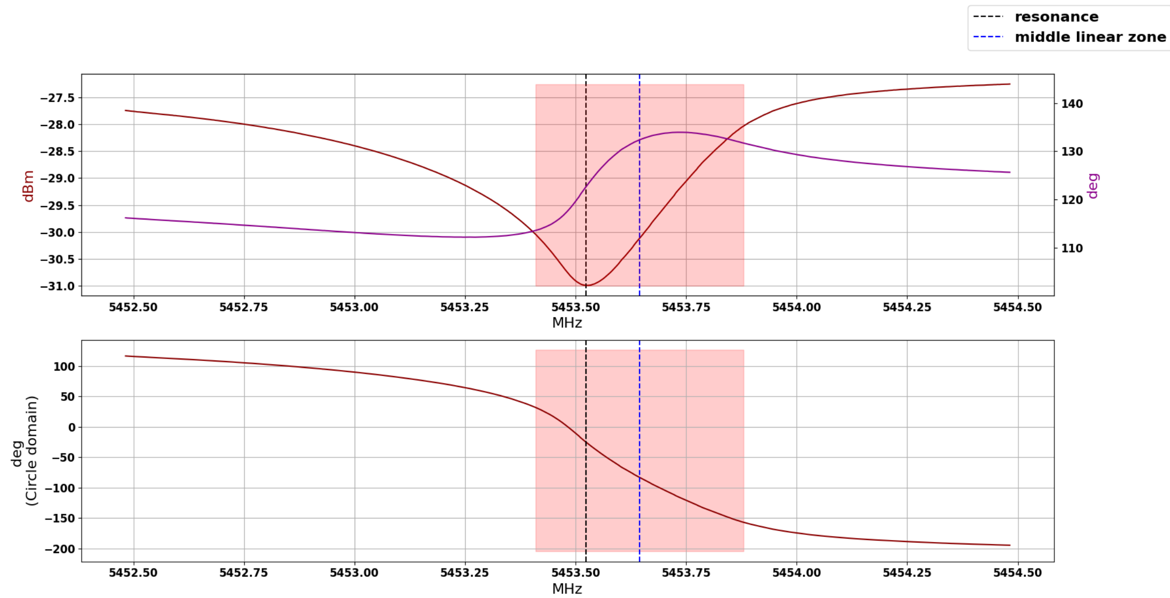

Figure 4.4: Example of a MKID where its resonant frequency does not match with the center of the linear zone.

With this in mind, we decided to test 3 configurations:

1. Single tone readout with the tone at the resonance.
2. Double tone readout with the tones equally separated from the resonance.
3. Double tone readout with the tones equally separated from the center of the linear zone.

For the double-tone positioned centered in the middle of the linear zone in the circle domain, we need an automatic way to determine the linear range of each MKID. The brute force search would be to take successive pairs of points in the frequency sweep circle data and make a linear fit, searching the range where the error between the fit and the actual curve is minimum. As there is no prior information on the linear zone size of the MKIDs, and since the actual measured linear parts of the MKIDs are not ideal, this brute force becomes impractical.

The determination of the linear zone was made using a decision tree regression algorithm. A decision tree is a data structure where, in every node the initial dataset is separated into smaller subsets trying to maximize or minimize a given metric (for example, the variance in the child sets). Therefore, when going deeper the subsets have to meet more separation criteria, partitioning the space into different categories.

Figure 4.5 depicts an example of the partition process of a decision tree, where for each node there is one partition on the subspace. These successive partitions lead to the complete classification of the input samples. When using a decision tree as a regressor, instead of returning a class for a given input, the tree returns a value that best fits the data. Both types of trees use a training set as input information for how to build the decision scheme. Figure 4.6 shows a decision tree in a regression problem where it can be seen that the output of the tree is a piece-wise function that depends on the depth of the tree.

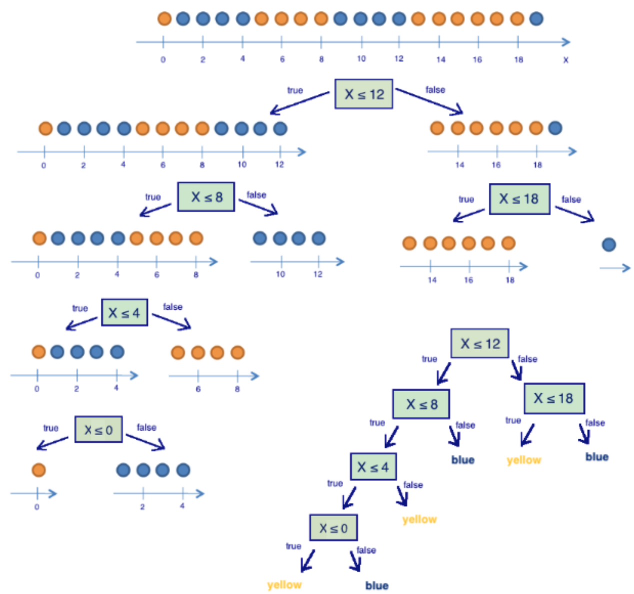

Figure 4.5: Decision tree example. In this example the tree separates the blue and orange points using a decision scheme. Image extracted from [33].

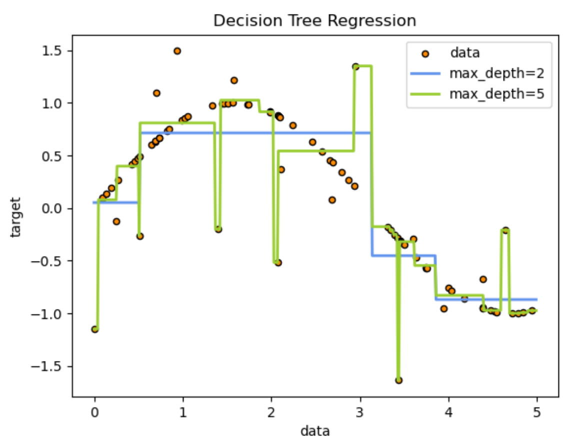

Figure 4.6: Decision tree as a regressor. Image extracted from [34].

To find the linear zone on the circle, first we pass the signal through a low-pass filter to avoid noise spikes, then we calculate the derivative over the filtered data and finally feed the result into the decision tree to train it. The trained tree returns a single value for a region that shares roughly the same slope. This approach is only valid if we know beforehand how many piecewise linear functions the signal can decompose, but luckily, when identifying the number of resonances that are in the data, we obtain a hint of the test number. We found that an acceptable number is five linear functions per resonance. Figure 4.7 shows the output of the algorithm and the intermediate information of the derivative of the phase and the regression output.

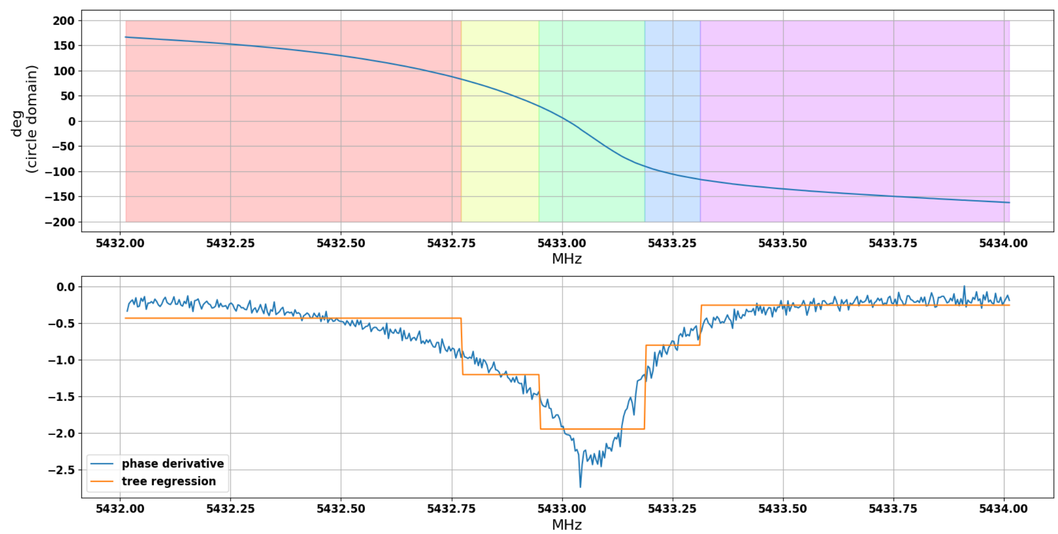

Figure 4.7: Example of the linear zone detector method. The upper figure shows the circle phase data obtained after a frequency sweep. The colorized regions represent the zones predicted by the regression tree. The lower image shows the actual derivative of the phase and the regression made by the decision tree.

The algorithm for the linear zone search allows us to characterize the distribution of the linear zone in all the MKIDs in the line. Figure 4.8 shows a histogram of the linear zone widths per MKID, where we can see that most of the MKIDs have around 100 kHz of linear zone available.

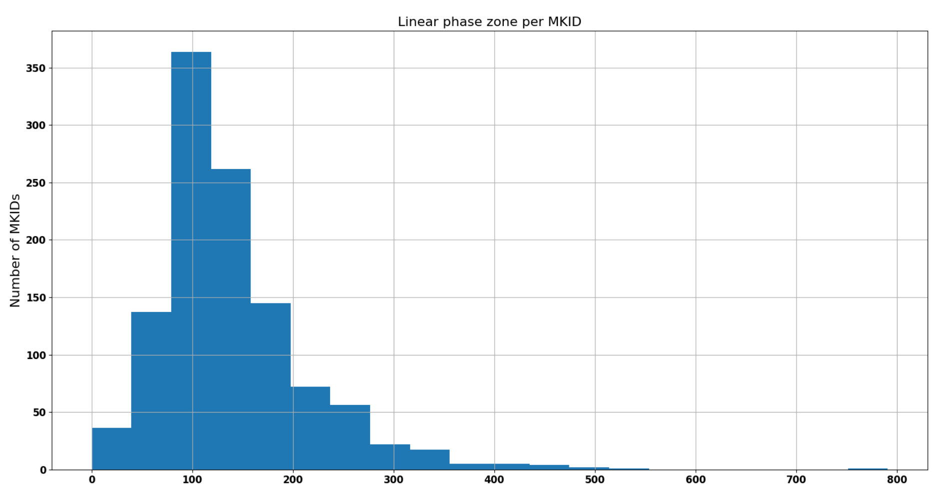

Figure 4.8: Linear zone width in the circle domain for the line 19 of the A-MKID receiver.

4.1.3. Characterization of the double MKID readout

When the optimal power level of the MKIDs is computed, the system can switch to a double-tone readout mode, where you can select the position of the tones to be centered around the resonance with a defined gap (we use 20 kHz) or to be centered around the middle of the linear zone. When using the linear zone as the positioning method, you should be aware that as each MKID has its own linear zone width, the positioning will vary between the MKIDs. To maintain the power level of the signal, we maintain the tone levels but add 3 dB of attenuation using the digital controllable attenuator.

After placing the double tones with the optimal power levels, we need to re-characterize the MKIDs because even if we get the single-tone circle parameters, when placing two tones at the MKID the presence of the second tone will affect the measurement of the first one. As an example, figure 4.9 shows the effect of measuring with two tones instead of one. The figure 4.9 was made using the double-tone at ± 20 kHz of the single-tone resonance. The first thing to be noted is that for the double tone readings the depth of the MKID is lower than the single tone reading. Also, between the two tones used in the double tone reading, there is a disagreement in the depth of the resonance. These effects occur because the frequency sweep is made by changing the LO frequency, moving it from lower to higher frequencies. Then, when the tone positioned at $+20$ kHz passes through the resonant frequency, the effect of the tone at -20 kHz is not being noted by the MKID, so the total amount of readout power is less than the optimal one, causing the MKID response to be smaller than it should be. On the other hand, when the tone positioned at -20 kHz passes through the resonance, the MKID is still able to sense the power from the tone at $+20$ kHz, obtaining a deeper reading. In this case, the resonant frequency remains more or less equal to the single tone readout, but there are cases where the resonant frequency also shifts to a lower frequency since the total amount of power is less than the optimal one.

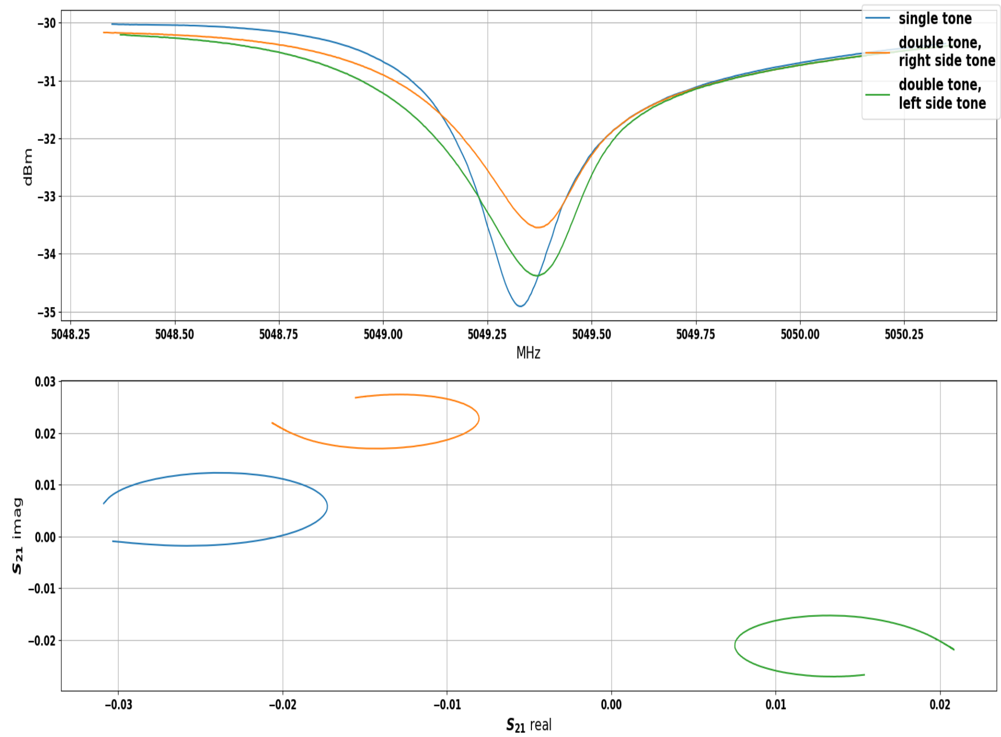

Figure 4.9: Example of the difference between the double tone and single tone readings. The curves are inherently different and then each one needs its own parameters for the phase reading.

Although this effect in the reading is disappointing, since we would ideally like to have the exact same circle parameters than the single-tone case, when the resonance shift occurs the overall effect will be the same as observed on the frequency sweep data. This means that one of the tones will measure the resonance with lower power than the other one.

If we disregard for a moment the change in the quality factor of the resonator, we can relate the frequency sweeping method and the change in the resonance when the tones are fixed in a given frequency with the mathematical idea of passive transformations (where the coordinate system is fixed and the points move) and active transformations (where the points are fixed and it is the coordinate system that moves).

In the case when the readout system is moving the tones, it is equivalent to being in a reference frame that is moving, and the effect would be the same as keeping the tones fixed and having a change in the resonant frequency.

Figures 4.10, 4.11, 4.12, 4.13 depict the different curves generated when implementing the double-tone readings and compare them with the single tone curves. In these figures, the two methods presented before were used, one where the tones are placed at $\pm 20kHz$ from the single-tone version and the second one where the tones are placed considering the width of the linear zone at the phase in the circle domain. Additionally, figure 4.14 shows the intermediate steps used to compute the width of the linear zone in the circle domain and how it is mapped to the other visualizations of the MKID.

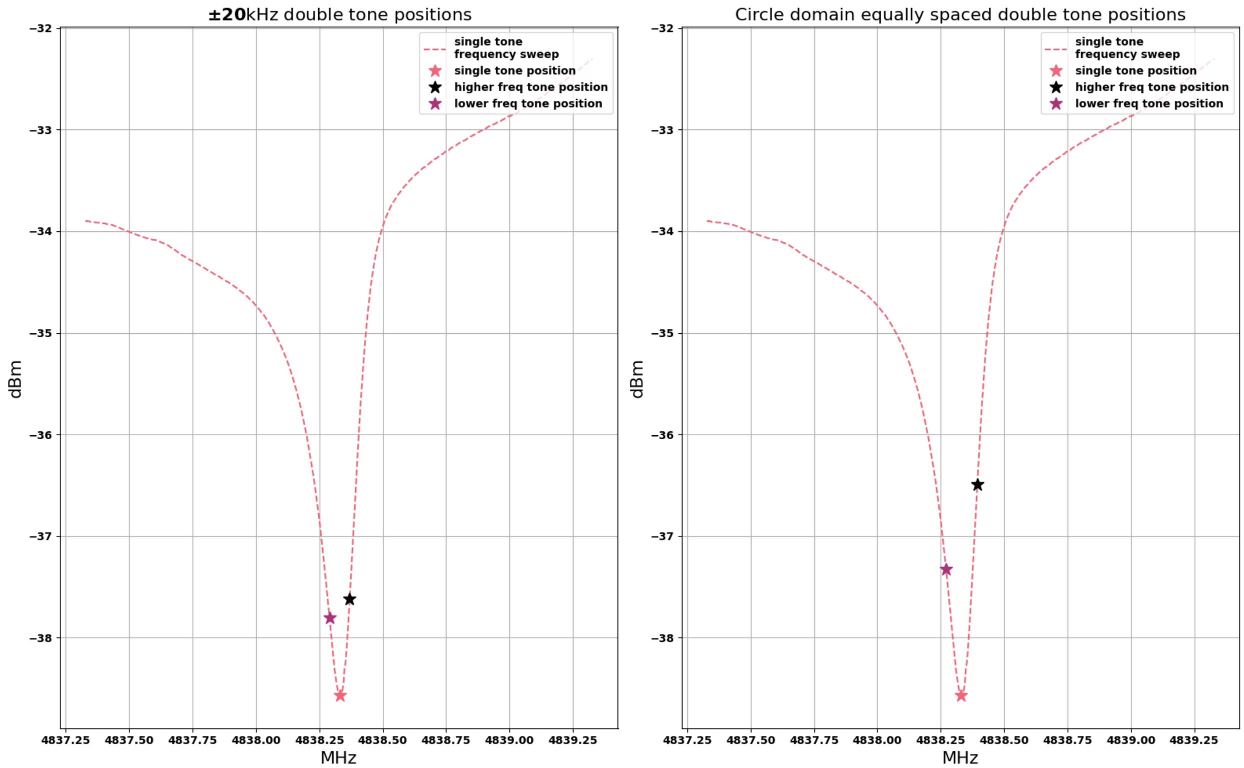

Figure 4.10: Double tone positioning for the two schemes.

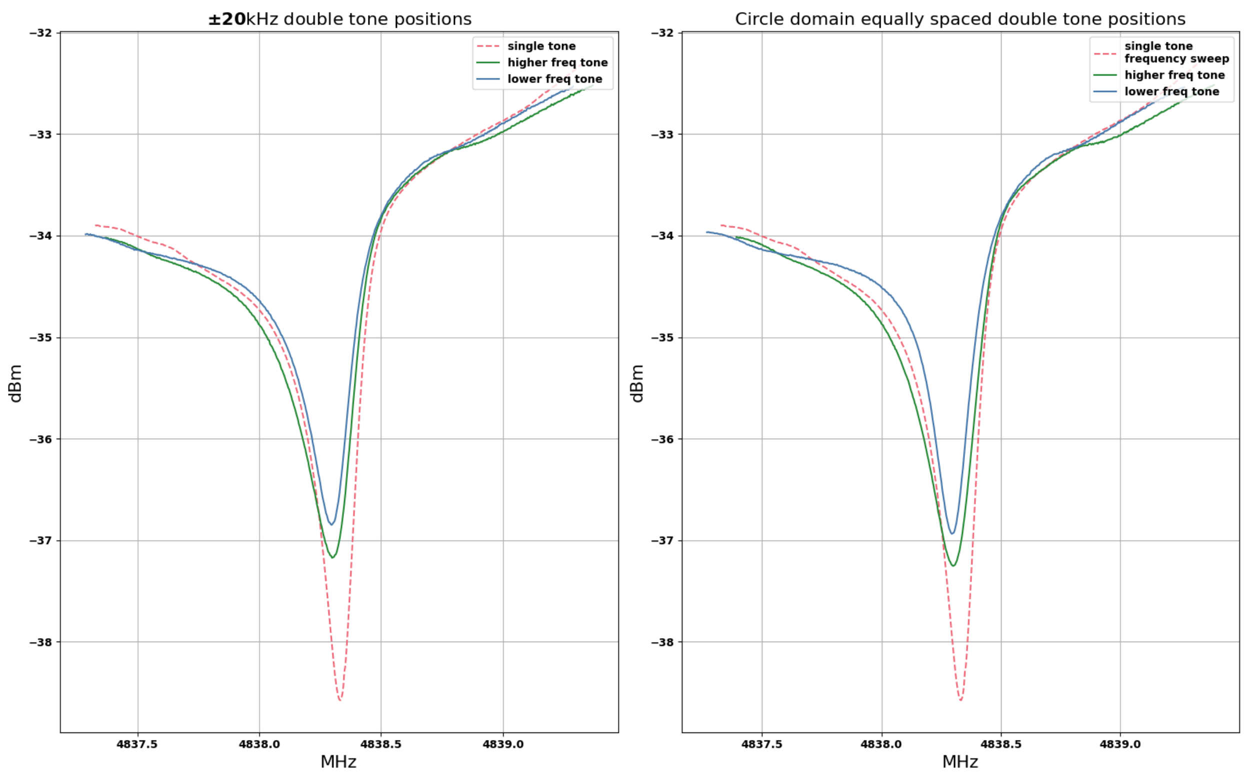

Figure 4.11: Double tone frequency sweep for the two schemes.

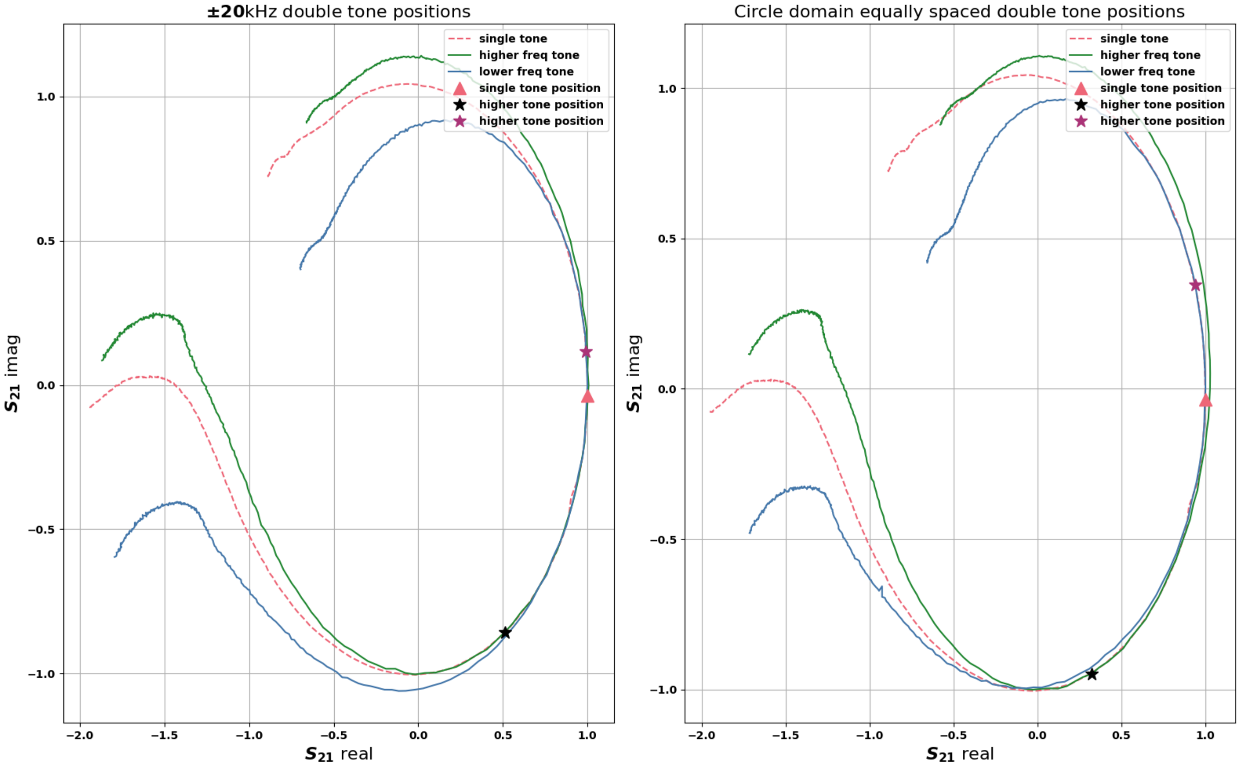

Figure 4.12: Double tone circles for the two schemes.

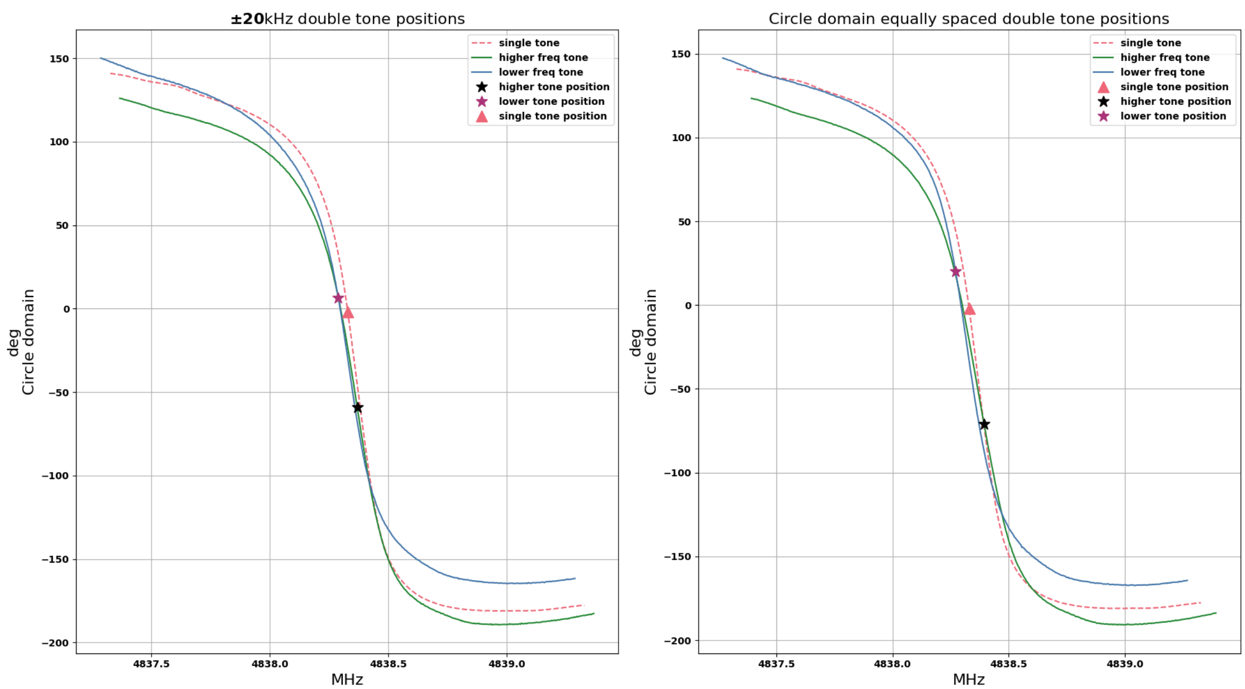

Figure 4.13: Double tone phase curve at the circle for the two schemes.

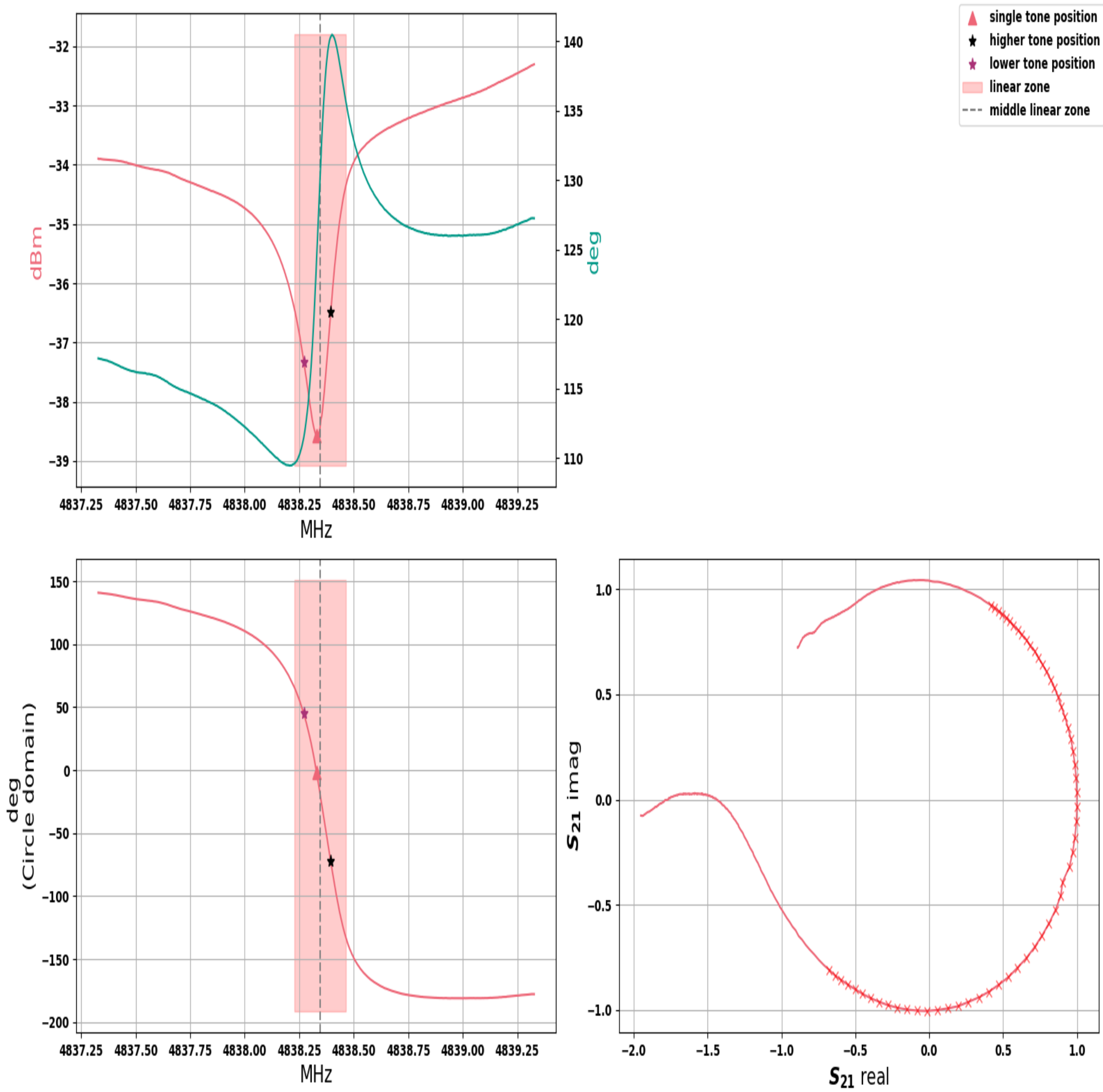

Figure 4.14: Double tone intermediate steps for the equally spaced toned in the circle domain.

4.2. Wire scan test

To test the implementations of the double-tone readout, we need a way to compute the sensitivity of each configuration and compare it with the single-tone sensitivity. For a receiver, the standard method consists of placing two known temperature sources in the optical path of the receiver and reading the corresponding response of the detector. Since the resonance shift of the MKIDs is linear with the temperature, if we know the source temperatures beforehand, we can calibrate the MKIDs responses, obtaining a phase-temperature mapping.

At the Max-Planck Institute, a novel method to calibrate the MKIDs response was developed, where four stepper motors move two cables in front of the optical path in the X and

Y directions. When the cable passes in front of a given detector beam, the MKID detector will respond to the change in temperature by abruptly changing its phase value in the circle domain. The idea is to calibrate the MKID response knowing the background temperature (when the cable is not crossing the beam) and the room temperature weighted with the effective area of the cable at the detector frequency when it crosses the beam.

When having the system installed in the APEX telescope, the background temperature will be the sky temperature (measured by a radiometer). For the laboratory setup, we placed a bucket filled with liquid nitrogen with a flat background temperature of 77 K. Figure 4.15 shows the model of the wire scan used to calibrate the MKIDs.

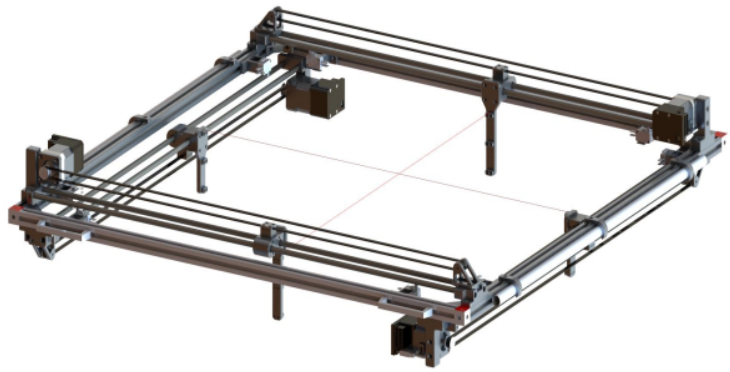

Figure 4.15: Model of the wire-scan system. The wire-scan is mounted in the optical path of the MKID receiver to generate a temperature change to calibrate the MKIDs.

To calculate the NET of the MKID array, we transform the phase data into temperature, then calculate a periodogram over the data and normalize it by the spectral channel width having a signal with the units K^2/Hz. Over the periodogram, we calculate the standard deviation in all the channels, obtaining the NET with units of $K/\sqrt{Hz}$. In this setup, one can think about the NET as the variation of the sensors when measuring a stable temperature, which at the end is the error bar of the instrument when being used.

Besides the NET estimation, the wire-scan can be used to find the location of each MKID beam in the focal plane. To do that, the wire-scan is constantly streaming the cable positions with the corresponding timestamp. On the backend side, the computed phases also contain a timestamp, so we can relate the response of the phases to a given cable position, obtaining the pixel position.

4.3. Results

To test the dual-tone readout and compare it with the single-tone readout, we placed a bucket filled with liquid nitrogen at the top of the wire-scan and measured the NET for the three modes:

- Single tone readout.
- Dual tone readout with $\pm 20kHz$ from the resonance.
- Dual tone readout equally spaced in the circle domain.

The first step in the data processing consists of correcting the baseline by fitting a polynomial of order 1, just to discount the slope that the readout could have. To find the cable response in the data, we search for zones that have over three standard deviations. Since the movement of the wire-scan cables is a round trip, the cables cross the beam of each pixel four times (two on the X axis and two more on the Y axis).

Figure 4.16 shows the response of a single MKID to the wire-scan system and how we found the wire in the data. In this figure, it is noticeable that the amplitude of the phase response is not equal for all the cable crossings, but what should be an invariant is not the height of the response but the overall integrated area of the peak.

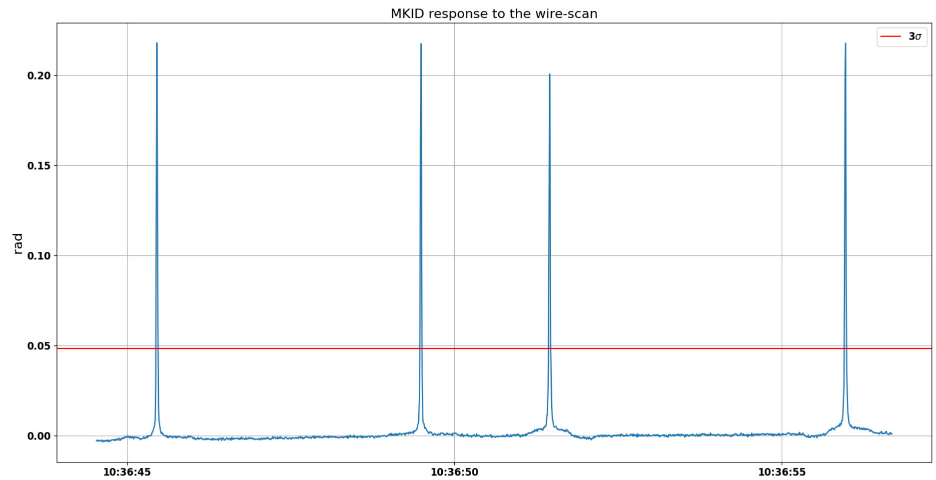

Figure 4.16: AMKID response to the wire-scan.

With the cable cross identified in the phase data, we can read the timestamp position that the wire-scan streams while moving, and using an interpolation, we are able to find the position of the MKIDs in the array. As the wire-scan passes two times for each detector in the X and Y axes, we can compute the errors associated with the position determination in a preliminary way[4]. Figure 4.17 shows the calculated positions of the MKIDs detector in the line 21, with the error bars in the positions and a color map of the integrated area of the peaks in the data.

[4] when observing in the telescope, the actual pixels positions would be found observing a celestial source in a continuous mapping mode.

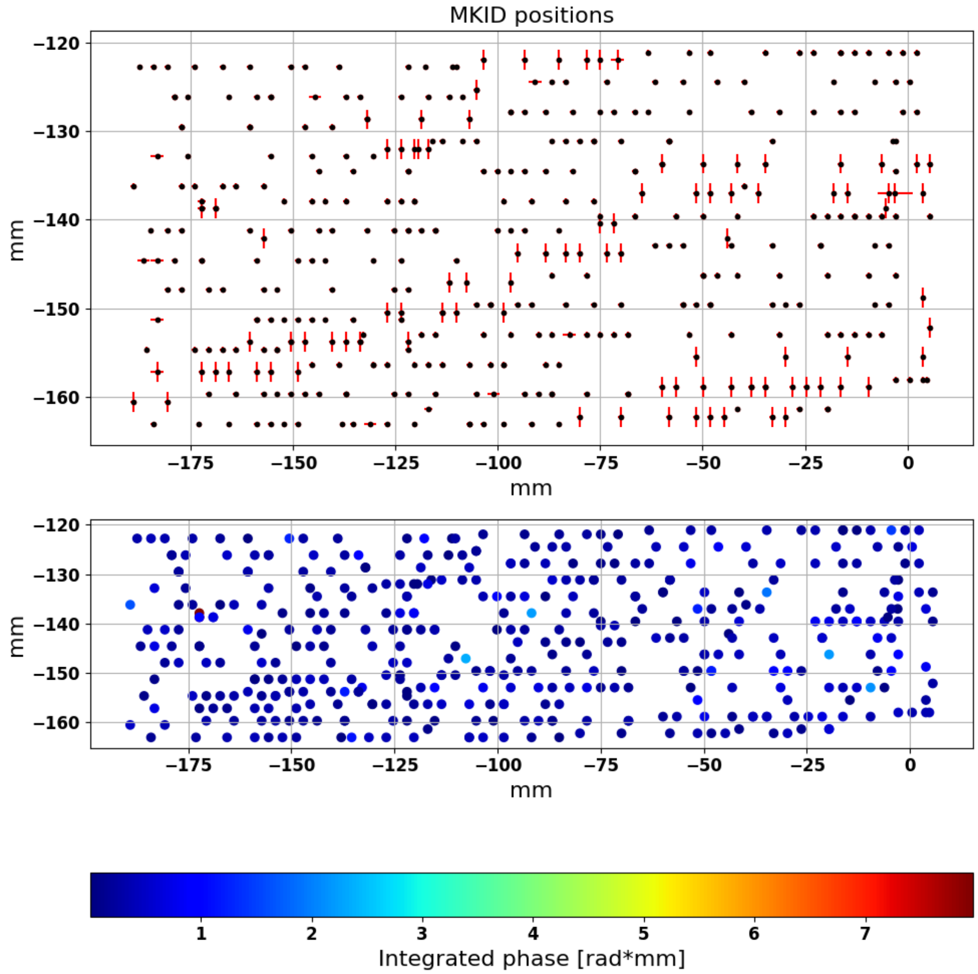

Figure 4.17: Positions of the detectors at the line 21 using the wire-scan calibrator. The upper image shows positions of each detector with its error bars and the lower image shows the integrated phase for each MKID.

To make the phase-temperature conversion, we calculate the integrated phase in the peak and normalize it by the effective wire width at the detector frequency. This integrated phase is used to obtain the calibration factor to convert the phase data into temperature, as equation 4.1 shows.

$$calibration\ factor = \frac{T_{wire} - T_{background}}{Integrated\ phase} \left[\frac{K}{rad}\right] \tag{4.1}$$

To calculate the NET, after the wire-scan measurement, we let the system read the nitrogen bucket in order to measure the variation of the system, and we use the calibration factor obtained to transform the phase data into temperature. With the temperature we can compute the periodogram and calculate the variation over the data. To avoid considering the flicker noise, we just consider the channels over 5 Hz. Figure 4.18 shows the spectrum of a single MKID when reading the nitrogen bucket; in red is marked the 5 Hz channel. It is also important to note the presence of the 50 Hz component that comes from the electrical power network.

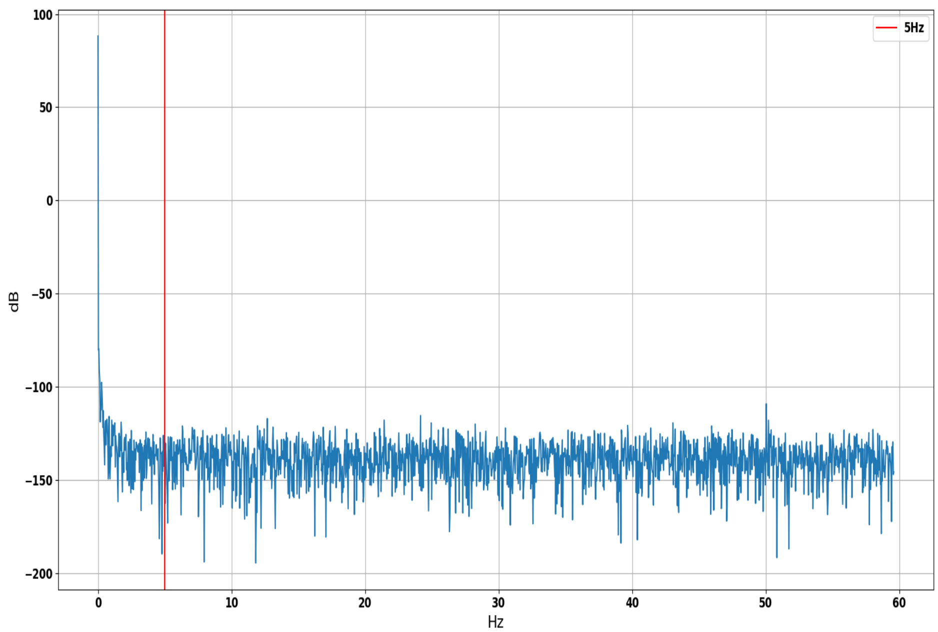

Figure 4.18: MKID background spectrum when placing the nitrogen bucket in the optical path of the receiver.

The NET for the single-tone readout is shown in figure 4.19. For the case of the double-tone readout, we calculate the average temperature response before computing the periodogram (so we are doubling the integration time). The results for the two double-tone schemes are shown in figures 4.20 and 4.21. To compare the results obtained by the double-tone modes, we also add the NET computed by each tone on its own (in a single-mode format) and just keep the minimum of the pair that is reading a certain MKID. The histograms of these computations can be seen in the figures.

The NET results are summarized in table 4.1, where the single mode NET is the method described previously, analyzing each one of the tone pairs on its own and keeping the lower NET of both tones. It is worth to mention that the MKIDs considered in the histogram are the ones with a NET higher than $10mK\sqrt{s}$, causing that the number of MKIDs differ in each configuration.

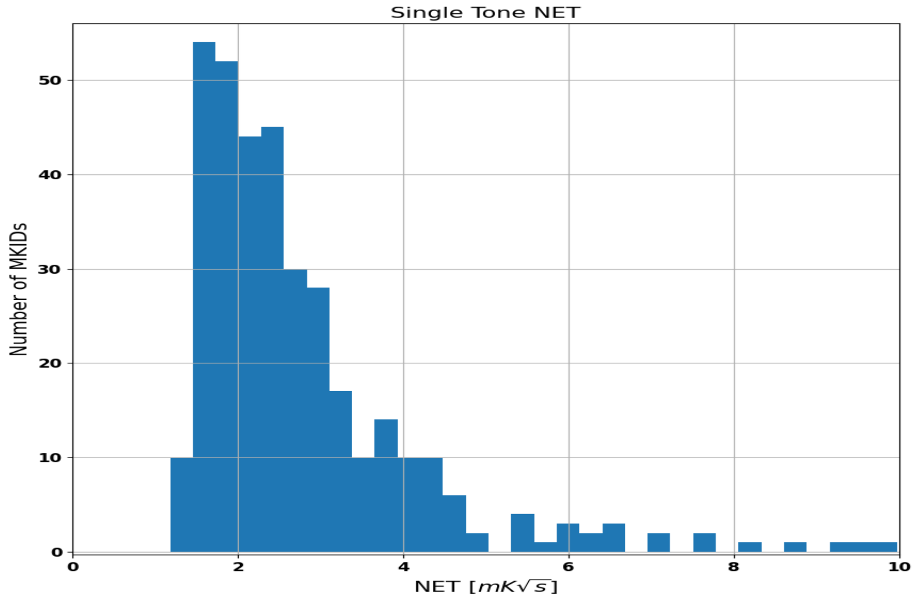

Figure 4.19: Single tone NET histogram.

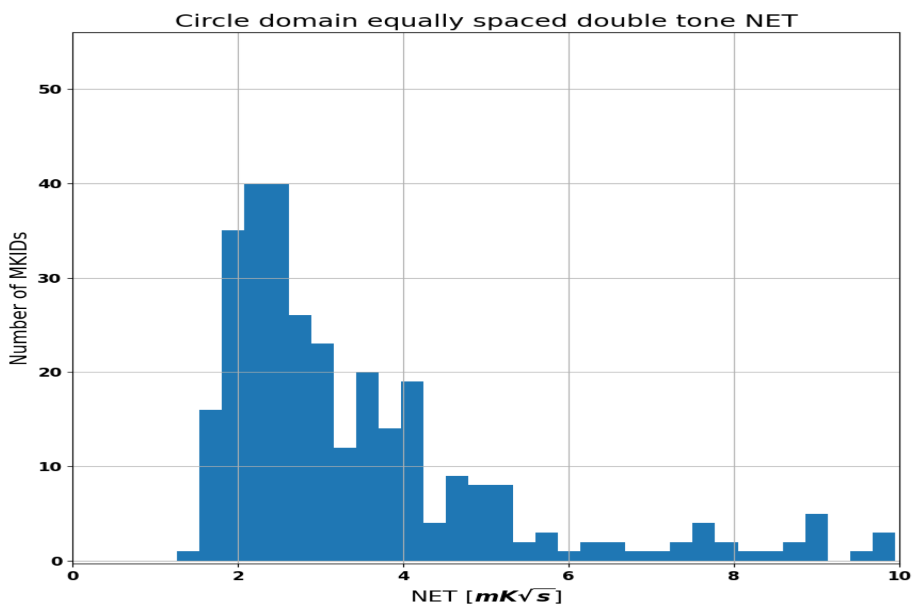

Figure 4.20: Equally spaced in circle domain double tone readout NET histogram.

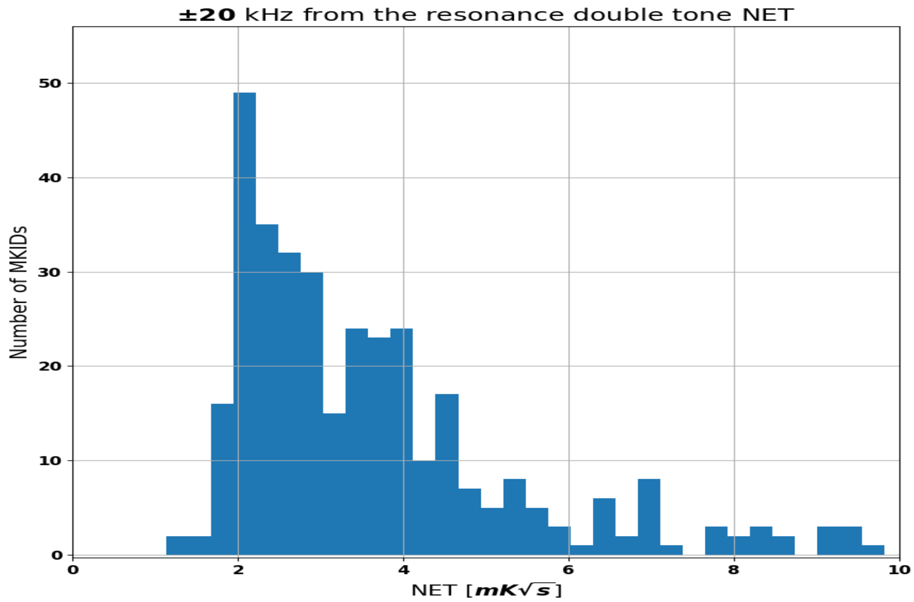

Figure 4.21: ±20 kHz from the resonance double tone readout NET histogram.

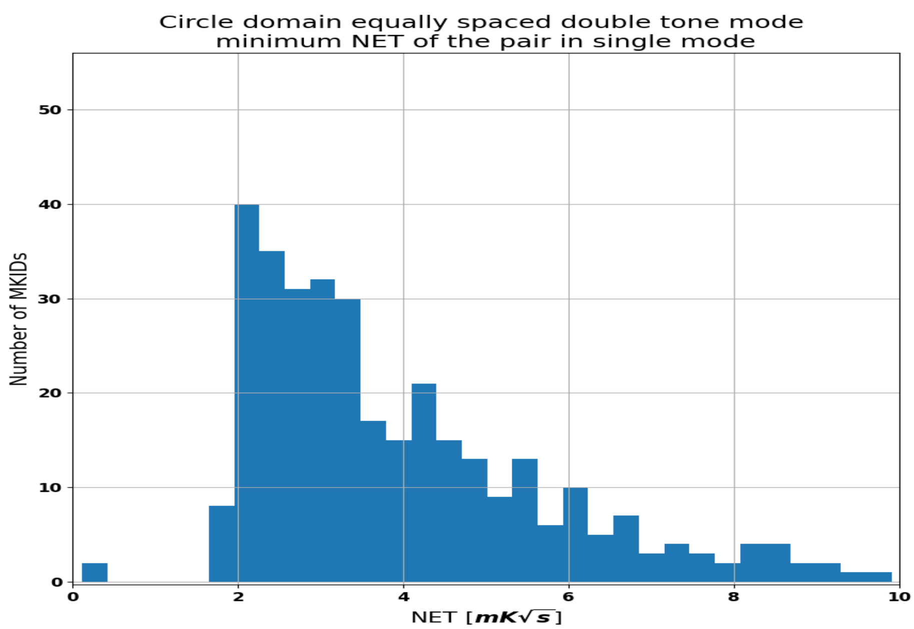

Figure 4.22: Equally spaced in circle domain double tone readout, with the NET computed using each tone by its own and keeping the minimum NET of the tone pair.

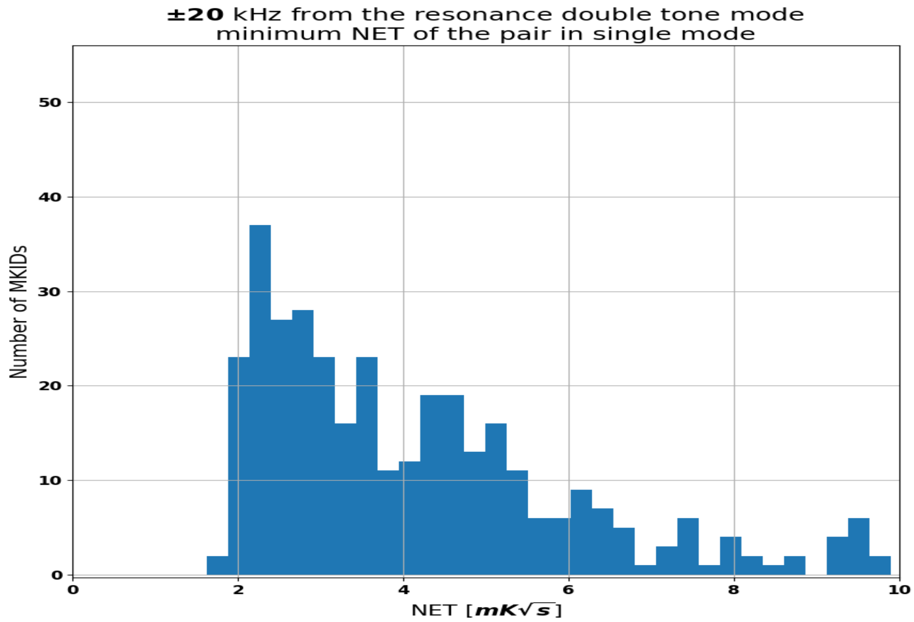

Figure 4.23: $\pm 20kHz$ from the resonance double tone readout, with the NET computed using each tone by its own and keeping the minimum NET of the tone pair.

Table 4.1: NET statistics

	KID number	average $mK\sqrt{s}$	median $mK\sqrt{s}$
Single Tone	439	2.77	2.35
Double Tone ±20 kHz from resonance	392	3.62	3.15
Double Tone ±20 kHz from resonance single mode NET	392	4.12	3.65
Double Tone spaced in circle domain	376	3.44	2.84
Double Tone spaced in circle domain single mode NET	376	3.911	3.39

The results obtained show that the performance of the double-tone modes is worse than the single-tone mode. When using two tones per resonance readout but computing the NET using each tone on its own, we obtain worse results than when combining them to compute the NET. This indicates that the averaging of both tones is indeed increasing the sensitivity and can be understood as a gain via a longer integration time, but the values are still worse than the ones obtained in the single-tone mode.

Chapter 5

Conclusions

5.1. Conclusions

In this document, the implementation of a dual-tone readout for the A-MKID camera has been described. To put the work in context, it was necessary to present the MKID technology, making a brief introduction to the superconductor theory.

For the completeness of the document, it was also necessary to describe the mathematics behind the circle phase readout, which is based on resonator theory and consists of modeling the MKID response as an ideal resonator and finding the parameters that best describe the data. With the resonator parameters, the readout can use a single tone to read the state of the MKID.

As this type of readout relies on a non-trivial way to read the system status, so it is mandatory to use custom solutions. For this reason, the Max-Planck-Institut für Radioastronomie developed a novel FPGA-GPU system for the next-generation readout system named U-board, which was used in this thesis.

For the dual-tone readout, two schemes were developed. The first one just places the tones at $\pm$ 20 kHz from the resonance, and the second one places the tones, trying to maximize the usage of the linear zone of the phase in the circle domain of the MKID. To test the performance of the system, the noise equivalent temperature was used as a metric. To compute the NET of each readout configuration, a novel MKID calibrator setup based on a moving wire in the optical path was used. This calibrator setup, named wire-scan, besides giving the sensitivity of the system, can be used as a way to obtain the pixel positions in the optical path.

The NET results indicate that the use of a dual-tone readout deteriorates the camera's sensitivity when comparing its performance with the one obtained by a single-tone readout.

In the double-tone setup, the data shows that the sensitivity increases when using the information of both tones compared with the sensitivity of using only the information of each tone on its own. Anyway, the noise inserted by doubling the number of tones compared with the sensitivity of the single-tone readout makes the use of the double-tone readout inconvenient.

The deterioration of the NET when using double-tone readout can be understood in a rough manner considering that the actual noise introduced by the digital system is given by equation 5.1 [35]. This equation tells that the noise of the digitizers will increase as the number of tones increases. Figure 5.1 shows the theoretical noise of the system as a function of the number of injected tones. On the other hand, the radiometer equation shown in expression 5.3 [36] tells the ideal SNR of a given source when knowing the source temperature T_{source}, the system temperature T_{sys}, the integration time τ and the instrument bandwidth BW.

The gain by increasing the integration time when doubling the tones is in the best case $\sqrt{2}$, but in the other hand the SNR reduction due the injection of the tones is around 3 dB in the ideal case. This is discounting the power dependence of the MKIDs, which generates shallow resonances when using the double-tone implementation, also impacting the readout sensitivity.

$$SNR_{ADC} = (6.02 * ENOB + 1.7) - 10 \cdot log_{10}(BW) \tag{5.1}$$

$$\text{ADC-DAC noise} = 10 \cdot log_{10}(n_{tones}) + \text{Crest factor} - SNR_{ADC}\ [dBc/Hz] \tag{5.2}$$

$$SNR = \frac{T_{source}}{T_{sys}}\sqrt{\tau \cdot BW} \tag{5.3}$$

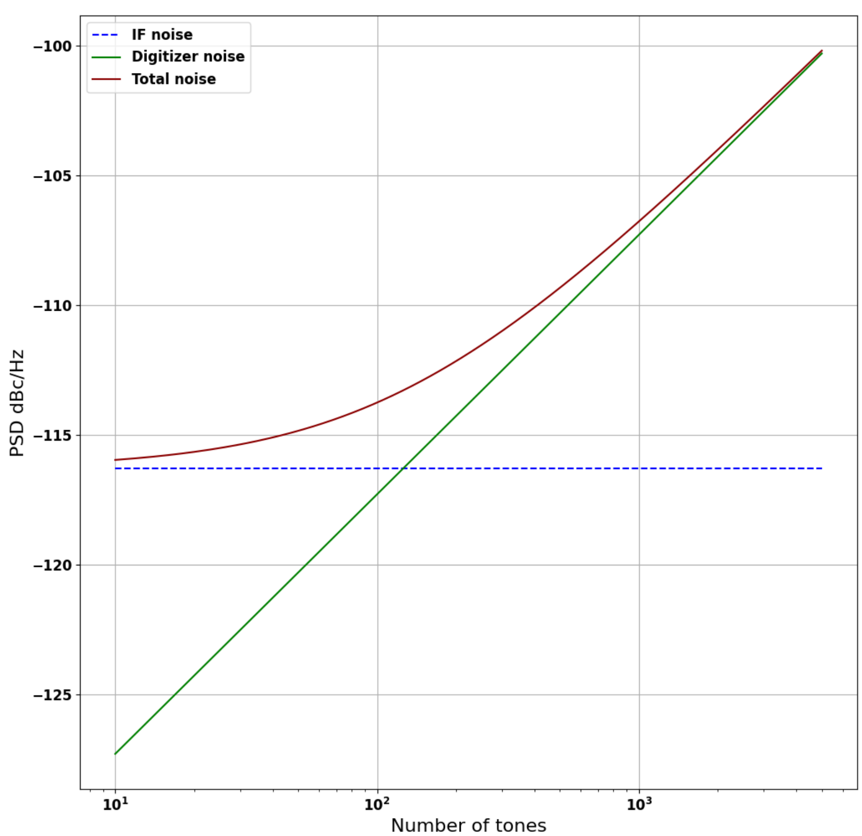

Figure 5.1: Theoretical system noise as function of the number of tones. This plot considers also the noise added by the IF amplifiers and attenuators before the digitizers.

5.2. Future Work

One of the main reasons to test the dual-tone readout was to be able to predict the positions of the resonances to adjust the tones and follow the resonance.

One idea that moves forward in that direction is based on the CONCERTO instrument resonance tracking algorithm [37]. This method is based on the geometry of the complex S_{21} plane, where by definition the closest point to the origin is mapped to the point where the resonance is. Therefore, measuring three points in the IQ circle can roughly predict the frequency shift of the resonance, as figure 5.2 shows. To get the three IQ points, the people of CONCERTO use a modulation in the LO shown in figure 5.3. This rough estimation is made by all the MKIDs in the line; if the majority of the MKIDs are shifted (this situation could be, for example, a change in the water vapor), then a partial way to solve it is to make a change in the LO compensating for the resonance shift. The benefit of this method is that it does not need to re-characterize the MKIDs, but it is not valid for large resonance shifts where the IQ circle parameters change and a new characterization is needed.

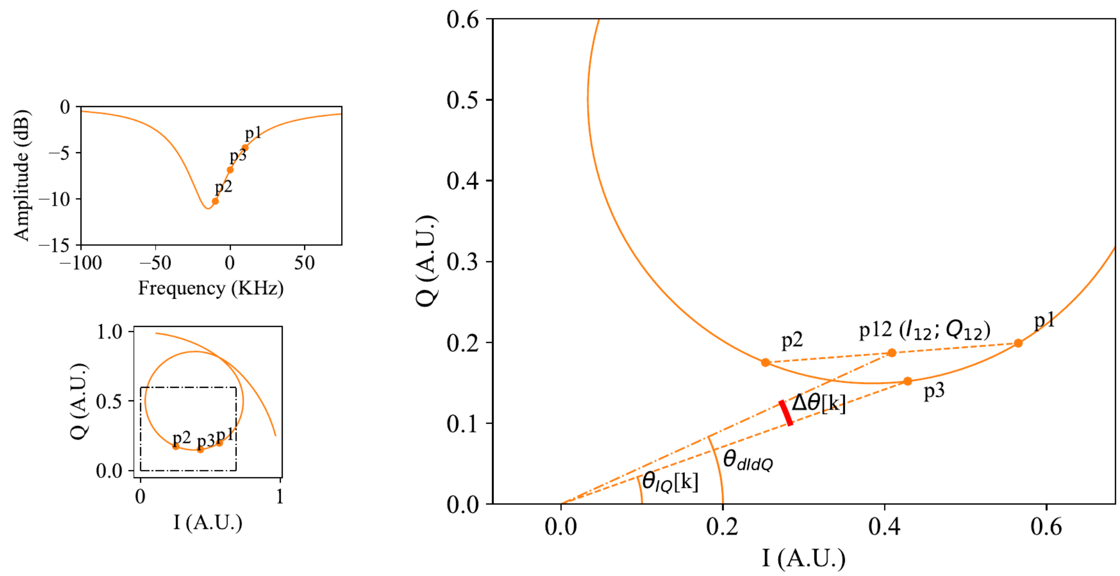

Figure 5.2: CONCERTO IQ data and a representation of the geometry used to predict the resonance shift. Image extracted from [37].

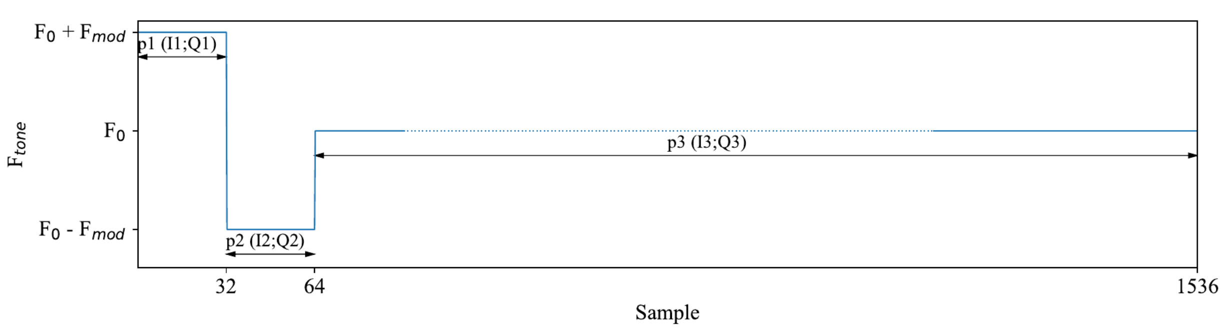

Figure 5.3: CONCERTO LO modulation. Image extracted from [37].

Since the U-board has enough computational power and the resolution of the IQ circles is outstanding, one plan is to predict the location of the resonance using the phase information of the circle domain. This is done by making a frequency sweep to obtain the phase curve in the circle domain and saving the curve as a MKID parameter. This phase curve can be used to predict the position of the resonance since you can invert the relation and for a given measured phase, calculate the corresponding frequency position. This is easily made by making just an interpolation of the measured curve.

To test the concept, we placed a polarizer at the cryostat window. The polarizer can be rotated using a DC motor, as figure 5.4 shows. Since the high and low frequency arrays are separated by an internal polarizer, when placing a new polarizer at the window, we can control the temperature loads that the MKIDs see. Therefore, when the polarizer angle matches the internal one, the MKIDs will see the ambient temperature, and when the polarizer is orthogonal to the internal one, the beams of the MKIDs will be reflected and will see a sum of the external temperature and the internal temperature of the cryostat. So, the overall effect is that when rotating the polarizer at different angles, we obtain different temperature loads in the MKIDs.

As we have control of the position with the DC supply, we can stop it at a certain angle, and for each temperature load, make a frequency sweep and compare the predicted position by the circle phase with the actual frequency sweep position. Figure 5.5 shows the curves measured for different angles at the polarizer. Figure 5.6 shows the discrepancies between the peak search using the frequency sweep data and the position predicted by the phase curve. The curves at 1) show the effect of the optical aberration when placing an object at the cryostat window (the instrument optics were designed to be used with the APEX primary and secondary). This optical aberration produces that not all the detector beams are terminated at the polarizer, generating a spread in the temperature distribution that the MKIDs sense. The curves at 2) and 3) show the actual error between the predicted resonance position and the ones predicted via a frequency sweep measurement. It is important to note that the percentage error is relative constant.

Figure 5.7 shows the error statistics for this setup. Here we can see that the error is cyclical, which makes sense since at certain angles the polarizer grid should let pass the same polarization as before. This curve tells us that for the first 4 temperature loads, the error is manageable, but past that point, the error starts to increase, and it is not acceptable any more. This occurs since the phase is getting out of the linear zone of the circle domain. As a future project, the idea is to be able to control the angle of the polarizer using a stepper motor and calibrate the temperature loads using the wire-scan method. For that, the Max-Planck Institute built a calibration unit that will be placed at the entrance of the cryostat. Besides these calibration techniques, the rotating grid can also be used for polarimetry observations.

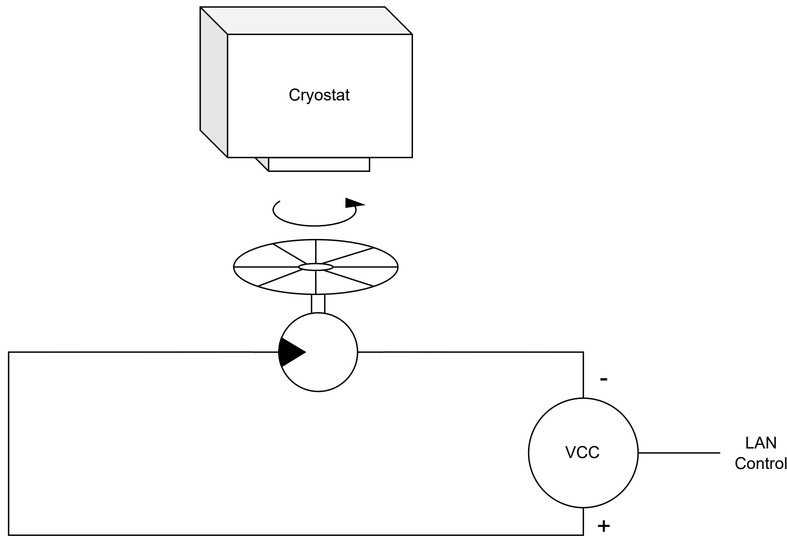

Figure 5.4: Polarizer test diagram.

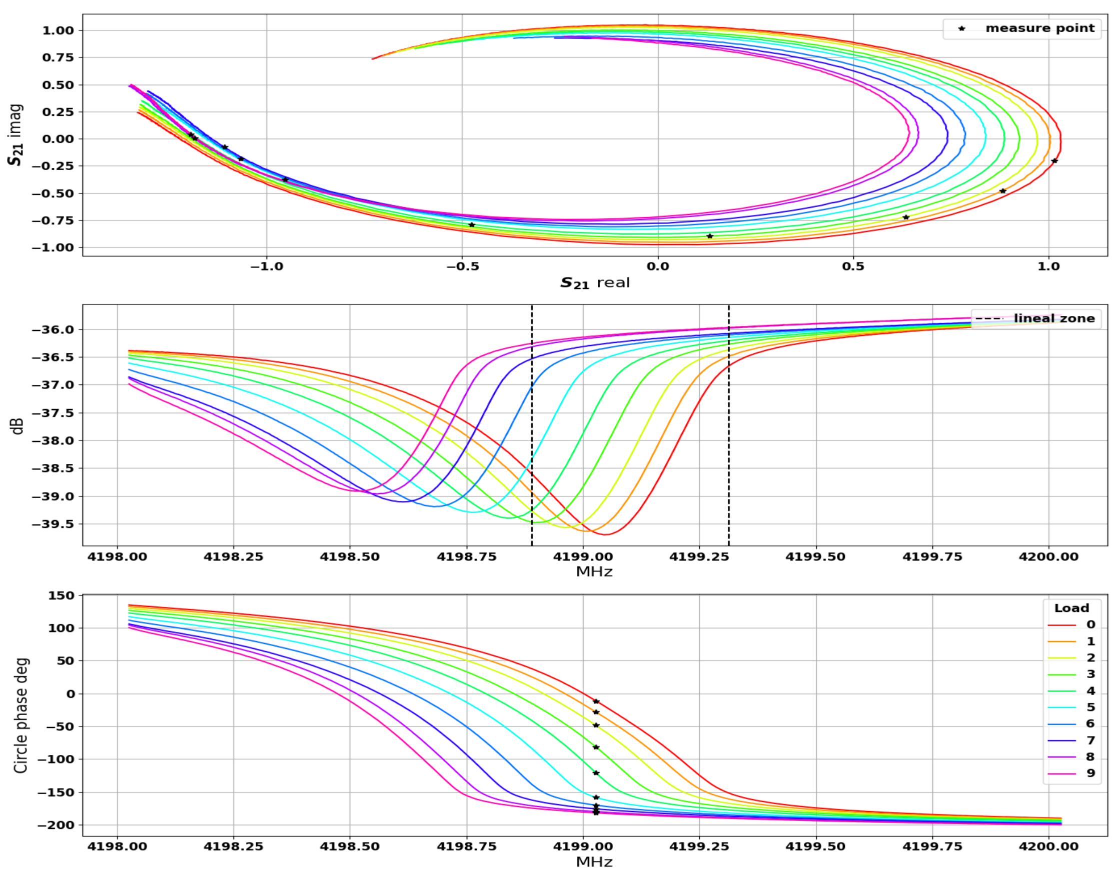

Figure 5.5: Measures obtained by changing the phase at the polarizer in front of the cryostat window.

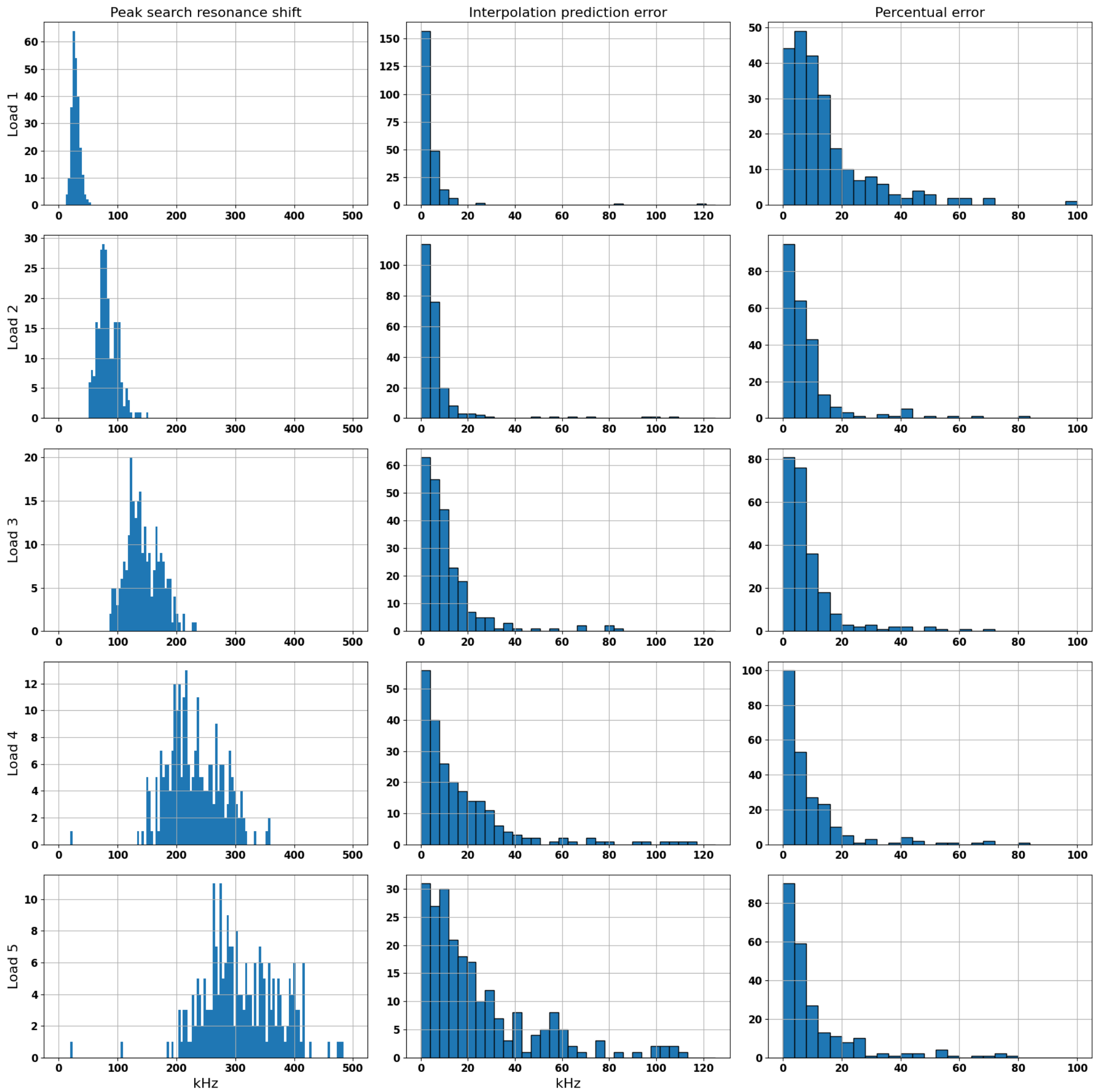

Figure 5.6: Polarizer predictions. 1) shows the shifts calculated via the frequency-sweeps. This image shows that the response at the polarizer angle is not equal for every MKID, this is due the optics aberration at the entrance of the cryostat window. 2) Shows the overall error between the predicted position of the resonance and the one measured using the frequency sweep data. 3) Shows the relative error when comparing with the resonance shift

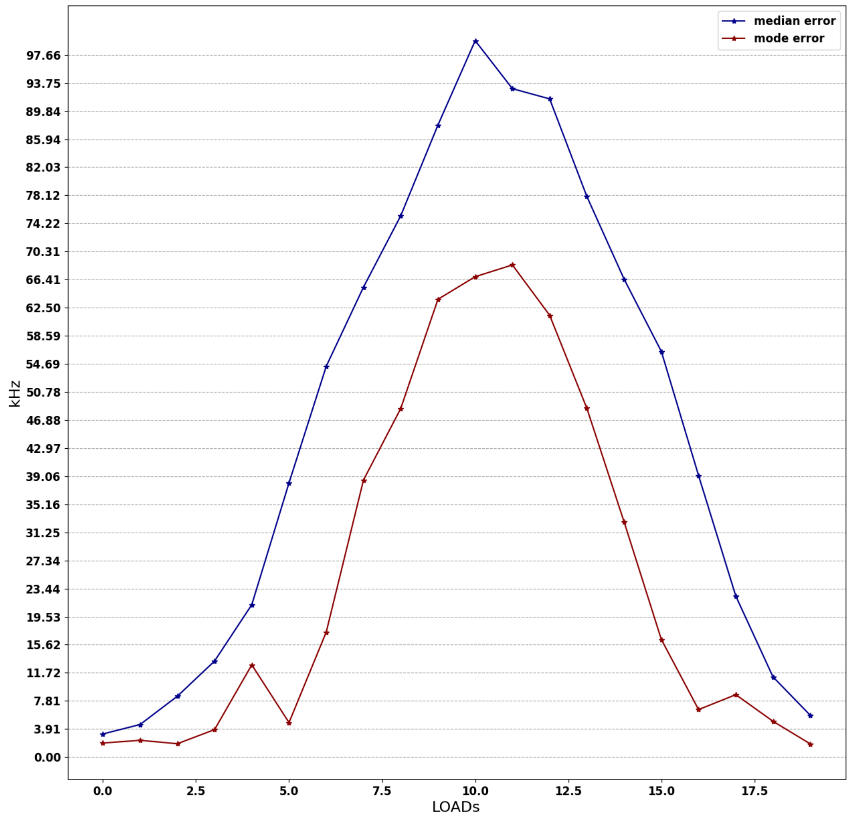

Figure 5.7

A second problem that can be tackled using the polarizer is using it to characterize the MKIDs responses to different temperature loads, studying how the IQ circles evolve. As figure 5.8 shows, we can have a 3-D curve that represents the state of the MKID at different temperatures. Figure 5.9 shows the phase curves at different temperature loads. Part of the future work consists of finding a clever way to utilize this information. For example, one idea consists of having a look-up table with the parameters of every MKID at different temperatures that can be loaded into the readout without having to re-characterize the MKID status. Also, this MKID characterization could help to rescue data when the phase goes out of the linear zone of the circle domain.

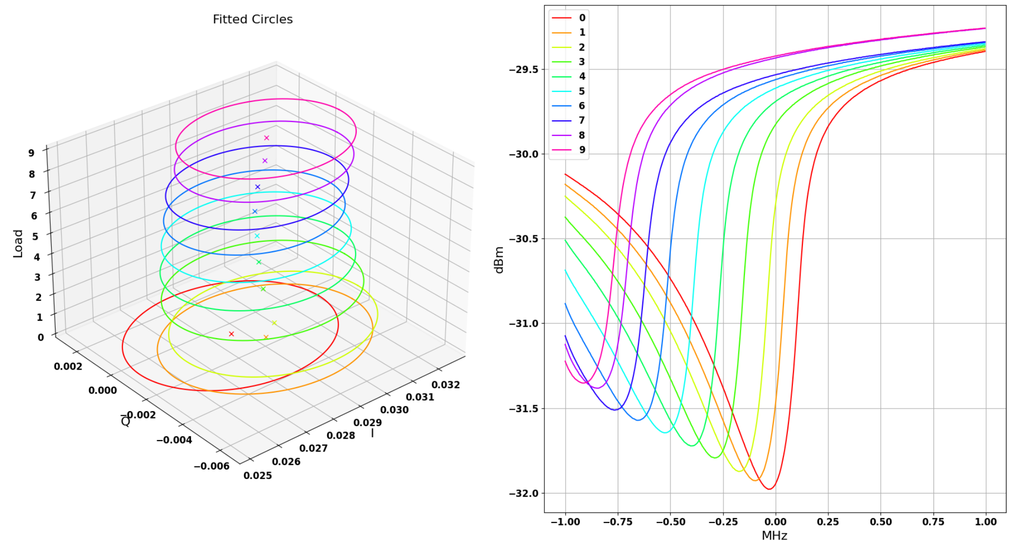

(a) Fitted circles for different temperature loads.

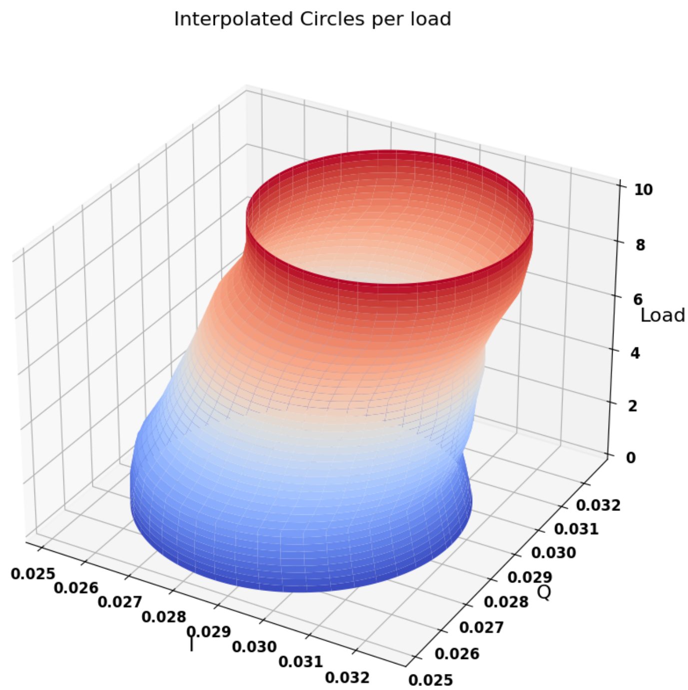

(b) Interpolated circle data.

Figure 5.8: MKID characterization using different temperature loads.

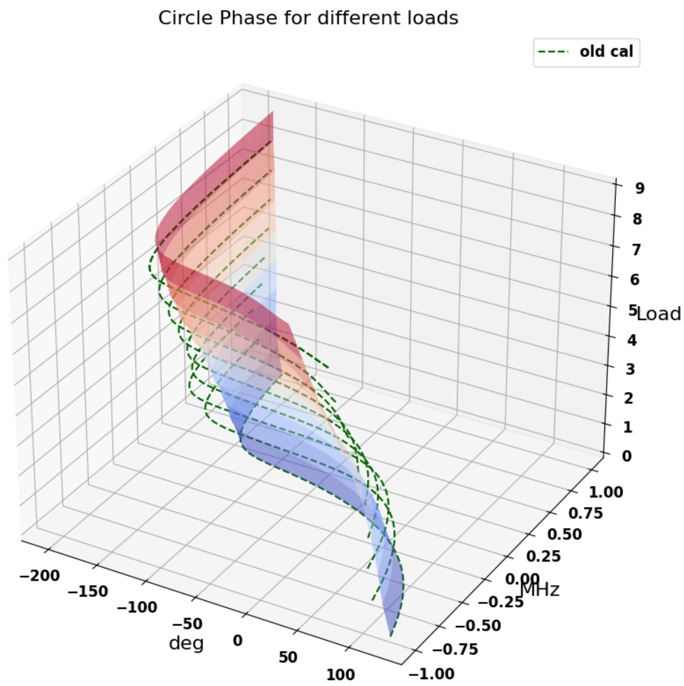

(a) Surface of the phase in the circle domain for different temperature loads.

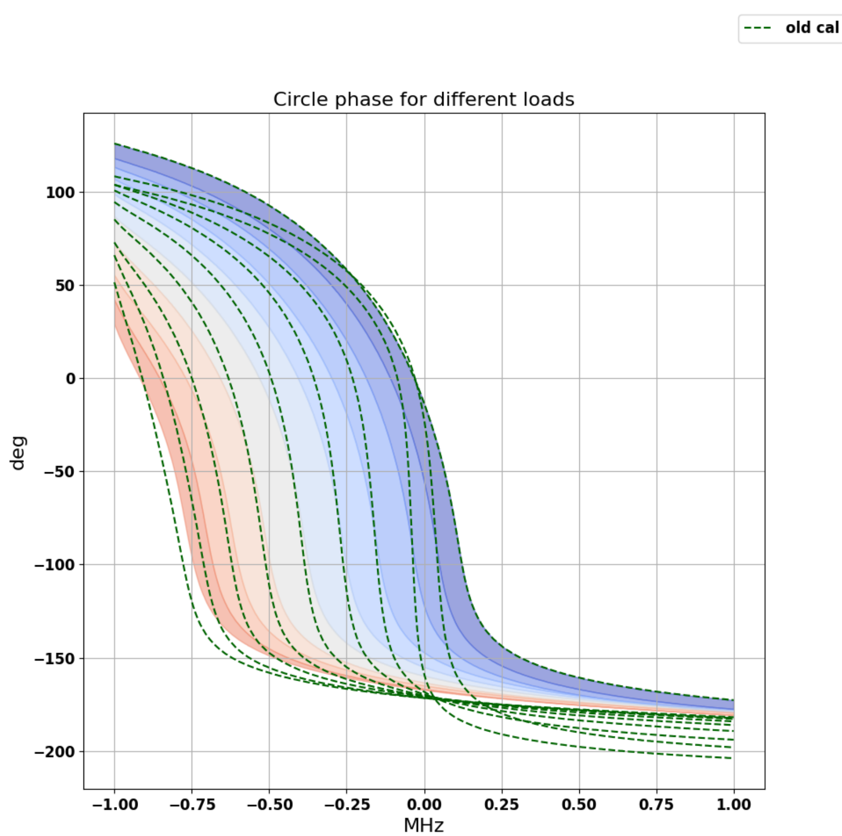

(b) Top view of the phase in the circle domain for different temperature loads.

Figure 5.9: MKID characterization using different temperature loads.

Bibliography

[1] Siringo, G., "PolKa: a polarimeter for submillimeter bolometer arrays," Ph. D. Thesis, 2003.

[2] Stanimirovic, S., Altschuler, D., Goldsmith, P., y Salter, C., "Single-dish radio astronomy: Techniques and applications," 2002.

[3] Timm, C., "Theory of superconducivity," 2023, https://tu-dresden.de/mn/physik/itp/cmt/ressourcen/dateien/skripte/Skript_Supra.pdf?lang=en (visitado el 2023-04-29).

[4] Huebener, R. P., "The path to type-II superconductivity," Metals, vol. 9, no. 6, 2019, doi:10.3390/met9060682.

[5] Tong, D., Statistical Physics. University of Cambridge, 2011, http://www.damtp.cam.ac.uk/user/tong/statphys.html.

[6] New York Times, "Low-temperature superconductivity," 2008, https://archive.nytimes.com/www.nytimes.com/imagepages/2008/01/07/science/20080108_SUPER_GRAPHIC.html (visitado el 2024-04-29).

[7] Annett, J. F., Superconductivity, superfluids and condensates, vol. 5. Oxford University Press, 2004.

[8] Thomas, C. N., Withington, S., Sun, Z., Skyrme, T., y Goldie, D. J., "Nonlinear effects in superconducting thin film microwave resonators," New Journal of Physics, vol. 22, 2020, doi:10.1088/1367-2630/ab97e8.

[9] Doyle, S., Lumped Element Kinetic Inductance Detector. PhD thesis, Cardiff University, 2008.

[10] Zmuidzinas, J., "Superconducting microresonators: Physics and applications," Annual Review of Condensed Matter Physics, vol. 3, pp. 169–214, 2012, doi:10.1146/annurev-conmatphys-020911-125022.

[11] Mazin, B. A., "Microwave kinetic inductance detectors: The first decade," en AIP Conference Proceedings, vol. 1185, pp. 135–142, American Institute of Physics, 2009.

[12] Hickman, I., Analog Electronics: Analog Circuitry Explained. Newnes, 2013.

[13] Probst, S., Song, F., Bushev, P. A., Ustinov, A. V., y Weides, M., "Efficient and robust analysis of complex scattering data under noise in microwave resonators," Review of Scientific Instruments, vol. 86, no. 2, 2015.

[14] Shabani, A., Sarabandi, S., Porta, J. M., y Thomas, F., "A fast branch-and-prune algorithm for the position analysis of spherical mechanisms," vol. 73, pp. 549–558, Springer Science and Business Media B.V., 2019, doi:10.1007/978-3-030-20131-9_55.

[15] Wang, X. y Mortazawi, A., "Bandwidth enhancement of RF resonators using Duffing

nonlinear resonance for wireless power applications," IEEE Transactions on Microwave Theory and Techniques, vol. 64, no. 11, pp. 3695–3702, 2016.

[16] Barry, P., On the development of SuperSpec: a fully integrated on-chip spectrometer for far-infrared astronomy. PhD thesis, Cardiff University, 2014.

[17] Rowe, S., Passive terahertz imaging with lumped element kinetic inductance detectors. PhD thesis, Cardiff University, 2015.

[18] Güsten, R., Nyman, L., Schilke, P., Menten, K., Cesarsky, C., y Booth, R., "The Atacama Pathfinder EXperiment (APEX)–a new submillimeter facility for southern skies–," Astronomy & Astrophysics, vol. 454, no. 2, pp. L13–L16, 2006.

[19] Bernd Klein, "APEX instrumentation." The Atacama Pathfinder Experiment in 2023 and future opportunities conference, 2023.

[20] Belitsky, V., Lapkin, I., Vassilev, V., Monje, R., Pavolotsky, A., Meledin, D., Henke, D., Nystrom, O., Desmaris, V., Risacher, C., *et al.*, "Facility heterodyne receiver for the Atacama Pathfinder EXperiment telescope," en 2007 Joint 32nd International Conference on Infrared and Millimeter Waves and the 15th International Conference on Terahertz Electronics, pp. 326–328, IEEE, 2007.

[21] Baselmans, J., Bueno, J., Yates, S. J., Yurduseven, O., Llombart, N., Karatsu, K., Baryshev, A., Ferrari, L., Endo, A., Thoen, D., *et al.*, "A kilo-pixel imaging system for future space based far-infrared observatories using microwave kinetic inductance detectors," Astronomy & Astrophysics, vol. 601, p. A89, 2017.

[22] Bhatia, R., Chase, S., Edgington, S., Glenn, J., Jones, W., Lange, A., Maffei, B., Mainzer, A., Mauskopf, P., Philhour, B., *et al.*, "A three-stage helium sorption refrigerator for cooling of infrared detectors to 280 mK," Cryogenics, vol. 40, no. 11, pp. 685–691, 2000.

[23] Otal, L. E., The optical system and the astronomical potential of A-MKID, a new camera using microwave kinetic inductance detector technology. PhD thesis, Rheinische Friedrich-Wilhelms-Universität Bonn, 2015.

[24] Reyes, N., Camara, I., Grutzeck, G., Yates, S., Baryshev, A., Klein, B., Weiss, A., Konig, C., Wunsh, H. J., Gorlitz, A., Castenholz, C., Ciechanowicz, M., y Schmitz, A., "A-MKID optical verification," internal report, Max-Planck Institut für Radioastronomie, 2022.

[25] Klein, B., Hochgürtel, S., Krämer, I., Bell, A., Meyer, K., y Güsten, R., "High-resolution wide-band fast fourier transform spectrometers," Astronomy & Astrophysics, vol. 542, p. L3, 2012.

[26] Ronak, B. y Fahmy, S. A., "Mapping for maximum performance on FPGA DSP blocks," IEEE Transactions on Computer-Aided Design of Integrated Circuits and Systems, vol. 35, no. 4, pp. 573–585, 2015.

[27] Kirk, D. B. y Wen-Mei, W. H., Programming massively parallel processors: a hands-on approach. Morgan kaufmann, 2016.

[28] AMD, "69737 - Virtex Ultrascale+ FPGA VCU118 Evaluation kit - board debug checklist," 2020, https://support.xilinx.com/s/article/69737?language=en_US (visitado el 2024-04-29).

[29] NVIDIA, “JETSON AGX XAVIER and the new era of autonomous machines,” 2020, https://info.nvidia.com/rs/156-OFN-742/images/Jetson_AGX_Xavier_New_Era_Autonomous_Machines.pdf (visitado el 2024-04-29).

[30] Lyons, R. G., Understanding digital signal processing, 3/E. Pearson Education India, 1997.

[31] Grutzeck, G., Krämer, I., König, C., Reyes, N., Ciechanowicz, M., Klein, B., Baryshev, A., Yates, S., y Bell, A., “The new readout for A-MKID.” 2022.

[32] Schubert, E., Sander, J., Ester, M., Kriegel, H. P., y Xu, X., “DBSCAN revisited, revisited: why and how you should (still) use DBSCAN,” ACM Transactions on Database Systems (TODS), vol. 42, no. 3, pp. 1–21, 2017.

[33] OpenDataScience, “Open machine learning course,” 2023, https://mlcourse.ai/book/topic03/topic03_decision_trees_kNN.html (visitado el 2023-04-29).

[34] scikit learn, “scikit-learn,” 2023, ttps://scikit-learn.org/stable/modules/tree.html (visitado el 2023-04-29).

[35] van Rantwijk, J., Grim, M., van Loon, D., Yates, S., Baryshev, A., y Baselmans, J., “Multiplexed readout for 1000-pixel arrays of microwave kinetic inductance detectors,” IEEE Transactions on Microwave Theory and Techniques, vol. 64, no. 6, pp. 1876–1883, 2016.

[36] Condon, J. J. y Ransom, S. M., Essential Radio Astronomy, vol. 2. Princeton University Press, 2016.

[37] Bounmy, J., Hoarau, C., Macías-Pérez, J.-F., Beelen, A., Benoît, A., Bourrion, O., Calvo, M., Catalano, A., Fasano, A., Goupy, J., *et al.*, “CONCERTO: Digital processing for finding and tuning LEKIDs,” Journal of Instrumentation, vol. 17, no. 08, p. P08037, 2022.